PHYSICAL REVIEW D **92,** 032002 (2015)

Dalitz plot analysis of $B^0 \to \bar{D}^0\pi^+\pi^-$ decays

R. Aaij *et al.*[*]
(LHCb Collaboration)

(Received 8 May 2015; published 7 August 2015)

The resonant substructures of $B^0 \to \bar{D}^0\pi^+\pi^-$ decays are studied with the Dalitz plot technique. In this study a data sample corresponding to an integrated luminosity of 3.0 fb^{-1} of pp collisions collected by the LHCb detector is used. The branching fraction of the $B^0 \to \bar{D}^0\pi^+\pi^-$ decay in the region $m(\bar{D}^0\pi^\pm) > 2.1$ GeV/c^2 is measured to be $(8.46 \pm 0.14 \pm 0.29 \pm 0.40) \times 10^{-4}$, where the first uncertainty is statistical, the second is systematic and the last arises from the normalization channel $B^0 \to D^*(2010)^-\pi^+$. The $\pi^+\pi^-$ S-wave components are modeled with the isobar and K-matrix formalisms. Results of the Dalitz plot analyses using both models are presented. A resonant structure at $m(\bar{D}^0\pi^-) \approx 2.8$ GeV/c^2 is confirmed and its spin-parity is determined for the first time as $J^P = 3^-$. The branching fraction, mass and width of this structure are determined together with those of the $D_0^*(2400)^-$ and $D_2^*(2460)^-$ resonances. The branching fractions of other $B^0 \to \bar{D}^0 h^0$ decay components with $h^0 \to \pi^+\pi^-$ are also reported. Many of these branching fraction measurements are the most precise to date. The first observation of the decays $B^0 \to \bar{D}^0 f_0(500)$, $B^0 \to \bar{D}^0 f_0(980)$, $B^0 \to \bar{D}^0\rho(1450)$, $B^0 \to D_3^*(2760)^-\pi^+$ and the first evidence of $B^0 \to \bar{D}^0 f_0(2020)$ are presented.

DOI: 10.1103/PhysRevD.92.032002 PACS numbers: 14.40.Lb, 14.40.Be, 14.40.Nd

I. INTRODUCTION

The study of the Cabibbo-Kobayashi-Maskawa (CKM) mechanism [1,2] is a central topic in flavor physics. Accurate measurements of the various CKM matrix parameters through different processes provide sensitivity to new physics effects, by testing the global consistency of the Standard Model. Among them, the CKM angle β is expressed in terms of the CKM matrix elements as $\arg(-V_{cd}V_{cb}^*/V_{td}V_{tb}^*)$. The most precise measurements have been obtained with the $B^0 \to (c\bar{c})K^{(*)0}$ decays by *BABAR* [3], Belle [4] and more recently by LHCb [5]. The decay[1] $B^0 \to \bar{D}^0\pi^+\pi^-$ through the $b \to c\bar{u}d$ transition has sensitivity to the CKM angle β [6–10] and to new physics effects [11–14].

The Dalitz plot analysis [15] of $B^0 \to \bar{D}^0\pi^+\pi^-$ decays, with the $\bar{D}^0 \to K^+\pi^-$ mode, is presented as the first step towards an alternative method to measure the CKM angle β. Two sets of results are given, where the $\pi^+\pi^-$ S-wave components are modeled with the isobar [16–18] and K-matrix [19] formalisms. Dalitz plot analyses of the decay $B^0 \to \bar{D}^0\pi^+\pi^-$ have already been performed by Belle [20,21] and *BABAR* [22]. Similar studies for the charged B decays $B^- \to D^{(*)+}\pi^-\pi^-$ have been published by the B-factories [23,24]. The LHCb data set offers a larger and almost pure signal sample. Feynman diagrams of the dominant tree level amplitudes contributing to the decay $B^0 \to \bar{D}^0\pi^+\pi^-$ are shown in Fig. 1.

In addition to the interest for the CKM parameter measurements, the analysis of the Dalitz plot of the $B^0 \to \bar{D}^0\pi^+\pi^-$ decay is motivated by its rich resonant structure. The decay $B^0 \to \bar{D}^0\pi^+\pi^-$ contains information about excited D mesons decaying to $D\pi$, with natural spin and parity $J^P = 0^+, 1^-, 2^+, \ldots$ A complementary Dalitz plot analysis of the decay $B_s^0 \to \bar{D}^0 K^-\pi^+$ was recently published by LHCb [25,26], and constrains the phenomenology of the $\bar{D}^0 K^-$ (D_{sJ}^-) and $K^-\pi^+$ states. The spectrum of excited D mesons is predicted by theory [27,28] and contains the known states $D^*(2010), D_0^*(2400)$, $D_2^*(2460)$, as well as other unknown states not yet fully explored. An extensive discussion on theory predictions for the $c\bar{u}$, $c\bar{d}$ and $c\bar{s}$ mass spectra is provided in Refs. [26,29]. More recent measurements performed in inclusive decays by *BABAR* [30] and LHCb [29] have led to the observation of several new states: $D^*(2650), D^*(2760)$, and $D^*(3000)$. However, their spin and parity are difficult to determine from inclusive studies. Orbitally excited D mesons have also been studied in semileptonic B decays (see a review in Ref. [31]) with limited precision. These are of prime interest both in the extraction of the CKM parameter $|V_{cb}|$, where longstanding differences remain between exclusive and inclusive methods (see review in Ref. [32]), and in recent studies of $B \to D^{(*)}\tau\bar{\nu}_\tau$ [33] which have generated much theoretical discussion (see, e.g., Refs. [34,35]).

[*]Full author list given at end of the article.

[1]The inclusion of charge conjugate states is implied throughout the paper.

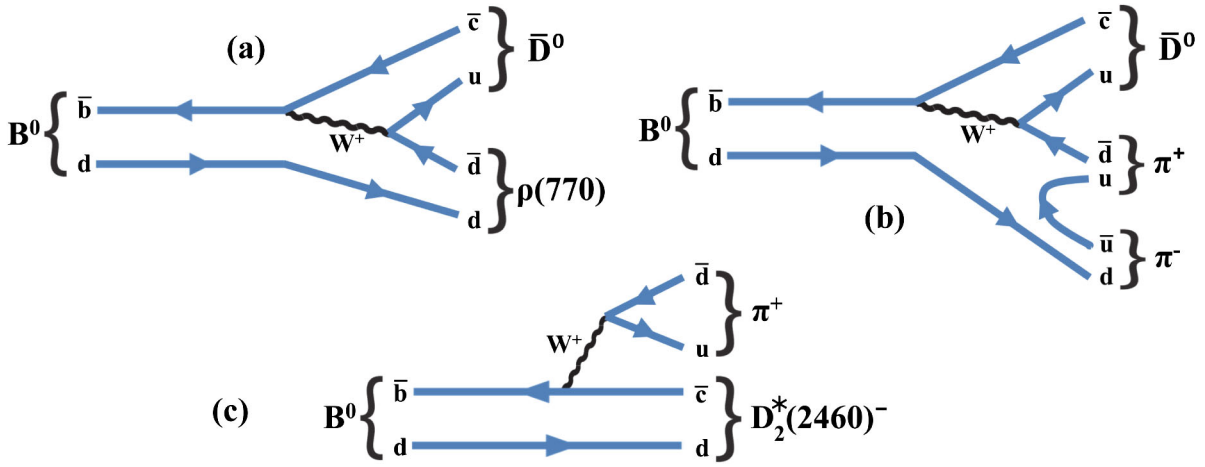

FIG. 1 (color online). Examples of tree diagrams via $\bar{b} \to \bar{c}u\bar{d}$ transition to produce (a) $\pi^+\pi^-$ resonances, (b) nonresonant three-body decay and (c) $\bar{D}^0\pi^-$ resonances.

A measurement of the branching fraction of the decay $B^0 \to \bar{D}^0\rho^0$ is also presented. This study helps in understanding the effects of color suppression in B decays, which is due to the requirement that the color quantum numbers of the quarks produced from the virtual W boson must match those of the spectator quark to form a ρ^0 meson [36–40]. Moreover, using isospin symmetry to relate the decay amplitudes of $B^0 \to \bar{D}^0\rho^0$, $B^0 \to D^-\rho^+$ and $B^+ \to \bar{D}^0\rho^+$, effects of final-state interactions (FSI) can be studied in those decays (see a review in Refs. [37,41]). The previous measurement for the branching fraction of $B^0 \to \bar{D}^0\rho^0$ has limited precision, $(3.2 \pm 0.5) \times 10^{-4}$ [21], and is in agreement with theoretical predictions that range from 1.7 to 3.4×10^{-4} [38,42].

Finally, a study of the $\pi^+\pi^-$ system is performed on a broad phase-space range in $B^0 \to \bar{D}^0\pi^+\pi^-$ from 280 MeV/c^2 ($\approx 2m_\pi$) to 3.4 GeV/c^2 ($\approx m_{B^0_d} - m_{D^0}$), which is much larger than that accessible in charmed meson decays such as $D^0 \to K^0_S\pi^+\pi^-$ [43–45] or in B decays such as $B^0_{(s)} \to J/\psi\pi^+\pi^-$ [46–49]. The nature of the light scalar $\pi^+\pi^-$ states below 1 GeV/c^2 ($J^{PC} = 0^{++}$), and in particular the $f_0(500)$ and $f_0(980)$ states, has been a longstanding debate (see, e.g., Refs. [50–52]). Popular interpretations include tetraquarks, meson-meson bound states (molecules), or some other mixtures, where the isosinglets $f_0(500)$ and $f_0(980)$ can mix, therefore leading to a nontrivial nature (e.g. pure $s\bar{s}$ state) of the $f_0(980)$ and complicating the determination of the CKM phase ϕ_s from $B^0_s \to J/\psi\pi^+\pi^-$ decays [48,53,54]. In the tetraquark picture, the mixing angle, $\omega_{\rm mix}$, between the $f_0(980)$ and $f_0(500)$ states is predicted to be $|\omega_{\rm mix}| \approx 20°$ [55,56] (recomputed with the latest average of the mass of the κ meson 682 ± 29 MeV/c^2 [32]). Other theory models based on QCD factorization and its extensions [57,58] predict that the $f_0(500)$ and $f_0(980)$ mixing angle $\varphi_{\rm mix}$ for the $q\bar{q}$ model is $20° \lesssim \varphi_{\rm mix} \lesssim 45°$. The LHCb experiment, in the study of $B^0_{(s)} \to J/\psi\pi^+\pi^-$ decays [47–49], has already set stringent upper bounds on $\varphi_{\rm mix}$ in B^0 (B^0_s) decay: $\varphi_{\rm mix} < 17°$ ($< 7.7°$) at 90% C.L. For the first time, the $f_0(500) - f_0(980)$ mixing in the $B^0 \to \bar{D}^0\pi^+\pi^-$ decay, both in $q\bar{q}$ and tetraquark pictures, is studied.

The analysis of the decay $B^0 \to \bar{D}^0\pi^+\pi^-$ presented in this paper is based on a data sample corresponding to an integrated luminosity of 3.0 fb^{-1} of pp collision data collected with the LHCb detector. Approximately one third of the data was obtained during 2011 when the collision center-of-mass energy was $\sqrt{s} = 7$ TeV and the rest during 2012 with $\sqrt{s} = 8$ TeV.

The paper is organized as follows. A brief description of the LHCb detector as well as the reconstruction and simulation software is given in Sec. II. The selection of signal candidates and the fit to the B^0 candidate invariant mass distribution used to separate and to measure signal and background yields are described in Sec. III. An overview of the Dalitz plot analysis formalism is given in Sec. IV. Details and results of the amplitude analysis fits are presented in Sec. V. In Sec. VI the measurement of the $B^0 \to \bar{D}^0\pi^+\pi^-$ branching fraction is documented. The evaluation of systematic uncertainties is described in Sec. VII. The results are given in Sec. VIII, and a summary concludes the paper in Sec. IX.

II. THE LHCB DETECTOR

The LHCb detector [59] is a single-arm forward spectrometer covering the pseudorapidity range $2 < \eta < 5$, designed for the study of particles containing b or c quarks. The detector includes a high-precision tracking system consisting of a silicon-strip vertex detector surrounding the pp interaction region [60], a large-area silicon-strip

detector located upstream of a dipole magnet with a bending power of about 4 Tm, and three stations of silicon-strip detectors and straw drift tubes [61] placed downstream of the magnet. The tracking system provides a measurement of momentum, p, with a relative uncertainty that varies from 0.4% at low momentum to 0.6% at 100 GeV/c. The minimum distance of a track to a primary vertex, the impact parameter (IP), is measured with a resolution of $(15 + 29/p_{\mathrm{T}})$ μm, where p_{T} is the component of p transverse to the beam, in GeV/c. Different types of charged hadrons are distinguished using information from two ring-imaging Cherenkov detectors [62]. Photon, electron and hadron candidates are identified by a calorimeter system consisting of scintillating-pad and preshower detectors, an electromagnetic calorimeter and a hadronic calorimeter. Muons are identified by a system composed of alternating layers of iron and multiwire proportional chambers [63].

The online event selection is performed by a trigger which consists of a hardware stage, based on information from the calorimeter and muon systems, followed by a software stage, which applies a full event reconstruction. At the hardware trigger stage, events are required to have a muon with high p_{T} or a hadron, photon or electron with high transverse energy in the calorimeters. For hadrons, the transverse energy threshold is 3.5 GeV. The software trigger requires a two-, three- or four-track secondary vertex with a significant displacement from the primary pp interaction vertices (PVs). At least one charged particle must have a transverse momentum $p_{\mathrm{T}} > 1.7$ GeV/c and be inconsistent with originating from a PV. A multivariate algorithm [64] is used for the identification of secondary vertices consistent with the decay of a b hadron. The p_{T} of the photon from D_s^{*-} decay is too low to contribute to the trigger decision.

Simulated events are used to characterize the detector response to signal and certain types of background events. In the simulation, pp collisions are generated using PYTHIA [65] with a specific LHCb configuration [66]. Decays of hadronic particles are described by EVTGEN [67], in which final-state radiation is generated using PHOTOS [68]. The interaction of the generated particles with the detector and its response are implemented using the GEANT4 toolkit [69] as described in Ref. [70].

III. EVENT SELECTION

Signal B^0 candidates are formed by combining $\bar{D}^0$ candidates, reconstructed in the decay channel $K^+\pi^-$, with two additional pion candidates of opposite charge. Reconstructed tracks are required to be of good quality and to be inconsistent with originating from a PV. They are also required to have sufficiently high p and p_{T} and to be within kinematic regions where reasonable particle identification (PID) performance is achieved, as determined by calibration samples of $D^{*+} \to D^0(K^-\pi^+)\pi^+$ decays. The four final-state tracks are required to be positively identified by the PID system. The $\bar{D}^0$ daughters are required to form a good quality vertex and to have an invariant mass within 100 MeV/c^2 of the known $\bar{D}^0$ mass [32]. The $\bar{D}^0$ candidates and the two charged pion candidates are required to form a good vertex. The reconstructed $\bar{D}^0$ and B^0 vertices are required to be significantly displaced from the PV. To improve the B^0 candidate invariant mass resolution, a kinematic fit [71] is used, constraining the $\bar{D}^0$ candidate to its known mass [32].

By requiring the reconstructed $\bar{D}^0$ vertex to be displaced downstream from the reconstructed B^0 vertex, backgrounds from both charmless B decays and direct prompt charm production coming from the PV are reduced to a negligible level. Background from $D^*(2010)^-$ decays is removed by requiring $m(\bar{D}^0\pi^\pm) > 2.1$ GeV/c. Backgrounds from doubly misidentified $\bar{D}^0 \to K^+\pi^-$ or doubly Cabibbo-suppressed $\bar{D}^0 \to K^-\pi^+$ decays are also removed by this requirement.

To further distinguish signal from combinatorial background, a multivariate analysis based on a Fisher discriminant [72] is applied. The *sPlot* technique [73] is used to statistically separate signal and background events with the B^0 candidate mass used as the discriminating variable. Weights obtained from this procedure are applied to the candidates to obtain signal and background distributions that are used to train the discriminant. The Fisher discriminant uses information about the event kinematic properties, vertex quality, IP and p_{T} of the tracks and flight distance from the PV. It is optimized by maximizing the purity of the signal events.

Signal candidates are retained for the Dalitz plot analysis if the invariant mass of the B^0 meson lies in the range [5250, 5310] MeV/c^2 and that of the $\bar{D}^0$ meson in the range [1840, 1890] MeV/c^2 (called the signal region). Once all selection requirements are applied, less than 1% of the events contain multiple candidates, and in those cases one candidate is chosen randomly.

Background contributions from decays with the same topology, but having one or two misidentified particles, are estimated to be less than 1% and are not considered in the Dalitz analysis. These background contributions include decays like $B^0 \to \bar{D}^0 K^+\pi^-$, $B_s^0 \to \bar{D}^0 K^-\pi^+$ [74], $\Lambda_b^0 \to D^0 p\pi^-$ [75] and $B^0 \to \bar{D}^0\pi^+\pi^-$ with $\bar{D}^0 \to \pi^+\pi^-$ or $\bar{D}^0 \to K^+K^-$.

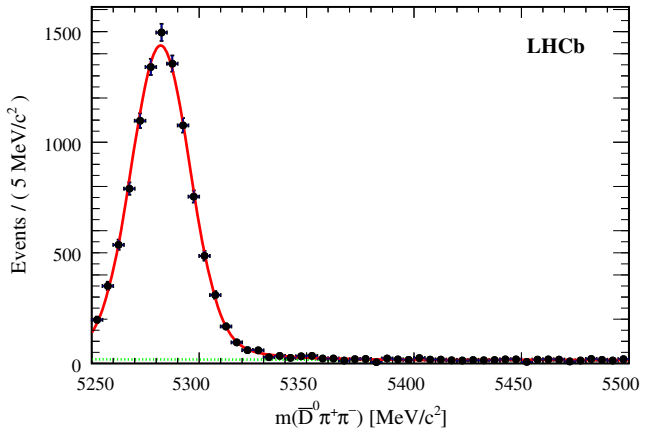

FIG. 2 (color online). Invariant mass distribution of $B^0 \to \bar{D}^0\pi^+\pi^-$ candidates. Data points are shown in black. The fit is shown as a solid (red) line with the background component displayed as dashed (green) line.

Partially reconstructed decays of the type $B^0 \to \bar{D}^0\pi^+\pi^-X$, where one or more particles are not reconstructed, have similar efficiencies to the signal channel decays. They are distributed in the region below the B^0 mass. By requiring the invariant mass of B^0 candidates to be larger than 5250 MeV/c^2, these backgrounds are reduced to a negligible level, as determined by simulated samples of $B^0 \to \bar{D}^{*0}\pi^+\pi^-$ and $B^0 \to \bar{D}^{*0}\rho(770)$ with $\bar{D}^{*0}$ decaying into $\bar{D}^0\gamma$ or $\bar{D}^0\pi^0$ under different hypotheses for the $\bar{D}^{*0}$ helicity.

The signal and combinatorial background yields are determined using an unbinned extended maximum likelihood fit to the invariant mass distribution of B^0 candidates. The invariant mass distribution is shown in Fig. 2, with the fit result superimposed. The fit uses a Crystal Ball (CB) function [76] convoluted with a Gaussian function for the signal distribution and a linear function for the combinatorial background distribution in the mass range of [5250, 5500] MeV/c. Simulated studies validate this choice of signal shape and the tail parameters of the CB function are fixed to those determined from simulation. Table I summarizes the fit results on the free parameters,

TABLE I. Results of the fit to the invariant mass distribution of $B^0 \to \bar{D}^0\pi^+\pi^-$ candidates. Uncertainties are statistical only.

Parameter	Value
μ_{B^0}	5282.1 ± 0.2 MeV/c^2
$\sigma_{\rm G}$	33.6 ± 5.4 MeV/c^2
$\sigma_{\rm CB}$	13.4 ± 0.3 MeV/c^2
$f_{\rm CB}$	0.908 ± 0.025
p_1	-0.152 ± 0.035 (GeV/c)$^{-1}$
ν_s^0	9565 ± 116
ν_b^0	215 ± 19

where μ_{B^0} is the mean peak position and $\sigma_{\rm G}$ is the width of the Gaussian function. The parameter $\sigma_{\rm CB}$ is the width of the Gaussian core of the CB function. The parameters $f_{\rm CB}$ and p_1 give the fit fraction of the CB function and the slope of the linear function that describes the background distribution. The yields of signal (ν_s^0) and background (ν_b^0) events given in Table I are calculated within the signal region. The purity is $(97.8 \pm 0.2)\%$.

IV. DALITZ PLOT ANALYSIS FORMALISM

The analysis of the distribution of decays across the Dalitz plot [15] allows a determination of the amplitudes contributing to the three-body $B^0 \to \bar{D}^0\pi^+\pi^-$ decay. Two of the three possible two-body invariant mass-squared combinations, which are connected by

$$m^2(\bar{D}^0\pi^+) + m^2(\bar{D}^0\pi^-) + m^2(\pi^+\pi^-) = m_{B^0}^2 + m_{D^0}^2 + 2m_\pi^2, \tag{1}$$

are sufficient to describe the kinematics of the system. The two observables $m^2(\bar{D}^0\pi^-)$ and $m^2(\pi^+\pi^-)$, where resonances are expected to appear, are chosen in this paper. These observables are calculated with the masses of the B^0 and $\bar{D}^0$ mesons constrained to their known values [32]. The invariant mass resolution has negligible effect and therefore it is not modeled in the Dalitz plot analysis.

The total decay amplitude is described by a coherent sum of amplitudes from resonant or nonresonant intermediate processes as

$$M(\vec{x}) = \sum_i c_i A_i(\vec{x}). \tag{2}$$

The complex coefficient c_i and amplitude $A_i(\vec{x})$ describe the relative contribution and dynamics of the ith intermediate state, where $\vec{x}$ represents the $(m^2(\bar{D}^0\pi^-), m^2(\pi^+\pi^-))$ coordinates in the Dalitz plot. The Dalitz plot analysis determines the coefficients c_i. In addition, fit fractions and interference fit fractions are also calculated to give a convention-independent representation of the population of the Dalitz plot. The fit fractions are defined as

$$\mathcal{F}_i = \frac{\int |c_i A_i(\vec{x})|^2 d\vec{x}}{\int |\sum_i c_i A_i(\vec{x})|^2 d\vec{x}}, \tag{3}$$

and the interference fit fractions between the resonances i and j $(i < j)$ are defined as

$$\mathcal{F}_{ij} = \frac{\int 2\mathrm{Re}[c_i c_j^* A_i(\vec{x}) A_j^*(\vec{x})] d\vec{x}}{\int |\sum_i c_i A_i(\vec{x})|^2 d\vec{x}}, \tag{4}$$

where the integration is performed over the full Dalitz plot with $m(\bar{D}^0\pi^\pm) > 2.1$ GeV/c. Due to these interferences

between different contributions, the sum of the fit fractions is not necessarily equal to unity.

The amplitude $A_i(\vec{x})$ for a specific resonance r with spin L is written as

$$A_i(\vec{x}) = F_B^{(L)}(q, q_0) \times F_r^{(L)}(p, p_0) \times T_L(\vec{x}) \times R(\vec{x}). \quad (5)$$

The functions $F_B^{(L)}(q, q_0)$ and $F_r^{(L)}(p, p_0)$ are the Blatt-Weisskopf barrier factors [77] for the production, $B^0 \to r h_3$, and the decay, $r \to h_1 h_2$, of the resonance, respectively. The parameters p and q are the momenta of one of the resonance daughters (h_1 or h_2) and of the bachelor particle (h_3), respectively, both evaluated in the rest frame of the resonance. The value p_0 (q_0) represents the value of p (q) when the invariant mass of the resonance is equal to its pole mass. The spin-dependent F_B and F_r functions are defined as

$$\begin{aligned}
&L=0\text{: } F^{(0)}(z,z_0)=1,\\
&L=1\text{: } F^{(1)}(z,z_0)=\sqrt{\frac{1+z_0}{1+z}},\\
&L=2\text{: } F^{(2)}(z,z_0)=\sqrt{\frac{(z_0-3)^2+9z_0}{(z-3)^2+9z}},\\
&L=3\text{: } F^{(3)}(z,z_0)=\sqrt{\frac{z_0(z_0-15)^2+9(2z_0-5)}{z(z-15)^2+9(2z-5)}},\\
&L=4\text{: } F^{(4)}(z,z_0)=\sqrt{\frac{(z_0^2-45z_0+105)^2+25z_0(2z_0-21)^2}{(z^2-45z+105)^2+25z(2z-21)^2}},
\end{aligned} \quad (6)$$

where $z_{(0)}$ is equal to $(r_{\rm BW} \times q_{(0)})^2$ or $(r_{\rm BW} \times p_{(0)})^2$. The value for the radius of the resonance, $r_{\rm BW}$, is taken to be 1.6 GeV$^{-1} \times \hbar c$ ($= 0.3$ fm) [78].

The function $T_L(\vec{x})$ represents the angular distribution for the decay of a spin L resonance. It is defined as

$$\begin{aligned}
&L=0\text{: } T_0=1,\\
&L=1\text{: } T_1=\sqrt{1+y^2}\cos\theta \times qp,\\
&L=2\text{: } T_2=(y^2+3/2)(\cos^2\theta-1/3)\times q^2p^2,\\
&L=3\text{: } T_3=\sqrt{1+y^2}(1+2y^2/5)(\cos^3\theta-3\cos(\theta)/5)\\
&\qquad\times q^3p^3,\\
&L=4\text{: } T_4=(8y^4/35+40y^2/35+1)\\
&\qquad\times(\cos^4\theta-30\cos^2(\theta)/35+3/35)\times q^4p^4.
\end{aligned} \quad (7)$$

The helicity angle, θ, of the resonance is defined as the angle between the direction of the momenta p and q. The y dependence accounts for relativistic transformations between the B^0 and the resonance rest frames [79,80], where

$$1+y^2 = \frac{m_{B^0}^2 + m^2(h_1h_2) - m_{h_3}^2}{2m(h_1h_2)m_{B^0}}. \quad (8)$$

Finally, $R(\vec{x})$ is the resonant line shape and is described by the relativistic Breit-Wigner (RBW) function unless specified otherwise,

$$\mathrm{RBW}(s) = \frac{1}{m_r^2 - s - i m_r \Gamma^{(L)}(s)}, \quad (9)$$

where $s = m^2(h_1h_2)$ and m_r is the pole mass of the resonance; $\Gamma^{(L)}(s)$, the mass-dependent width, is defined as

$$\Gamma^{(L)}(s) = \Gamma_0 \left(\frac{p}{p_0}\right)^{2L+1} \left(\frac{m_r}{\sqrt{s}}\right) F_r^{(L)}(p, p_0)^2, \quad (10)$$

where Γ_0 is the partial width of the resonance, i.e., the width at the peak mass $s = m_r$.

The line shapes of $\rho(770)$, $\rho(1450)$ and $\rho(1700)$ are described by the Gounaris-Sakurai (GS) function [81],

$$\mathrm{GS}(s) = \frac{m_r^2(1+\Gamma_0 g/m_r)}{m_r^2 - s + f(s) - i m_r \Gamma_\rho(s)}, \quad (11)$$

where

$$\begin{aligned}
f(s) &= \Gamma_0 \frac{m_r^2}{p_0^3}\left[(h(s)-h(m_r^2))p^2\right.\\
&\qquad\left.+(m_r^2-s)p_0^2\left.\frac{dh}{ds}\right|_{s=m_r^2}\right],\\
h(s) &= \frac{2}{\pi}\frac{p}{\sqrt{s}}\log\left(\frac{\sqrt{s}+2p}{2m_\pi}\right),\\
g &= \frac{3}{\pi}\frac{m_\pi^2}{p_0^2}\log\left(\frac{m_r+2p_0}{2m_\pi}\right)+\frac{m_r}{2\pi p_0}-\frac{m_\pi^2 m_r}{\pi p_0^3},\\
\text{and}\quad \Gamma_\rho(s) &= \Gamma_0\left[\frac{p}{p_0}\right]^3\left[\frac{m_r^2}{s}\right]^{1/2}.
\end{aligned} \quad (12)$$

The $\rho - \omega$ interference is taken into account by

$$R_{\rho-\omega}(s) = \mathrm{GS}_{\rho(770)}(s) \times (1 + a e^{i\theta} \mathrm{RBW}_{\omega(782)}(s)), \quad (13)$$

where Γ_0 is used, instead of the mass-dependent width $\Gamma^{(L)}(s)$, for $\omega(782)$ [82].

The $D^*(2010)^-$ contribution is vetoed as described in Sec. III. Possible remaining contributions from the $D^*(2010)^-$ RBW tail or general $\bar{D}^0\pi^-$ P-waves are modeled as

$$R_{D^*(2010)}(m^2(\bar{D}^0\pi^+)) = e^{-(\beta_1+i\beta_2)m^2(\bar{D}^0\pi^+)}, \quad (14)$$

where β_1 and β_2 are free parameters.

The $\pi^+\pi^-$ S-wave contribution is modeled using two alternative approaches, the isobar model [16–18] or the K-matrix model [19]. Contributions from the $f_0(500)$, $f_0(980)$, $f_0(2020)$ resonances and a nonresonant component are parametrized separately in the isobar model and globally by one amplitude in the K-matrix model.

In the isobar model, the $f_0(2020)$ resonance is modeled by a RBW function and the modeling of the $f_0(500)$, $f_0(980)$ resonances and the nonresonant contribution are described as follows. The Bugg resonant line shape [83] is employed for the $f_0(500)$ contribution,

$$R_{f_0(500)}(s) = m_r\Gamma_1(s)/\left[m_r^2 - s - g_1^2\frac{s-s_A}{m_r^2-s_A}z(s) - im_r\Gamma_{\rm tot}(s)\right], \quad (15)$$

where

$$\begin{aligned}
m_r\Gamma_1(s) &= g_1^2\frac{s-s_A}{m_r^2-s_A}\rho_1(s),\\
g_1^2(s) &= m_r(b_1+b_2 s)\exp(-(s-m_r^2)/A),\\
z(s) &= j_1(s) - j_1(m_r^2),\\
j_1(s) &= \frac{1}{\pi}\left[2+\rho_1\log\left(\frac{1-\rho_1}{1+\rho_1}\right)\right],\\
m_r\Gamma_2(s) &= 0.6g_1^2(s)(s/m_r^2)\exp(-\alpha|s-4m_K^2|)\rho_2(s),\\
m_r\Gamma_3(s) &= 0.2g_1^2(s)(s/m_r^2)\exp(-\alpha|s-4m_\eta^2|)\rho_3(s),\\
m_r\Gamma_4(s) &= m_r g_{4\pi}\rho_{4\pi}(s)/\rho_{4\pi}(m_r^2),\\
\rho_{4\pi}(s) &= 1/[1+\exp(7.082-2.845s)],\\
\text{and}\quad \Gamma_{\rm tot}(s) &= \sum_{i=1}^{4}\Gamma_i(s).
\end{aligned} \quad (16)$$

The parameters are fixed to $m_r = 0.953\ \text{GeV}/c^2$, $s_A = 0.41m_\pi^2$, $b_1 = 1.302\ \text{GeV}^2/c^4$, $b_2 = 0.340$, $A = 2.426\ \text{GeV}^2/c^4$ and $g_{4\pi} = 0.011\ \text{GeV}/c^2$ [83]. The phase-space factors of the decay channels $\pi\pi$, KK and $\eta\eta$ correspond to $\rho_{1,2,3}(s)$, respectively, and are defined as

$$\rho_{1,2,3}(s) = \sqrt{1-4\frac{m_{1,2,3}^2}{s}}, \qquad 1,2, \quad \text{and} \quad 3=\pi, \quad K \quad \text{and} \quad \eta. \quad (17)$$

The Flatté formula [84] is used to describe the $f_0(980)$ line shape,

$$R_{f_0(980)}(s) = \frac{1}{m_r^2 - s - im_r(\rho_{\pi\pi}(s)g_1 + \rho_{KK}(s)g_2)}, \quad (18)$$

where

$$\rho_{\pi\pi}(s) = \frac{2}{3}\sqrt{1-\frac{4m_{\pi^\pm}^2}{s}} + \frac{1}{3}\sqrt{1-\frac{4m_{\pi^0}^2}{s}},$$
$$\text{and}\quad \rho_{KK}(s) = \frac{1}{2}\sqrt{1-\frac{4m_{K^\pm}^2}{s}} + \frac{1}{2}\sqrt{1-\frac{4m_{K^0}^2}{s}}. \quad (19)$$

The parameters $g_{1(2)}$ and m_r [46] are $m_r = 939.9 \pm 6.3\ \text{MeV}/c^2$, $g_1 = 199 \pm 30\ \text{MeV}$ and $g_2/g_1 = 3.0 \pm 0.3$.

The nonresonant contribution is described by

$$R_{NR}(m^2(\pi^+\pi^-), m^2(\bar{D}^0\pi^+)) = e^{i\alpha m^2(\pi^+\pi^-)}. \quad (20)$$

Its modulus equals unity, and a slowly varying phase over $m^2(\pi^+\pi^-)$ accounts for rescattering effects of the $\pi^+\pi^-$ final state and α is a free parameter of the model.

The K-matrix formalism [19] describes the production, rescattering and decay of the $\pi^+\pi^-$ S-wave in a coherent way. The scattering matrix S, from an initial state to a final state, is

$$S = I + 2i(\rho^\dagger)^{1/2}T\rho^{1/2}, \quad (21)$$

where I is the identity matrix, ρ is a diagonal phase-space matrix and T is the transition matrix. The unitarity requirement $SS^\dagger = I$ gives

$$(T^{-1} + i\rho)^\dagger = T^{-1} + i\rho. \quad (22)$$

The K-matrix is a Lorentz-invariant Hermitian matrix, defined as $\mathrm{K}^{-1} = T^{-1} + i\rho$. The amplitude for a decay process,

$$A_i = (I - i\mathrm{K}\rho)^{-1}_{ij}P_j, \quad (23)$$

is computed by combining the K-matrix obtained from a scattering experiment with a production vector to describe process-dependent contributions. The K-matrix is modeled as a five-pole structure,

$$\mathrm{K}_{ij}(s) = \left(\sum_\alpha \frac{g_i^\alpha g_j^\alpha}{m_\alpha^2 - s} + f_{ij}^{\rm scatt}\frac{1-s_0^{\rm scatt}}{s-s_0^{\rm scatt}}\right) \times \frac{1-s_{A0}}{s-s_{A0}}\left(s - \frac{s_A m_\pi^2}{2}\right), \quad (24)$$

where the indexes $i,j = 1,2,3,4,5$ correspond to five decay channels: $\pi\pi$, $K\bar{K}$, $\eta\eta$, $\eta\eta'$ and multimeson (mainly 4π states) respectively. The coupling constant of the bare state α to the decay channel i, g_i^α, is obtained from a global

TABLE II. The K-matrix parameters used in this paper are taken from a global analysis of $\pi^+\pi^-$ scattering data [22]. Masses and coupling constants are in units of MeV/c^2.

m_α	$g^\alpha_{\pi^+\pi^-}$	$g^\alpha_{K\bar{K}}$	$g^\alpha_{4\pi}$	$g^\alpha_{\eta\eta}$	$g^\alpha_{\eta\eta'}$
0.65100	0.22889	−0.55377	0.00000	−0.39899	−0.34639
1.20360	0.94128	0.55095	0.00000	0.39065	0.31503
1.55817	0.36856	0.23888	0.55639	0.18340	0.18681
1.21000	0.33650	0.40907	0.85679	0.19906	−0.00984
1.82206	0.18171	−0.17558	−0.79658	−0.00355	0.22358
	$f^{\rm scatt}_{11}$	$f^{\rm scatt}_{12}$	$f^{\rm scatt}_{13}$	$f^{\rm scatt}_{14}$	$f^{\rm scatt}_{15}$
	0.23399	0.15044	−0.20545	0.32825	0.35412
	$s^{\rm scatt}_0$	$s^{\rm prod}_0$	s_{A0}	s_A	
	−3.92637	−3.0	−0.15	1	

fit of scattering data and is listed in Table II. The mass m_α is the bare pole mass and is in general different from the resonant mass of the RBW function. The parameters $f^{\rm scatt}_{ij}$ and $s^{\rm scatt}_0$ are used to describe smooth scattering processes. The last factor of the K-matrix, $\frac{1-s_{A0}}{s-s_{A0}}(s-\frac{s_A m_\pi^2}{2})$, regulates the singularities near the $\pi^+\pi^-$ threshold, the so-called "Adler zero" [85,86]. The Hermitian property of the K-matrix imposes the relation $f^{\rm scatt}_{ij}=f^{\rm scatt}_{ji}$, and since only $\pi^+\pi^-$ decays are considered, if $i\neq 1$ and $j\neq 1$, $f^{\rm scatt}_{ij}$ is set to 0. The production vector is modeled with

$$P_j=\left[f^{\rm prod}_{1j}\frac{1-s^{\rm prod}_0}{s-s^{\rm prod}_0}+\sum_\alpha\frac{\beta_\alpha g^\alpha_j}{m^2_\alpha-s}\right], \tag{25}$$

where $f^{\rm prod}_{1j}$ and β_α are free parameters. The singularities in the K-matrix and the production vector cancel when calculating the amplitude matrix element.

V. DALITZ PLOT FIT

An unbinned extended maximum likelihood fit is performed to the Dalitz plot distribution. The likelihood function is defined by

$$\mathcal{L}=\mathcal{L}'\times\frac{1}{\sqrt{2\pi}\sigma_s}\exp\left(-\frac{(\nu_s-\nu^0_s)^2}{2\sigma^2_s}\right)\times\frac{1}{\sqrt{2\pi}\sigma_b}\exp\left(-\frac{(\nu_b-\nu^0_b)^2}{2\sigma^2_b}\right), \tag{26}$$

where

$$\mathcal{L}'=\frac{e^{-(\nu_s+\nu_b)}(\nu_s+\nu_b)^N}{N!}\times\prod_{i=1}^{N}\left[\frac{\nu_s}{\nu_s+\nu_b}f_s(\vec{x}_i;\theta_s)+\frac{\nu_b}{\nu_s+\nu_b}f_b(\vec{x}_i;\theta_b)\right]. \tag{27}$$

The background probability density function (PDF) is given by $f_b(\vec{x};\theta_b)$ and is described in Sec. V A. The signal PDF, $f_s(\vec{x}_i;\theta_s)$, is described by

$$\frac{M(\vec{x}_i;\theta_s)\varepsilon(\vec{x}_i)}{\int M(\vec{x};\theta_s)\varepsilon(\vec{x})d\vec{x}}, \tag{28}$$

where the decay amplitude, $M(\vec{x};\theta_s)$, is described in Sec. IV and the efficiency variation over the Dalitz plot, $\varepsilon(\vec{x})$, is described in Sec. V B. The fit parameters, θ_s and θ_b, include complex coefficients and resonant parameters like masses and widths. The value N is the total number of reconstructed candidates in the signal region. The number of signal and background events, ν_s and ν_b, are floated and constrained by the yields, ν^0_s and ν^0_b, determined by the $\bar{D}^0\pi^+\pi^-$ mass fit and shown with their statistical uncertainties in Table I.

A. Background modeling

The only significant source of candidates in the signal region, other than $B^0\to\bar{D}^0\pi^+\pi^-$ decays, is from combinatorial background. It is modeled using candidates in the upper $m(\bar{D}^0\pi^+\pi^-)$ sideband ([5350, 5450] MeV/c^2) with a looser requirement on the Fisher discriminant, and is shown in Fig. 3. The looser requirement gives a similar distribution in the Dalitz plane but with lower statistical fluctuations. The Dalitz plot distribution of the combinatorial background events lying in the upper-mass sideband is considered to provide a reliable description of that in the signal region, as no dependence on $m(\bar{D}^0\pi^+\pi^-)$ is found by studying the Dalitz distribution in a different upper-mass sideband region. The combinatorial background is modeled with an interpolated nonparametric PDF [87,88] using an adaptive kernel-estimation algorithm [89].

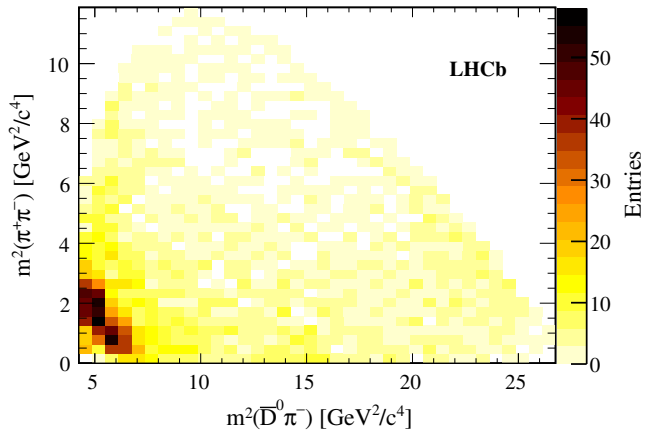

FIG. 3 (color online). Density profile of the combinatorial background events in the Dalitz plane obtained from the upper $m(\bar{D}^0\pi^+\pi^-)$ sideband with a looser selection applied on the Fisher discriminant.

B. Efficiency modeling

The efficiency function $\varepsilon(\vec{x})$ accounts for effects of reconstruction, triggering and selection of the $B^0 \to \bar{D}^0\pi^+\pi^-$ signal events, and varies across the Dalitz plane. Two simulated samples are generated to describe its variation with several data-driven corrections. One is uniformly distributed over the phase space of the Dalitz plot and the other is uniformly distributed over the square Dalitz plot, which models efficiencies more precisely at the kinematic boundaries. The square Dalitz plot is parametrized by two variables m' and θ' that each varies between 0 and 1 and are defined as

$$m' = \frac{1}{\pi}\arccos\left(2\frac{m(\pi^+\pi^-) - m(\pi^+\pi^-)_{\rm min}}{m(\pi^+\pi^-)_{\rm max} - m(\pi^+\pi^-)_{\rm min}} - 1\right)$$
$$\text{and} \quad \theta' = \frac{1}{\pi}\theta(\pi^+\pi^-), \tag{29}$$

where $m(\pi^+\pi^-)_{\rm max} = m_{B^0} - m_{D^0}$, $m(\pi^+\pi^-)_{\rm min} = 2m_\pi$ and $\theta(\pi^+\pi^-)$ is the helicity angle of the $\pi^+\pi^-$ system.

The two samples are fitted simultaneously with common fit parameters. A fourth-order polynomial function is used to describe the efficiency variation over the Dalitz plot. As the efficiency in the simulation is approximately symmetric over $m^2(\bar{D}^0\pi^+)$ and $m^2(\bar{D}^0\pi^-)$, the polynomial function is defined as

$$\begin{aligned}\varepsilon(x,y) \propto\ & 1.0 + a_0(x+y) + a_1(x+y)^2 + a_2(xy) \\ & + a_3(x+y)^3 + a_4(x+y)xy + a_5(x+y)^4 \\ & + a_6(x+y)^2xy + a_7x^2y^2,\end{aligned} \tag{30}$$

where

$$x = \frac{m^2(\bar{D}^0\pi^+) - m_0^2}{(m_{B^0} - m_\pi)^2 - m_0^2} \quad \text{and} \quad y = \frac{m^2(\bar{D}^0\pi^-) - m_0^2}{(m_{B^0} - m_\pi)^2 - m_0^2}, \tag{31}$$

with m_0^2 defined as $[(m_{D^0} + m_\pi)^2 + (m_{B^0} - m_\pi)^2]/2$. The fitted efficiency distribution over the Dalitz plane is shown in Fig. 4.

The efficiency is corrected using dedicated control samples with data-driven methods. The corrections applied to the simulated samples include known differences between simulation and data that originate from the trigger, PID and tracking.

C. Results of the Dalitz plot fit

The Dalitz plot distribution from data in the signal region is shown in Fig. 5. The analysis is performed using the isobar model and the K-matrix model. The nominal fit model in each case is defined by considering many possible resonances and removing those that do not significantly contribute to the Dalitz plot analysis. The resulting resonant

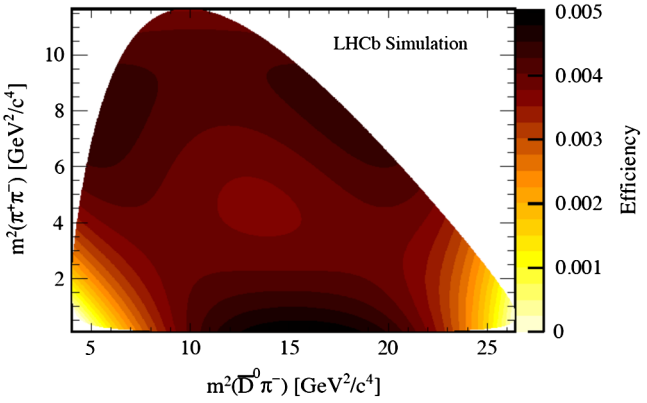

FIG. 4 (color online). Efficiency function for the Dalitz variables obtained in a fit to the LHCb simulated samples.

contributions are given in Table III while the projections of the fit results are shown in Fig. 6 (Fig. 7) for the isobar (K-matrix) model.

The comparisons of the S-wave results for the isobar model and the K-matrix model are shown in Fig. 8. The results from the two models agree reasonably well for the amplitudes and phases. In the $\pi^+\pi^-$ mass-squared region of $[1.5, 4.0]$ GeV$^2/c^4$, small structures are seen in the K-matrix model, indicating possible contributions from $f_0(1370)$ and $f_0(1500)$ states. These contributions are not significant in the isobar model and are thus not included in the nominal fit: adding them results in marginal changes and shows similar qualitative behavior to the K-matrix model as displayed in Fig. 8. The measured S-waves from both models qualitatively agree with predictions given in Ref. [91].

To see more clearly the resonant contributions in the region of the $\rho(770)$ resonance, the data are plotted in the $\pi^+\pi^-$ invariant mass-squared region $[0.0, 2.1]$ GeV$^2/c^4$ in

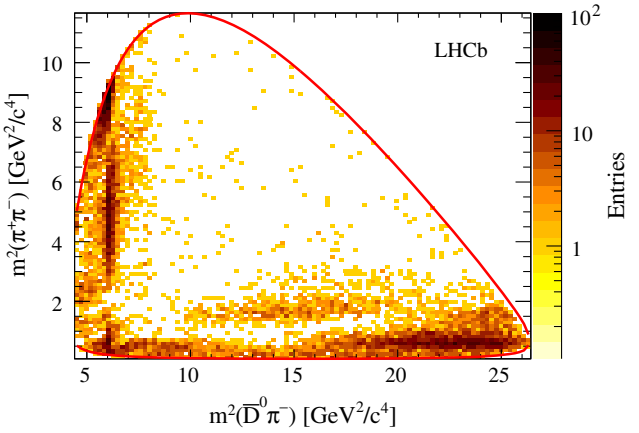

FIG. 5 (color online). Dalitz plot distribution of candidates in the signal region, including background contributions. The red line shows the Dalitz plot kinematic boundary.

TABLE III. Resonant contributions to the nominal fit models and their properties. Parameters and uncertainties of $\rho(770)$, $\omega(782)$, $\rho(1450)$ and $\rho(1700)$ come from Ref. [90], and those of $f_2(1270)$ and $f_0(2020)$ come from Ref. [32]. Parameters of $f_0(500)$, $f_0(980)$ and K-matrix formalism are described in Sec. IV.

Resonance	Spin	Model	m_r (MeV/c^2)	Γ_0 (MeV)
$\bar{D}^0\pi^-$ P-wave	1	Eq. (14)	Floated	
$D_0^*(2400)^-$	0	RBW	Floated	
$D_2^*(2460)^-$	2	RBW	Floated	
$D_J^*(2760)^-$	3	RBW	Floated	
$\rho(770)$	1	GS	775.02 ± 0.35	149.59 ± 0.67
$\omega(782)$	1	Eq. (13)	781.91 ± 0.24	8.13 ± 0.45
$\rho(1450)$	1	GS	1493 ± 15	427 ± 31
$\rho(1700)$	1	GS	1861 ± 17	316 ± 26
$f_2(1270)$	2	RBW	1275.1 ± 1.2	$185.1^{+2.9}_{-2.4}$
$\pi\pi$ S-wave	0	K-matrix	See Sec. IV	
$f_0(500)$	0	Eq. (15)	See Sec. IV	
$f_0(980)$	0	Eq. (18)	See Sec. IV	
$f_0(2020)$	0	RBW	1992 ± 16	442 ± 60
Nonresonant	0	Eq. (20)	See Sec. IV	

Fig. 9. In the region around 0.6 GeV$^2/c^4$, interference between the $\rho(770)$ and $\omega(782)$ resonances is evident. In the $\pi^+\pi^-$ S-wave distributions of both the isobar model and the K-matrix model, a peaking structure is seen in the region $[0.9, 1.0]$ GeV$^2/c^4$, which corresponds to the $f_0(980)$ resonance. The structure in the region $[1.3, 1.8]$ GeV$^2/c^4$ corresponds to the spin-2 $f_2(1270)$ resonance.

Distributions in the invariant mass-squared region $[6.4, 10.4]$ GeV$^2/c^4$ of $m^2(\bar{D}^0\pi^-)$ are shown in Fig. 10. There is a significant contribution from the $D_J^*(2760)^-$ resonance observed in Ref. [29] and a spin-3 assignment gives the best description. A detailed discussion on the determination of the spin of $D_J^*(2760)$ is provided in Sec. VIII B.

The fit quality is evaluated by determining a χ^2 value by comparing the data and the fit model in $N_{\rm bins} = 256$ bins that are defined adaptively to ensure approximately equal population with a minimum bin content of 37 entries. A value of 287 (296) is found for the isobar (K-Matrix) model based on statistical uncertainties only.

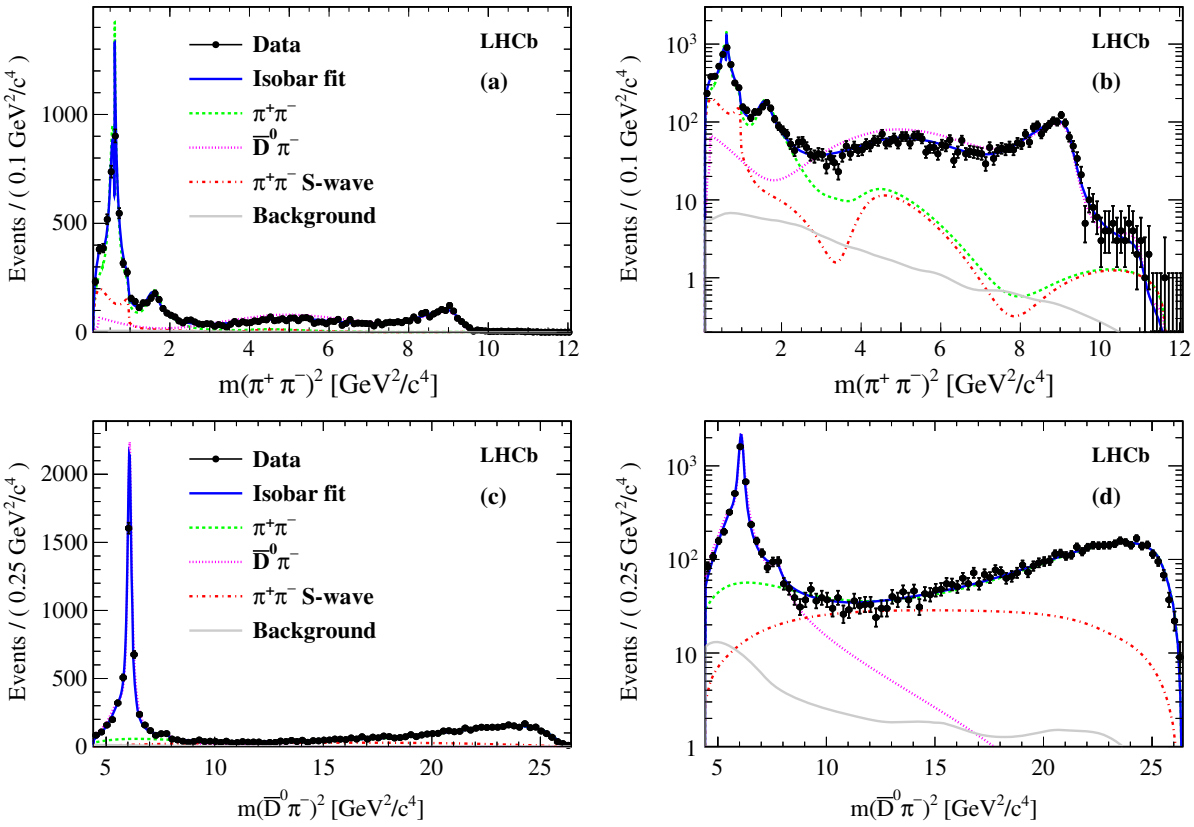

FIG. 6 (color online). Projections of the data and isobar fit onto (a) $m^2(\pi^+\pi^-)$ and (c) $m^2(\bar{D}^0\pi^-)$ with a linear scale. Same projections shown in (b) and (d) with a logarithmic scale. Components are described in the legend. The lines denoted $\bar{D}^0\pi^-$ and $\pi^+\pi^-$ include the coherent sums of all $\bar{D}^0\pi^-$ resonances, $\pi^+\pi^-$ resonances, and $\pi^+\pi^-$ S-wave resonances. The various contributions do not add linearly due to interference effects.

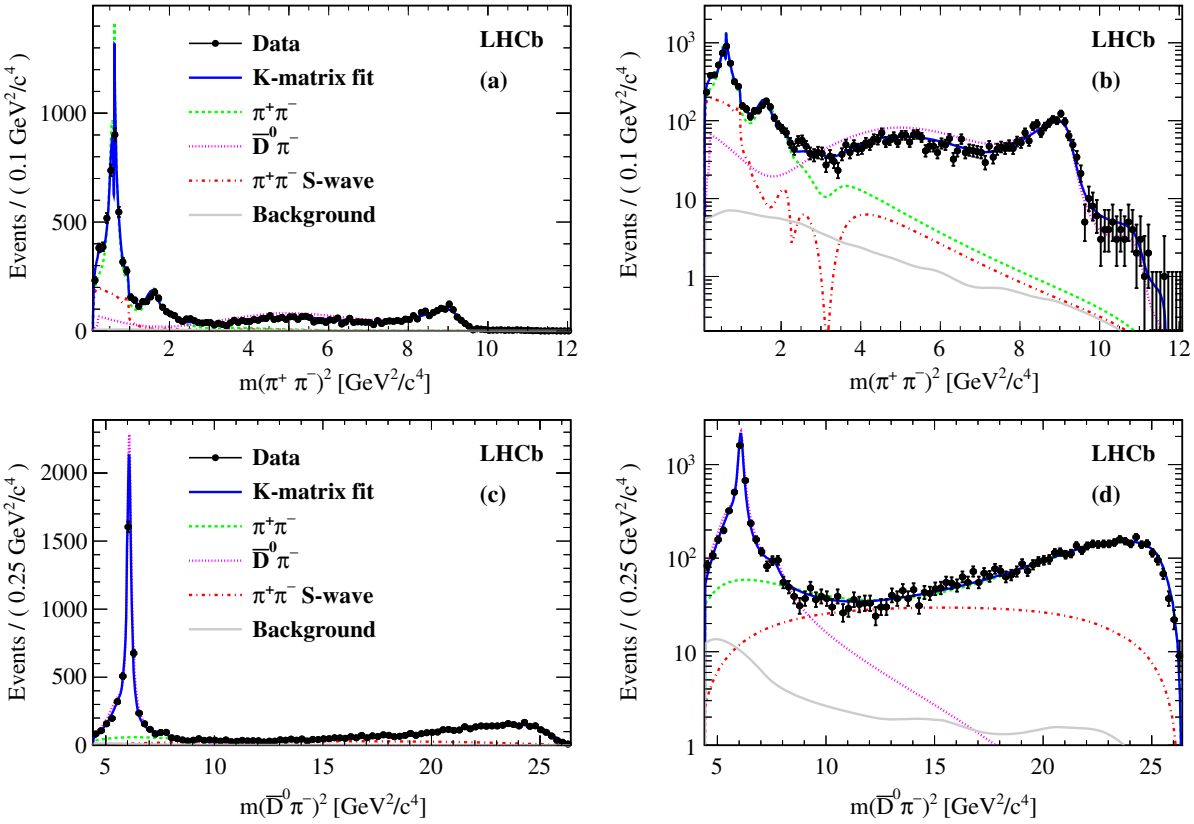

FIG. 7 (color online). Projections of the data and K-matrix fit onto (a) $m^2(\pi^+\pi^-)$ and (c) $m^2(\bar{D}^0\pi^-)$ with a linear scale. Same projections shown in (b) and (d) with a logarithmic scale. Components are described in the legend. The lines denoted $\bar{D}^0\pi^-$ and $\pi^+\pi^-$ include the coherent sums of all $\bar{D}^0\pi^-$ resonances, $\pi^+\pi^-$ resonances, and $\pi^+\pi^-$ S-wave resonances. The various contributions do not add linearly due to interference effects.

The effective number of degrees of freedom (nDoF) of the χ^2 is bounded by $N_{\text{bins}} - 1$ and $N_{\text{bins}} - N_{\text{pars}} - 1$, where N_{pars} is the number of parameters determined by the data. Pseudoexperiments give an effective number of 234 (235) nDoF.

Further checks of the consistency between the fitted models and the data are performed with the unnormalized Legendre polynomial weighted moments as a function of $m^2(\bar{D}^0\pi^-)$ and $m^2(\pi^+\pi^-)$. The corresponding distributions are shown in Appendix A.

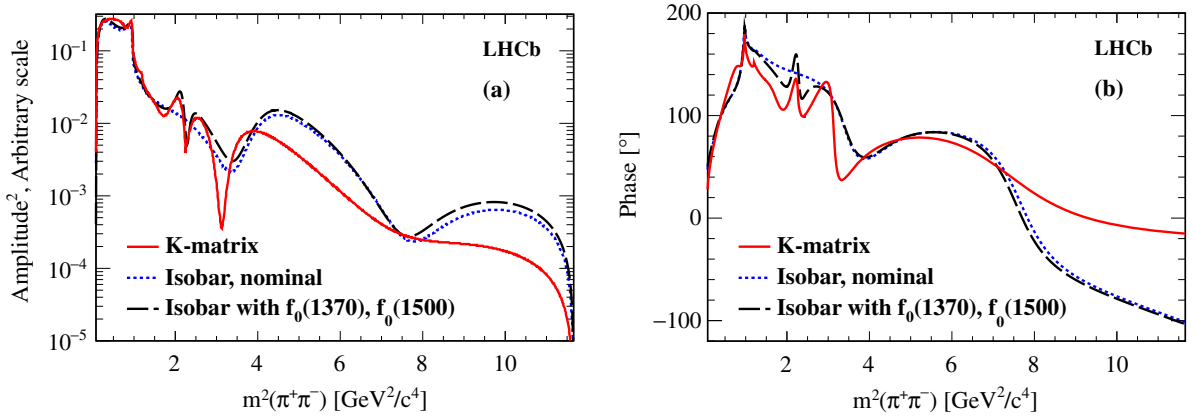

FIG. 8 (color online). Comparison of the $\pi^+\pi^-$ S-wave obtained from the isobar model and the K-matrix model, for (a) amplitudes and (b) phases. The K-matrix model is shown by the red solid line; two scenarios for the isobar model with (black long dashed line) and without (blue dashed line) $f_0(1370)$ and $f_0(1500)$ are shown.

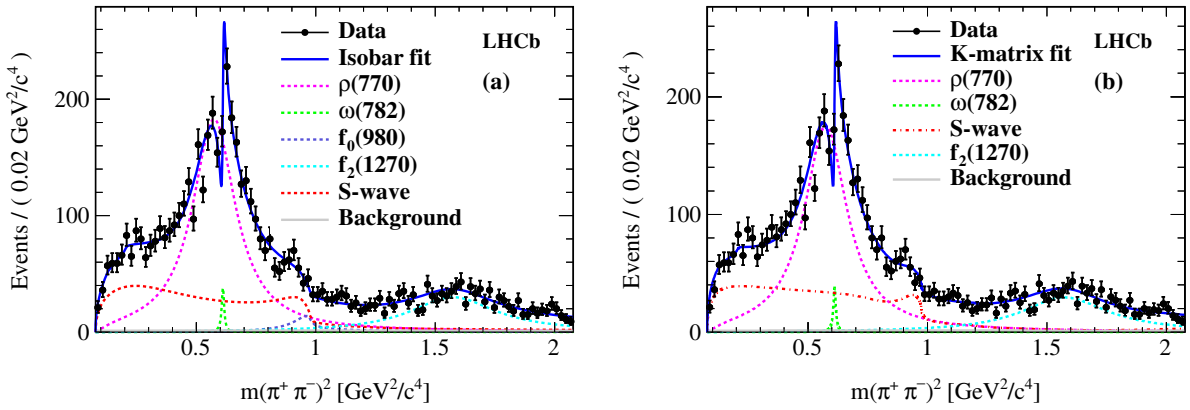

FIG. 9 (color online). Distributions of $m^2(\pi^+\pi^-)$ in the $\rho(770)$ mass region. The different fit components are described in the legend. Results from (a) the isobar model and (b) the K-matrix model are shown.

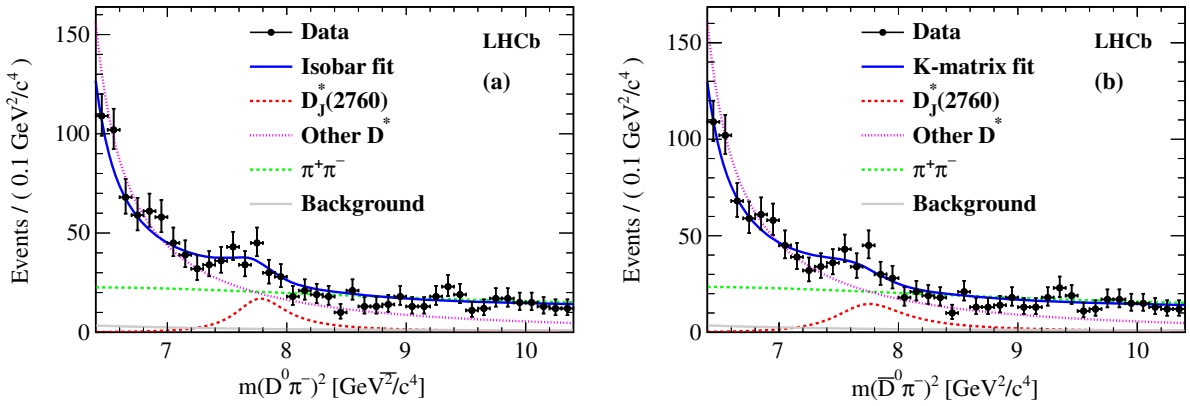

FIG. 10 (color online). Distributions of $m^2(\bar{D}^0\pi^-)$ in the $D_J^*(2760)^-$ mass region. The different fit components are described in the legend. Both results from (a) the isobar model and (b) the K-matrix model are shown.

VI. MEASUREMENT OF THE $B^0 \to \bar{D}^0\pi^+\pi^-$ BRANCHING FRACTION

Measuring the branching fractions of the different resonant contributions requires knowledge of the $B^0 \to \bar{D}^0\pi^+\pi^-$ branching fraction. This branching fraction is normalized relative to the $B^0 \to D^*(2010)^-\pi^+$ decay that has the same final state, so systematic uncertainties are reduced. Identical selections are applied to select $B^0 \to D^*(2010)^-\pi^+$ and $B^0 \to \bar{D}^0\pi^+\pi^-$ candidates, the only difference being that $m(\bar{D}^0\pi^-) < 2.1$ GeV/c^2 is used to select $D^*(2010)^-$ candidates. The kinematic constraints remove backgrounds from doubly misidentified $\bar{D}^0 \to K^+\pi^-$ or doubly Cabibbo-suppressed $\bar{D}^0 \to K^-\pi^+$ decays and no requirement is applied on $m(\bar{D}^0\pi^+)$.

The invariant mass distributions of $m(\bar{D}^0\pi^-)$ and $m(\bar{D}^0\pi^+\pi^-)$ for the $B^0 \to D^*(2010)^-\pi^+$ candidates are shown in Fig. 11 and are fitted simultaneously to determine the signal and background contributions. The $D^*(2010)^-$ signal distribution is modeled by three Gaussian functions to account for resolution effects while its background is modeled by a phase-space factor. The modeling of the signal and background shapes in the $m(\bar{D}^0\pi^+\pi^-)$ distribution are described in Sec. III. The $B^0 \to D^*(2010)^-\pi^+$ yield in the signal region is 7327 ± 85.

The efficiencies for selecting $B^0 \to D^*(2010)^-\pi^+$ and $B^0 \to \bar{D}^0\pi^+\pi^-$ decays are obtained from simulated samples. To take into account the resonant distributions in the Dalitz plot, the $B^0 \to \bar{D}^0\pi^+\pi^-$ simulated sample is weighted using the model described in the previous sections. The average efficiencies are $(1.72 \pm 0.05) \times 10^{-4}$ and $(4.96 \pm 0.05) \times 10^{-4}$ for the $B^0 \to D^*(2010)^-\pi^+$ and $B^0 \to \bar{D}^0\pi^+\pi^-$ decays.

Using the branching fractions of $\mathcal{B}(B^0 \to D^*(2010)^-\pi^+) = (2.76 \pm 0.13) \times 10^{-3}$ and $\mathcal{B}(D^*(2010)^- \to \bar{D}^0\pi^-) = (67.7 \pm 0.5)\%$ [32], the derived branching fraction of $B^0 \to \bar{D}^0\pi^+\pi^-$ in the kinematic region $m(\bar{D}^0\pi^\pm) > 2.1$ GeV/c^2 is $(8.46 \pm 0.14 \pm 0.40) \times 10^{-4}$, where the first uncertainty is statistical and the second uncertainty comes from the branching fraction of the normalization channel.

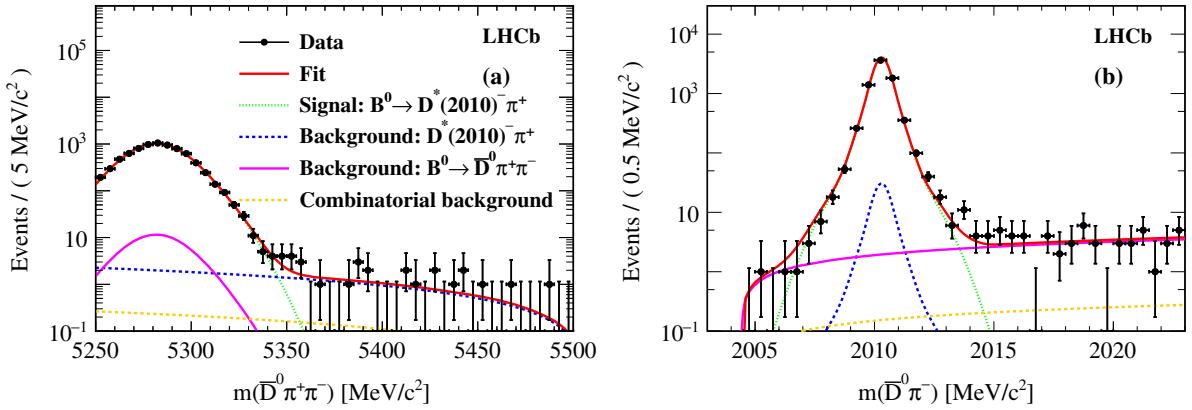

FIG. 11 (color online). Invariant mass distributions of (a) $m(\bar{D}^0\pi^+\pi^-)$ and (b) $m(\bar{D}^0\pi^-)$ for $B^0 \to D^*(2010)^-\pi^+$ candidates. The data are shown as black points with the fit superimposed as red solid lines.

VII. SYSTEMATIC UNCERTAINTIES

A. Common systematic uncertainties and checks

Two categories of systematic uncertainties are considered, each of which is quoted separately. They originate from the imperfect knowledge of the experimental conditions and from the assumptions made in the Dalitz plot fit model. The Dalitz model-dependent uncertainties also account for the precision on the external parameters. The various sources are assumed to be independent and summed in quadrature to give the total.

Experimental systematic uncertainties arise from the efficiency and background modeling and from the veto on the $D^*(2010)^-$ resonance. Those corresponding to the signal efficiency are due to imperfect estimations of PID, trigger, tracking reconstruction effects, and to the finite size of the simulated samples. Each of these effects is evaluated by the differences between the results using efficiencies computed from the simulation and from the data-driven methods. The systematic uncertainties corresponding to the modeling of the small residual background are estimated by using different subsamples of backgrounds. The systematic uncertainty due to the veto on the $D^*(2010)^-$ resonance is assigned by changing the selection requirement from $m^2(\bar{D}^0\pi^\pm) > 2.10\ \mathrm{GeV}/c^2$ to $2.05\ \mathrm{GeV}/c^2$.

The systematic uncertainties related to the Dalitz models considered (see Sec. IV) include effects from other possible resonant contributions that are not included in the nominal fit, from the modeling of resonant line shapes and from imperfect knowledge of the parameters of the modeling, i.e., the masses and widths of the $\pi^+\pi^-$ resonances considered, and the resonant radius.

The nonsignificant resonances added to the model for systematic studies are the $f_0(1300)$, $f_0(1500)$, $f_2'(1525)$, and $D^*(2650)^-$ [$f_2'(1525)$ and $D^*(2650)^-$] mesons for the isobar (K-matrix) model [29,32,48,49]. The spin of the $D^*(2650)^-$ resonance is set to 1. The differences between each alternative model and the nominal model are conservatively assigned as systematic uncertainties.

The radius of the resonances (r_{BW}) is set to a unique value of $1.6\ \mathrm{GeV}^{-1} \times \hbar c$ in the nominal fit. In the systematic studies, it is floated as a free parameter and its best fit value is $1.84 \pm 0.05\ \mathrm{GeV}^{-1} \times \hbar c$ ($1.92 \pm 0.31\ \mathrm{GeV}^{-1} \times \hbar c$) for the isobar (K-matrix) model. The value $1.85\ \mathrm{GeV}^{-1} \times \hbar c$ is chosen to estimate the systematic uncertainties due to the imperfect knowledge of this parameter.

The masses and widths of the $\pi^+\pi^-$ resonances considered are treated as free parameters with Gaussian constraints according to the inputs listed in Table III. The differences between the results from those fits and those of the nominal fits are assigned as systematic uncertainties.

For the isobar model, additional systematic uncertainties due to the modeling of the $f_0(500)$ and $f_0(980)$ resonances are considered. The Bugg model [83] for the $f_0(500)$ resonance and the Flatté model [84] for the $f_0(980)$ resonance, used in the nominal fit, are replaced by more conventional RBW functions. The masses and widths, left as free parameters, give $553 \pm 15\ \mathrm{MeV}/c^2$ and 562 ± 39 MeV for the $f_0(500)$ meson and $981 \pm 13\ \mathrm{MeV}/c^2$ and 191 ± 39 MeV for the $f_0(980)$ meson. The resulting differences to the nominal fit are assigned as systematic uncertainties.

The kinematic variables are calculated with the masses of the $\bar{D}^0$ and B^0 mesons constrained to their known values [32]. These kinematic constraints affect the extraction of the masses and widths of the $\bar{D}^0\pi^-$ resonances. The current world average value for the B^0 meson mass is $5279.58 \pm 0.17\ \mathrm{MeV}/c^2$ and for the $\bar{D}^0$ meson is $1864.84 \pm 0.07\ \mathrm{MeV}/c^2$ [32]. A conservative and direct estimation of the systematic uncertainties on the masses and widths of the $\bar{D}^0\pi^-$ resonances is provided by the sum in quadrature of the B^0 and $\bar{D}^0$ mass uncertainties. The effects of mass constraints are found to be negligible for the fit fractions, moduli and phases of the complex coefficients.

The systematic uncertainties are summarized for the isobar (K-matrix) model Dalitz analysis in Appendix B. Systematic uncertainties related to the measurements performed with the isobar formalism are listed in

Tables XIV–XVII, while those for the K-matrix formalism are given in Tables XVIII–XXI. In most cases, the dominant systematic uncertainties are due to the $D^*(2010)^-$ veto and the model uncertainties related to other resonances not considered in the nominal fit. In the isobar model, the modeling of the $f_0(500)$ and $f_0(980)$ resonances also has non-negligible systematic effects.

Several cross-checks have been performed to study the stability of the results. The analysis was repeated for different Fisher discriminant selection criteria, different trigger requirements and different subsamples, corresponding to the two data-taking periods and to the two half-parts of the $\bar{D}^0\pi^+\pi^-$ invariant mass signal region, above and below the B^0 mass [32]. Results from those checks demonstrate good consistency with respect to the nominal fit results. No bias is seen; therefore no correction is applied, nor is any related uncertainty assigned.

B. Systematic uncertainties on the $B^0 \to \bar{D}^0\pi^+\pi^-$ branching fraction

The systematic uncertainties related to the measurement of the $B^0 \to \bar{D}^0\pi^+\pi^-$ branching fraction are listed in Table IV. The systematic uncertainties on the PID, trigger, reconstruction and statistics of the simulated samples are calculated in a similar way to those of the Dalitz plot analysis. Other systematic uncertainties are discussed below.

The systematic uncertainty on the modeling of the $\bar{D}^0\pi^-$ and $D^*(2010)^-\pi^+$ invariant mass distributions is estimated by counting the number of signal events in the B^0 signal region assuming a flat background contribution. The $D^*(2010)^-$ mass region is restricted to the range [2007, 2013] MeV/c^2 for this estimate. The calculated branching fraction is nearly identical to that from the mass fit and thus has a negligible contribution to the systematic uncertainty. The signal purity of $B^0 \to D^*(2010)^-\pi^+$ is more than 99%.

To account for the effect of resonant structures on the signal efficiency, the data sample is divided using an adaptive binning scheme. The average efficiency is calculated in a model-independent way as

$$\varepsilon_{\text{ave}} = \frac{\sum_i N_i}{\sum_i N_i/\varepsilon_i}, \tag{32}$$

where N_i is the number of events in bin i and ε_i is the average efficiency in bin i calculated from the efficiency model. The difference between this model-independent method and the nominal is assigned as a systematic uncertainty.

TABLE IV. Systematic uncertainties on $\mathcal{B}(B^0 \to \bar{D}^0\pi^+\pi^-)$.

Source	Uncertainty ($\times 10^{-4}$)
PID	0.02
Trigger	0.13
Reconstruction	< 0.01
Size of simulated sample	0.26
B^0, $D^*(2010)^-$ mass model	< 0.01
Dalitz structure	0.04
Total	0.29

VIII. RESULTS

A. Significance of resonances

The isobar and K-matrix models employed to describe the Dalitz plot of the $B^0 \to \bar{D}^0\pi^+\pi^-$ decay include all of the resonances listed in Table III. The statistical significances of well-established $\pi^+\pi^-$ resonances are calculated directly with their masses and widths fixed to the world averages. They are computed as the relative change of the minimum of the negative logarithm of the likelihood (NLL) function with and without a given resonance. Besides the $\pi^+\pi^-$ resonances listed in Table III, the significances of the $f_0(1370)$, $f_0(1500)$ and $f_2'(1525)$ are also given. The results, expressed as multiples of Gaussian standard deviations (σ), are summarized in Table V. All of the other $\pi^+\pi^-$ resonances not listed in this Table have large statistical significances, well above five standard deviations.

To test the significance of the $D_J^*(2760)^-$ state, where $J = 3$ (see Sec. VIII B), an ensemble of pseudoexperiments is generated with the same number of events as in the data sample, using parameters obtained from the fit with the $D_J^*(2760)^-$ resonance excluded. The difference of the minima of the NLL when fitting with and without $D_J^*(2760)^-$ is used as a test statistic. It corresponds to 11.4σ (11.5σ) for the isobar (K-matrix) model and confirms the observation of $D_J^*(2760)^-$ reported in Ref. [29]. The two other orbitally excited D resonances, $D_J^*(2650)^-$ and $D_J^*(3000)^-$, whose observations are presented in the same paper, are added into the nominal fit model with different spin hypotheses and tiny improvements are found. They also do not describe the data in the absence of the $D_J^*(2760)^-$. Those resonances are thus not confirmed by

TABLE V. Statistical significance (σ) of $\pi^+\pi^-$ resonances in the Dalitz plot analysis. For the statistically significant resonances, the effect of adding dominant systematic uncertainties is shown (see text).

Resonances	$\omega(782)$	$f_0(980)$	$f_0(1370)$	$\rho(1450)$	$f_0(1500)$	$f_2'(1525)$	$\rho(1700)$	$f_0(2020)$
Isobar	8.0	10.7	1.1	8.7	1.1	3.6	4.5	10.2
K-matrix	8.1	n/a	n/a	8.6	n/a	2.6	2.2	n/a
With systematic uncertainties	7.7	7.0	n/a	8.7	n/a	n/a	n/a	4.3

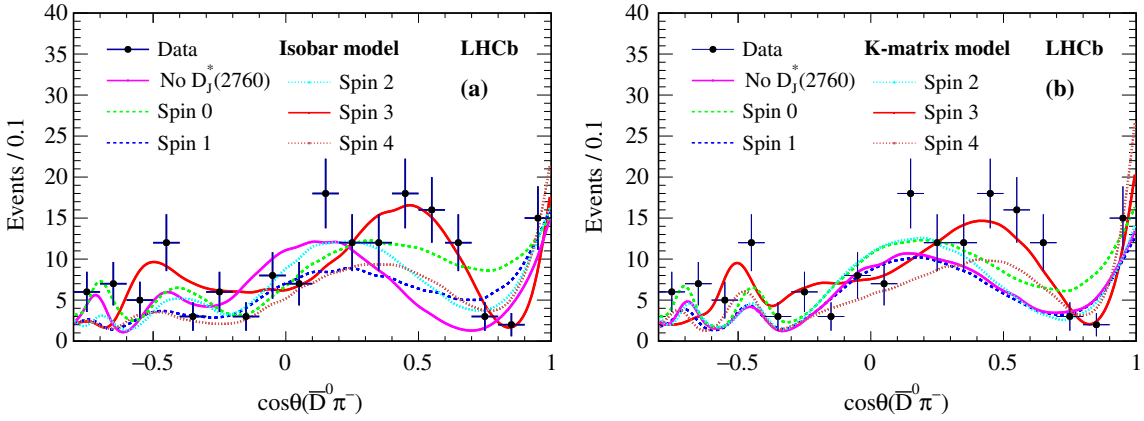

FIG. 12 (color online). Cosine of the helicity angle distributions in the $m^2(\bar{D}^0\pi^-)$ range $[7.4, 8.2]$ GeV$^2/c^4$ for (a) the isobar model and (b) the K-matrix model. The data are shown as black points. The helicity angle distributions of the Dalitz plot fit results, without the $D_J^*(2760)^-$ and with the different spin hypotheses of $D_J^*(2760)^-$, are superimposed.

this analysis. Finally, an extra $\bar{D}^0\pi^-$ resonance, with different spin hypotheses ($J = 0, 1, 2, 3, 4$) and with its mass and width allowed to vary, is added to the nominal fit model and no significant contribution is found.

The significance of each of the significant $\omega(782)$, $f_0(980)$, $\rho(1450)$, $f_0(2020)$ and $D_J^*(2760)^-$ states is checked while including the dominant systematic uncertainties (see Sec. VII A), namely, the modeling of the $f_0(500)$ and $f_0(980)$ resonances, the addition of other resonant contributions and the modification of the $D^*(2010)^-$ veto criteria. In all configurations, the significances of the $\omega(782)$, $f_0(980)$, $\rho(1450)$ and $D_J^*(2760)^-$ resonances are greater than 7.7σ, 7.0σ, 8.7σ, and 10.8σ, respectively. The significance of the $f_0(2020)$ drops to 4.3σ when using a RBW line shape for the $f_0(500)$ resonance. The abundant $f_0(500)$ contribution is highly significant under all of the applied changes.

B. Spin of resonances

As described in Sec. V C, a spin-3 $D_J^*(2760)^-$ contribution gives the best description of the data. To obtain the significance of the spin-3 hypothesis with respect to other spin hypotheses ($J = 0, 1, 2, 4$), test statistics are built. Their computations are based on the shift of the minimum of the NLL with respect to the nominal fit model when using different spin hypotheses. The mass and width of the $D_J^*(2760)^-$ resonance are floated in all the cases. Pseudoexperiments are generated using the fit parameters obtained using the other spin hypotheses. Significances are calculated according to the distributions obtained from the pseudoexperiments of the test statistic and its values from data. These studies indicate that data are inconsistent with other spin hypotheses by more than 10σ. Following the discovery of the $D_{sJ}^*(2860)^-$ meson, which is interpreted as the superposition of two particles with spin 1 and spin 3 [25,26], a similar configuration for the $D_J^*(2760)^-$ has been tested and is found to give no significant improvement in the description of the data. To illustrate the preference of the spin-3 hypothesis, the cosine of the helicity angle distributions in the mass-squared region of $[7.4, 8.2]$ GeV$^2/c^4$ for $m^2(\bar{D}^0\pi^-)$ are shown in Fig. 12 under the various scenarios. Based on our result, $D_J^*(2760)^-$ is interpreted as the $D_3^*(2760)^-$ meson. Recently, LHCb observed a neutral spin-1 $D^*(2760)^0$ state [92]. The current analysis does not preclude a charged spin-1 D^* state at around the same mass, but it is not sensitive to it with the current data sample size.

Studies have also been performed to validate the spin-0 hypothesis of the $D_0^*(2400)^-$ resonance, as the spin of this state has never previously been confirmed in experiment

TABLE VI. Measured masses (m in MeV$/c^2$) and widths (Γ in MeV) of the $D_0^*(2400)^-$, $D_2^*(2460)^-$ and $D_3^*(2760)^-$ resonances, where the first uncertainty is statistical, the second and the third are experimental and model-dependent systematic uncertainties, respectively.

		Isobar	K-matrix
$D_0^*(2400)$	m	$2349 \pm 6 \pm 1 \pm 4$	$2354 \pm 7 \pm 11 \pm 2$
	Γ	$217 \pm 13 \pm 5 \pm 12$	$230 \pm 15 \pm 18 \pm 11$
$D_2^*(2460)$	m	$2468.6 \pm 0.6 \pm 0.0 \pm 0.3$	$2468.1 \pm 0.6 \pm 0.4 \pm 0.3$
	Γ	$47.3 \pm 1.5 \pm 0.3 \pm 0.6$	$46.0 \pm 1.4 \pm 1.7 \pm 0.4$
$D_3^*(2760)$	m	$2798 \pm 7 \pm 1 \pm 7$	$2802 \pm 11 \pm 10 \pm 3$
	Γ	$105 \pm 18 \pm 6 \pm 23$	$154 \pm 27 \pm 13 \pm 9$

TABLE VII. The moduli of the complex coefficients of the resonant contributions for the isobar model and the K-matrix model. The first uncertainty is statistical, the second and the third are experimental and model-dependent systematic uncertainties, respectively.

Resonance	Isobar ($\lvert c_i\rvert$)	K-matrix ($\lvert c_i\rvert$)
Nonresonance	$3.43 \pm 0.22 \pm 0.04 \pm 0.51$	n/a
$f_0(500)$	$18.7 \pm 0.70 \pm 0.29 \pm 0.80$	n/a
$f_0(980)$	$2.62 \pm 0.25 \pm 0.09 \pm 0.46$	n/a
$f_0(2020)$	$4.41 \pm 0.51 \pm 0.21 \pm 1.78$	n/a
$\rho(770)$	1.0 (fixed)	1.0 (fixed)
$\omega(782)$	$0.30 \pm 0.04 \pm 0.00 \pm 0.01$	$0.31 \pm 0.04 \pm 0.01 \pm 0.01$
$\rho(1450)$	$0.23 \pm 0.03 \pm 0.01 \pm 0.02$	$0.28 \pm 0.03 \pm 0.08 \pm 0.01$
$\rho(1700)$	$0.078 \pm 0.016 \pm 0.006 \pm 0.008$	$0.136 \pm 0.020 \pm 0.077 \pm 0.011$
$f_2(1270)$	$0.072 \pm 0.002 \pm 0.000 \pm 0.005$	$0.073 \pm 0.002 \pm 0.006 \pm 0.003$
$\bar{D}^0\pi^-$ P-wave	$18.8 \pm 0.7 \pm 0.3 \pm 1.9$	$19.6 \pm 0.7 \pm 0.7 \pm 0.6$
$D_0^*(2400)^-$	$12.1 \pm 0.8 \pm 0.3 \pm 0.6$	$13.1 \pm 1.0 \pm 0.8 \pm 0.5$
$D_2^*(2460)^-$	$1.31 \pm 0.04 \pm 0.02 \pm 0.02$	$1.31 \pm 0.04 \pm 0.04 \pm 0.00$
$D_3^*(2760)^-$	$0.053^{+0.011}_{-0.006} \pm 0.003 \pm 0.008$	$0.075^{+0.016}_{-0.008} \pm 0.005 \pm 0.003$

[32]. When moving to other spin hypotheses, the minimum of the NLL increases by more than 250 units in all cases, which confirms the expectation of spin 0 unambiguously.

C. Results of the Dalitz plot analysis

The shape parameters of the $\pi^+\pi^-$ resonances are fixed from previous measurements except for the nonresonant contribution in the isobar model. The fitted value of the parameter α defined in Eq. (20) is -0.363 ± 0.027, which corresponds to a 10σ statistical significance compared to the case where there is no varying phase. An expansion of the model by including a varying phase in the $\bar{D}^0\pi^-$ axis is also investigated but no significantly varying phase in that system is seen. The results indicate a weak, but non-negligible, rescattering effect in the $\pi^+\pi^-$ states, while the rescattering in the $\bar{D}^0\pi^-$ states is not significant. The masses, widths and other shape parameters of the $\bar{D}^0\pi^-$ contributions are allowed to vary in the analysis. The values of the shape parameters of the $\bar{D}^0\pi^-$ P-wave component, defined in Eq. (14), are $\beta_1 = 0.95 \pm 0.05$ (0.90 ± 0.04) and $\beta_2 = 0.51 \pm 0.06$ (0.43 ± 0.05) for the isobar (K-matrix) model.

The measurements of the masses and widths of the three resonances $D_0^*(2400)^-$, $D_2^*(2460)^-$ and $D_3^*(2760)^-$ are listed in Table VI. The present precision on the mass and width of the $D_0^*(2400)^-$ resonance is improved with respect to Refs. [29,32]. The result for the width of the $D_2^*(2460)^-$ meson is consistent with previous measurements, whereas the result for the mass is above the world average which is dominated by the measurement using inclusive production by LHCb [29]. In the previous LHCb inclusive analysis, the broad $D_0^*(2400)^-$ component was excluded from the fit model due to a high correlation with the background line shape parameters, while here it is

TABLE VIII. The phase of the complex coefficients of the resonant contributions for the isobar model and the K-matrix model. The first uncertainty is statistical, the second and the third are experimental and model-dependent systematic uncertainties, respectively.

Resonance	Isobar [$\arg(c_i)°$]	K-matrix [$\arg(c_i)°$]
Nonresonance	$77.1 \pm 4.5 \pm 2.3 \pm 5.4$	n/a
$f_0(500)$	$38.4 \pm 2.7 \pm 1.3 \pm 3.7$	n/a
$f_0(980)$	$138.9 \pm 4.6 \pm 1.5 \pm 10.9$	n/a
$f_0(2020)$	$258.5 \pm 5.0 \pm 1.1 \pm 26.8$	n/a
$\rho(770)$	0.0 (fixed)	0.0 (fixed)
$\omega(782)$	$176.8 \pm 7.8 \pm 0.6 \pm 0.5$	$174.8 \pm 8.0 \pm 1.5 \pm 0.5$
$\rho(1450)$	$149.0 \pm 7.5 \pm 4.8 \pm 4.5$	$132.9 \pm 7.8 \pm 8.5 \pm 5.5$
$\rho(1700)$	$103.5 \pm 13.1 \pm 4.5 \pm 2.4$	$77.6 \pm 9.9 \pm 23.1 \pm 4.5$
$f_2(1270)$	$158.1 \pm 3.0 \pm 1.6 \pm 3.8$	$147.8 \pm 2.5 \pm 8.5 \pm 2.6$
$\bar{D}^0\pi^-$ P-wave	$266.7 \pm 3.7 \pm 0.3 \pm 7.1$	$261.0 \pm 4.0 \pm 3.3 \pm 6.7$
$D_0^*(2400)^-$	$83.6 \pm 4.4 \pm 2.8 \pm 4.6$	$78.4 \pm 4.1 \pm 11.5 \pm 1.7$
$D_2^*(2460)^-$	$262.9 \pm 2.9 \pm 0.8 \pm 3.0$	$257.4 \pm 3.4 \pm 0.7 \pm 1.9$
$D_3^*(2760)^-$	$91.1 \pm 6.7 \pm 1.4 \pm 5.1$	$92.7 \pm 7.3 \pm 15.2 \pm 2.3$

TABLE IX. The fit fractions of the resonant contributions for the isobar and K-matrix models with $m(\bar{D}^0\pi^\pm) > 2.1$ GeV/c^2. The first uncertainty is statistical, the second and the third are experimental and model-dependent systematic uncertainties, respectively.

Resonance	Isobar ($\mathcal{F}_i$ %)	K-matrix ($\mathcal{F}_i$ %)
Nonresonance	$2.82 \pm 0.34 \pm 0.07 \pm 0.80$	n/a
$f_0(500)$	$13.2 \pm 0.89 \pm 0.31 \pm 2.45$	n/a
$f_0(980)$	$1.56 \pm 0.29 \pm 0.11 \pm 0.54$	n/a
$f_0(2020)$	$1.58 \pm 0.36 \pm 0.15 \pm 1.00$	n/a
S-wave	$16.39 \pm 0.58 \pm 0.43 \pm 1.46$	$16.51 \pm 0.70 \pm 1.68 \pm 1.10$
$\rho(770)$	$37.54 \pm 1.00 \pm 0.61 \pm 0.98$	$36.15 \pm 1.00 \pm 2.13 \pm 0.79$
$\omega(782)$	$0.49 \pm 0.13 \pm 0.01 \pm 0.03$	$0.50 \pm 0.13 \pm 0.01 \pm 0.02$
$\rho(1450)$	$1.54 \pm 0.32 \pm 0.08 \pm 0.22$	$2.16 \pm 0.42 \pm 0.82 \pm 0.21$
$\rho(1700)$	$0.38^{+0.25}_{-0.12} \pm 0.07 \pm 0.06$	$0.83 \pm 0.21 \pm 0.61 \pm 0.12$
$f_2(1270)$	$10.28 \pm 0.49 \pm 0.31 \pm 1.10$	$9.88 \pm 0.58 \pm 0.83 \pm 0.58$
$\bar{D}^0\pi^-$ P-wave	$9.21 \pm 0.56 \pm 0.24 \pm 1.73$	$9.22 \pm 0.58 \pm 0.67 \pm 0.75$
$D_0^*(2400)^-$	$9.00 \pm 0.60 \pm 0.20 \pm 0.35$	$9.27 \pm 0.60 \pm 0.86 \pm 0.52$
$D_2^*(2460)^-$	$28.83 \pm 0.69 \pm 0.74 \pm 0.50$	$28.13 \pm 0.72 \pm 1.06 \pm 0.54$
$D_3^*(2760)^-$	$1.22 \pm 0.19 \pm 0.07 \pm 0.09$	$1.58 \pm 0.22 \pm 0.18 \pm 0.07$

included. The present result supersedes the former measurement. The Dalitz plot analysis used in this paper ensures that the background under the $D_2^*(2460)^-$ peak and the effect on the efficiency are under control, resulting in much lower systematic uncertainties compared to the inclusive approach.

The moduli and the phases of the complex coefficients of the resonant contributions, defined in Eq. (2), are displayed in Tables VII and VIII. Compatible results are obtained using both the isobar and K-matrix models. The results for the fit fractions are given in Table IX, while results for the interference fit fractions are given in Appendix C. Pseudoexperiments are used to validate the fitting procedure and no biases are found in the determination of parameter values.

D. Branching fractions

The measured branching fraction of the $B^0 \to \bar{D}^0\pi^+\pi^-$ decay in the phase-space region $m(\bar{D}^0\pi^\pm) > 2.1$ GeV/c^2 is

$$\mathcal{B}(B^0 \to \bar{D}^0\pi^+\pi^-) = (8.46 \pm 0.14 \pm 0.29 \pm 0.40) \times 10^{-4}, \tag{33}$$

taking into account the systematic uncertainties reported in Table IV. The first uncertainty is statistical, the second systematic, and the third the uncertainty from the branching fraction of the $B^0 \to D^*(2010)^-\pi^+$ normalization decay channel. The result agrees with the previous Belle measurement $(8.4 \pm 0.4 \pm 0.8) \times 10^{-4}$ [21] and the *BABAR* measurement $(8.81 \pm 0.18 \pm 0.76 \pm 0.78 \pm 0.11) \times 10^{-4}$ [22], obtained in a slightly larger phase-space region. A multiplicative factor of 94.5% (96.2%) is required to scale the Belle (*BABAR*) results to the same phase-space region as in this analysis.

The branching fraction of each quasi-two-body decay, $B^0 \to r_i h_3$, with $r_i \to h_1 h_2$, is given by

$$\mathcal{B}(B^0 \to r_i h_3) \times \mathcal{B}(r_i \to h_1 h_2) = \mathcal{B}(B^0 \to \bar{D}^0\pi^+\pi^-) \times \frac{\mathcal{F}_i}{\varepsilon_i^{\rm corr}}, \tag{34}$$

where the resonant states $(h_1 h_2) = (\bar{D}^0\pi^-), (\pi^+\pi^-)$. The fit fractions $\mathcal{F}_i$, defined in Eq. (3), are obtained from the Dalitz plot analysis and are listed in Table IX. The correction factors, $\varepsilon_i^{\rm corr}$, account for the cutoff due to the $D^*(2010)^-$ veto. They are obtained by generating pseudoexperiment samples for each resonance over the Dalitz plot and applying the same requirement $[m(\bar{D}^0\pi^\pm) > 2.1$ GeV/$c^2]$. They are summarized in Table X. The correction factors are the same for the isobar model and the K-matrix model. The effects due to the uncertainties of the masses and widths of the resonances are included in the uncertainties given in the table.

Using the overall $B^0 \to \bar{D}^0\pi^+\pi^-$ decay branching fraction, the fit fractions ($\mathcal{F}_i$) and the correction factors ($\varepsilon_i^{\rm corr}$),

TABLE X. Correction factors due to the $D^*(2010)^-$ veto.

Resonance	$\epsilon_i^{\rm corr}$ %
$f_0(500)$	99.52 ± 0.10
$f_0(980)$	98.74 ± 0.09
$f_0(2020)$	99.29 ± 0.05
S-wave	98.55 ± 0.04
$\rho(770)$	98.95 ± 0.03
$\omega(782)$	99.39 ± 0.02
$\rho(1450)$	95.66 ± 0.06
$\rho(1700)$	96.73 ± 0.06
$f_2(1270)$	91.91 ± 0.09
$D_0^*(2400)^-$	98.60 ± 0.10
$D_2^*(2460)^-$	100.
$D_3^*(2760)^-$	100.

TABLE XI. Measured branching fractions of $\mathcal{B}(B^0 \to r h_3) \times \mathcal{B}(r \to h_1 h_2)$ for the isobar and K-matrix models. The first uncertainty is statistical, the second the experimental systematic, the third the model-dependent systematic, and the fourth the uncertainty from the normalization $B^0 \to D^*(2010)^- \pi^+$ channel.

Resonance	Isobar ($\times 10^{-5}$)	K-matrix ($\times 10^{-5}$)
$f_0(500)$	$11.2 \pm 0.8 \pm 0.5 \pm 2.1 \pm 0.5$	n/a
$f_0(980)$	$1.34 \pm 0.25 \pm 0.10 \pm 0.46 \pm 0.06$	n/a
$f_0(2020)$	$1.35 \pm 0.31 \pm 0.14 \pm 0.85 \pm 0.06$	n/a
S-wave	$14.1 \pm 0.5 \pm 0.6 \pm 1.3 \pm 0.7$	$14.2 \pm 0.6 \pm 1.5 \pm 0.9 \pm 0.7$
$\rho(770)$	$32.1 \pm 1.0 \pm 1.2 \pm 0.9 \pm 1.5$	$31.0 \pm 1.0 \pm 2.1 \pm 0.7 \pm 1.5$
$\omega(782)$	$0.42 \pm 0.11 \pm 0.02 \pm 0.03 \pm 0.02$	$0.43 \pm 0.11 \pm 0.02 \pm 0.02 \pm 0.02$
$\rho(1450)$	$1.36 \pm 0.28 \pm 0.08 \pm 0.19 \pm 0.06$	$1.91 \pm 0.37 \pm 0.73 \pm 0.19 \pm 0.09$
$\rho(1700)$	$0.33 \pm 0.11 \pm 0.06 \pm 0.05 \pm 0.02$	$0.73 \pm 0.18 \pm 0.53 \pm 0.10 \pm 0.03$
$f_2(1270)$	$9.5 \pm 0.5 \pm 0.4 \pm 1.0 \pm 0.4$	$9.1 \pm 0.6 \pm 0.8 \pm 0.5 \pm 0.4$
$D_0^*(2400)^-$	$7.7 \pm 0.5 \pm 0.3 \pm 0.3 \pm 0.4$	$8.0 \pm 0.5 \pm 0.8 \pm 0.4 \pm 0.4$
$D_2^*(2460)^-$	$24.4 \pm 0.7 \pm 1.0 \pm 0.4 \pm 1.2$	$23.8 \pm 0.7 \pm 1.2 \pm 0.5 \pm 1.1$
$D_3^*(2760)^-$	$1.03 \pm 0.16 \pm 0.07 \pm 0.08 \pm 0.05$	$1.34 \pm 0.19 \pm 0.16 \pm 0.06 \pm 0.06$

the branching fractions of quasi-two-body decays are calculated in Table XI. The first observation of the decays $B^0 \to \bar{D}^0 f_0(500)$, $B^0 \to \bar{D}^0 f_0(980)$, $B^0 \to \bar{D}^0 \rho(1450)$, as well as $B^0 \to D_3^*(2760)^- \pi^+$, and the first evidence of $B^0 \to \bar{D}^0 f_0(2020)$ are reported. The present world averages [32] of the branching fractions $\mathcal{B}(B^0 \to \bar{D}^0 \rho(770)) \times \mathcal{B}(\rho(770) \to \pi^+\pi^-)$, $\mathcal{B}(B^0 \to \bar{D}^0 f_2(1270)) \times \mathcal{B}(f_2(1270) \to \pi^+\pi^-)$, $\mathcal{B}(B^0 \to D_0^*(2400)^- \pi^+) \times \mathcal{B}(D_0^*(2400)^- \to \bar{D}^0 \pi^-)$, and $\mathcal{B}(B^0 \to D_2^*(2460)^- \pi^+) \times \mathcal{B}(D_2^*(2460)^- \to \bar{D}^0 \pi^-)$ are improved considerably. When accounting for the branching fractions of the $\omega(782)$ and $f_2(1270)$ to $\pi^+\pi^-$, one obtains the following results for the isobar model:

$$\mathcal{B}(B^0 \to \bar{D}^0 \omega(782)) = (2.75 \pm 0.72 \pm 0.13 \pm 0.20 \pm 0.13^{+0.20}_{-0.23}) \times 10^{-4} \quad (35)$$

and

$$\mathcal{B}(B^0 \to \bar{D}^0 f_2(1270)) = (16.8 \pm 1.1 \pm 0.7 \pm 1.8 \pm 0.7^{+0.5}_{-0.2}) \times 10^{-5}. \quad (36)$$

For the K-matrix model, one obtains

$$\mathcal{B}(B^0 \to \bar{D}^0 \omega(782)) = (2.81 \pm 0.72 \pm 0.13 \pm 0.13 \pm 0.13^{+0.20}_{-0.24}) \times 10^{-4} \quad (37)$$

and

$$\mathcal{B}(B^0 \to \bar{D}^0 f_2(1270)) = (16.1 \pm 1.1 \pm 1.4 \pm 0.9 \pm 0.7^{+0.5}_{-0.2}) \times 10^{-5}. \quad (38)$$

In both models, the fifth uncertainty is due to knowledge of the $\pi^+\pi^-$ decay rates [32]. The results are consistent with the measurement of the decay $B^0 \to \bar{D}^0 \omega(782)$, using the dominant $\omega(782) \to \pi^+\pi^-\pi^0$ decay [32,40].

E. Structure of the $f_0(980)$ and $f_0(500)$ resonances

In the isobar model, significant contributions from both $B^0 \to \bar{D}^0 f_0(500)$ and $B^0 \to \bar{D}^0 f_0(980)$ decays are observed. The related branching fraction measurements can be used to obtain information on the substructure of the $f_0(980)$ and $f_0(500)$ resonances within the factorization approximation. As discussed in Sec. I, two models for the quark structure of those states are considered: $q\bar{q}$ or $[qq'][\bar{q}\,\bar{q}']$ (tetraquarks). In both models, mixing angles between different quark states are determined using our measurements. In the $q\bar{q}$ model, the mixing between $s\bar{s}$ and $u\bar{u}$ or $d\bar{d}$ can be written as

$$|f_0(980)\rangle = \cos\varphi_{\rm mix}|s\bar{s}\rangle + \sin\varphi_{\rm mix}|n\bar{n}\rangle, \quad (39)$$

$$|f_0(500)\rangle = -\sin\varphi_{\rm mix}|s\bar{s}\rangle + \cos\varphi_{\rm mix}|n\bar{n}\rangle, \quad (40)$$

where $|n\bar{n}\rangle \equiv (|u\bar{u}\rangle + |d\bar{d}\rangle)/\sqrt{2}$ and $\varphi_{\rm mix}$ is the mixing angle. In the $[qq'][\bar{q}\,\bar{q}']$ model, the mixing angle, $\omega_{\rm mix}$, is introduced and the mixing becomes

$$|f_0(980)\rangle = \cos\omega_{\rm mix}|n\bar{n}s\bar{s}\rangle + \sin\omega_{\rm mix}|u\bar{u}d\bar{d}\rangle, \quad (41)$$

$$|f_0(500)\rangle = -\sin\omega_{\rm mix}|n\bar{n}s\bar{s}\rangle + \cos\omega_{\rm mix}|u\bar{u}d\bar{d}\rangle. \quad (42)$$

In both cases, the following variable is defined:

$$r^f = \frac{\mathcal{B}(B^0 \to \bar{D}^0 f_0(980))}{\mathcal{B}(B^0 \to \bar{D}^0 f_0(500))} \times \frac{\Phi(500)}{\Phi(980)}, \quad (43)$$

where $\Phi(500)$ and $\Phi(980)$ are the integrals of the phase-space factors computed over the resonant line shapes and the phase-space factors are proportional to the momentum computed in the B^0 rest frame. The value of their ratio is $\Phi(500)/\Phi(980) = 1.02 \pm 0.05$.

TABLE XII. Systematic uncertainties on r^f. The sum in quadrature of the uncertainties is also reported.

Source	r^f
PID	0.001
Trigger	0.001
Reconstruction	< 0.001
Simulation statistic	0.001
Background model	0.001
$D^*(2010)^-$ veto	0.012
Additional resonances	0.007
RBW parameters	0.008
$\pi\pi$ resonant mass, width	0.011
$f_0(500)$ model	0.033
$f_0(980)$ model	0.028
Total	0.048

The value of the branching fraction $\mathcal{B}(f_0(500) \to \pi^+\pi^-) = 2/3$ is obtained from the isospin Clebsch-Gordan coefficients and assumes that there are only contributions from $\pi\pi$ final states. The ratio $\mathcal{B}(f_0(980) \to K^+K^-)/\mathcal{B}(f_0(980) \to \pi^+\pi^-) = 0.35^{+0.15}_{-0.14}$, obtained from an average of the measurements by the *BABAR* [93] and BES [94] collaborations, is used to estimate the branching fraction $\mathcal{B}(f_0(980) \to \pi^+\pi^-)$. Assuming that the $\pi\pi$ and KK decays are dominant in the $f_0(980)$ decays, $\mathcal{B}(f_0(980) \to \pi^+\pi^-) = 0.46 \pm 0.06$ is obtained. This gives

$$r^f = 0.177^{+0.066}_{-0.062},$$

taking into account the systematic uncertainties, as listed in Table XII.

The parameter r^f is related to the mixing angle by the equation

$$r^f = \tan^2\varphi_{\rm mix} \times \left|\frac{F(B^0 \to f_0(980))}{F(B^0 \to f_0(500))}\right|^2 \qquad (44)$$

in the $q\bar{q}$ model and by

$$r^f = \left|\frac{1-\sqrt{2}\tan\omega_{\rm mix}}{\tan\omega_{\rm mix}+\sqrt{2}}\right|^2 \times \left|\frac{F(B^0 \to f_0(980))}{F(B^0 \to f_0(500))}\right|^2 \qquad (45)$$

in the $[qq'][\bar{q}\,\bar{q}']$ tetraquark model [57,58]. The form factors $F(B^0 \to f_0(980))$ and $F(B^0 \to f_0(500))$ are evaluated at the four-momentum transfer squared equal to the square of the $\bar{D}^0$ mass. Finally, values of the mixing angles as a function of form factor ratio are obtained in Fig. 13 for the $q\bar{q}$ model and the $[qq'][\bar{q}\,\bar{q}']$ tetraquark model. Such angles have also been computed by LHCb for the decays $B^0_{(s)} \to J/\psi\pi^+\pi^-$ [47–49].

The expectation is that the ratio of form factors should be close to unity. However, LHCb has recently performed a search for the decay $B^0_s \to \bar{D}^0 f_0(980)$ [95]. The limit set on this decay is below the value expected in a simple model based on our measured value of $\mathcal{B}(B^0 \to \bar{D}^0 f_0(500))$ and assuming equal form factors. More complicated models may be needed in order to explain all results.

The above discussion is one possible interpretation of the results. Another possible mechanism [91,96] involves the generation of pseudoscalar resonances through the interactions of $\pi^+\pi^-$ mesons.

F. Isospin analysis of the $B \to D\rho$ system

The measured branching fraction of the $B^0 \to \bar{D}^0\rho(770)^0$ decay, presented in Table XI, can be used to perform an isospin analysis of the $B \to D\rho$ system. Isospin symmetry relates the amplitudes of the decays $B^+ \to \bar{D}^0\rho(770)^+$, $B^0 \to D^-\rho(770)^+$, and $B^0 \to \bar{D}^0\rho(770)^0$, which can be written as linear combinations of the isospin eigenstates A_I with $I = 1/2$ and $3/2$ [37,41]

$$\begin{aligned} A(\bar{D}^0\rho^+) &= \sqrt{3}A_{3/2}, \\ A(D^-\rho^+) &= \sqrt{1/3}A_{3/2} + \sqrt{2/3}A_{1/2}, \\ A(\bar{D}^0\rho^0) &= \sqrt{2/3}A_{3/2} - \sqrt{1/3}A_{1/2}, \end{aligned} \qquad (46)$$

leading to

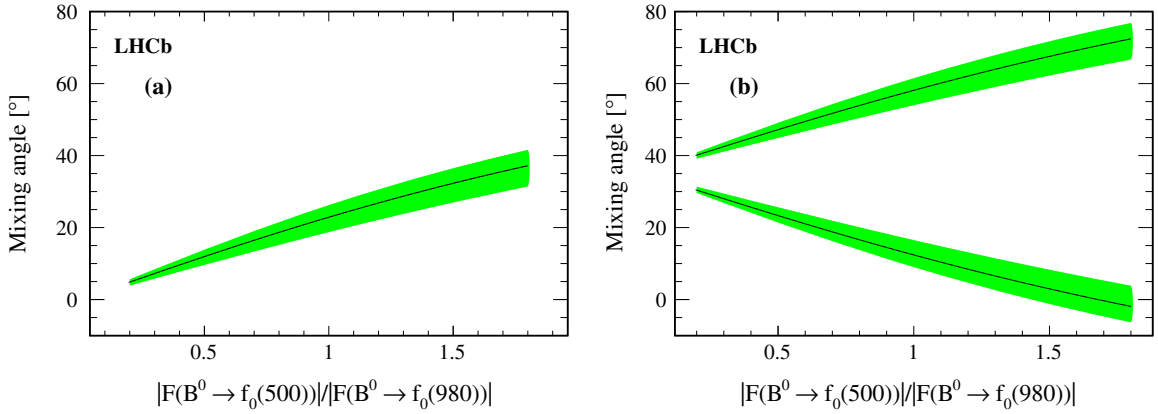

FIG. 13 (color online). Mixing angle as a function of form factor ratio for the (a) $q\bar{q}$ model and (b) $[qq'][\bar{q}\,\bar{q}']$ tetraquark model. The green band gives the 1σ interval around central values (black solid line).

TABLE XIII. Results of $R_{D\rho}$ and $\cos\delta_{D\rho}$.

Model	$R_{D\rho}$	$\cos\delta_{D\rho}$
Isobar	0.69 ± 0.15	$0.984^{+0.113}_{-0.048}$
K-matrix	0.69 ± 0.15	$0.987^{+0.114}_{-0.048}$

$$A(\bar{D}^0\rho^+) = A(D^-\rho^+) + \sqrt{2}A(\bar{D}^0\rho^0). \quad (47)$$

The strong phase difference between the amplitudes $A_{1/2}$ and $A_{3/2}$ is denoted by $\delta_{D\rho}$. Final-state interactions between the states $\bar{D}^0\rho^0$ and $D^-\rho^+$ may lead to a value of $\delta_{D\rho}$ different from zero and through constructive interference, to a larger value of $\mathcal{B}(B^0 \to \bar{D}^0\rho^0)$ than the prediction obtained within the factorization approximation. In the heavy-quark limit, the factorization model predicts [97,98] $\delta_{D\rho} = \mathcal{O}(\Lambda_{\rm QCD}/m_b)$ and the amplitude ratio $R_{D\rho} \equiv \frac{|A_{1/2}|}{\sqrt{2}|A_{3/2}|} = 1 + \mathcal{O}(\Lambda_{\rm QCD}/m_b)$, where m_b represents the b quark mass and $\Lambda_{\rm QCD}$ the QCD scale.

Using our measurement of $\mathcal{B}(B^0 \to \bar{D}^0\rho^0)$ together with the world average values of $\mathcal{B}(B^0 \to D^-\rho^+)$, $\mathcal{B}(B^+ \to \bar{D}^0\rho^+)$, and the ratio of lifetimes $\tau(B^+)/\tau(B^0)$ [32], we obtain

$$R_{D\rho} = \sqrt{\frac{1}{2}}\left(\frac{3(\mathcal{B}(D^-\rho^+) + \mathcal{B}(\bar{D}^0\rho^0))}{\mathcal{B}(\bar{D}^0\rho^+)} \times \frac{\tau_{B^+}}{\tau_{B^0}} - 1\right)^{1/2} \quad (48)$$

and

$$\cos\delta_{D\rho} = \frac{1}{4R_{D\rho}} \times \left(\frac{\tau_{B^+}}{\tau_{B^0}} \times \frac{3(\mathcal{B}(D^-\rho^+) - 2\mathcal{B}(\bar{D}^0\rho^0))}{\mathcal{B}(\bar{D}^0\rho^+)} + 1\right). \quad (49)$$

With a frequentist statistical approach [99], $R_{D\rho}$ and $\cos\delta_{D\rho}$ are calculated for the isobar and K-matrix models in Table XIII. These results are not significantly different from the predictions of factorization models. As opposed to the theoretical expectations [37,41] and in contrast to the $B \to D^{(*)}\pi$ system [40], nonfactorizable final-state interaction effects do not introduce a sizable phase difference between the isospin amplitudes in the $B \to D\rho$ system. The precision on $R_{D\rho}$ and $\cos\delta_{D\rho}$ is dominated by that of the branching fractions of the decays $B^+ \to \bar{D}^0\rho(770)^+$ (14%) and $B^0 \to D^-\rho(770)^+$ (17%) [32]. The precision of the branching fraction of the $B^0 \to \bar{D}^0\rho(770)^0$ decay is 7.3% (9.2%) for the isobar (K-matrix) model (see Table XI).

IX. CONCLUSION

A Dalitz plot analysis of the $B^0 \to \bar{D}^0\pi^+\pi^-$ decay is presented. The decay model contains four components from $\bar{D}^0\pi^-$ resonances, four P-wave $\pi^+\pi^-$ resonances and one D-wave $\pi^+\pi^-$ resonance. Two models are used to describe the S-wave $\pi^+\pi^-$ resonances. The isobar model uses four components, including the $f_0(500)$, $f_0(980)$, $f_0(2020)$ resonances and a nonresonant contribution. The K-matrix approach describes the $\pi^+\pi^-$ S-wave using a 5×5 scattering matrix with a production vector. The overall branching fraction of $B^0 \to \bar{D}^0\pi^+\pi^-$ and quasi-two-body decays are measured. Significant contributions from the $f_0(500)$, $f_0(980)$, $\rho(1450)$ and $D_3^*(2760)^-$ mesons are observed for the first time. For the latter, this is a confirmation of the observation from previous inclusive measurements, and the spin-parity of this resonance is determined for the first time to be $J^P = 3^-$. This suggests a spectroscopic assignment of $^3D_3$, and shows that the $1D$ family of charm resonances can be explored in the Dalitz plot analysis of B-meson decays in the same way as recently seen for the charm-strange resonances [25,26]. Evidence for the $f_0(2020)$ meson is also seen for the first time. The measured branching fractions of two-body decays are more precise than the existing world averages and there is good agreement between values from the isobar and K-matrix models.

The masses and widths of the $\bar{D}^0\pi^-$ resonances are also determined. The measured masses and widths of the $D_0^*(2400)^-$ and $D_3^*(2760)^-$ states are consistent with the previous measurements. The precision on the $D_0^*(2400)^-$ meson is much improved. For the measurement on the mass and width of the $D_2^*(2460)^-$ meson, the broad $D_0^*(2400)^-$ component was excluded from the fit model in the former LHCb inclusive analysis [29], due to a high correlation with the background line shape parameters, while here it is included. The present result therefore supersedes the former measurement.

The significant contributions found for both the $f_0(500)$ and $f_0(980)$ allow us to constrain the mixing angle between the $f_0(500)$ and $f_0(980)$ resonances. An isospin analysis in the $B \to D\rho$ decays using our improved measurement of the branching fraction of the decay $B^0 \to \bar{D}^0\rho^0$ is performed, indicating that nonfactorizable effects from final-state interactions are limited in the $D\rho$ system.

ACKNOWLEDGMENTS

We express our gratitude to our colleagues in the CERN accelerator departments for the excellent performance of the LHC. We thank the technical and administrative staff at the LHCb institutes. We acknowledge support from CERN and from the national agencies: CAPES, CNPq, FAPERJ and FINEP (Brazil); NSFC (China); CNRS/IN2P3 (France); BMBF, DFG, HGF and MPG (Germany); INFN (Italy); FOM and NWO (The Netherlands); MNiSW and NCN (Poland); MEN/IFA (Romania); MinES and FANO (Russia); MinECo (Spain); SNSF and SER (Switzerland); NASU (Ukraine); STFC (United Kingdom); NSF (USA). The Tier1 computing centers are supported by IN2P3

(France), KIT and BMBF (Germany), INFN (Italy), NWO and SURF (The Netherlands), PIC (Spain), GridPP (United Kingdom). We are indebted to the communities behind the multiple open source software packages on which we depend. We are also thankful for the computing resources and the access to software R&D tools provided by Yandex LLC (Russia). Individual groups or members have received support from EPLANET, Marie Skłodowska-Curie Actions

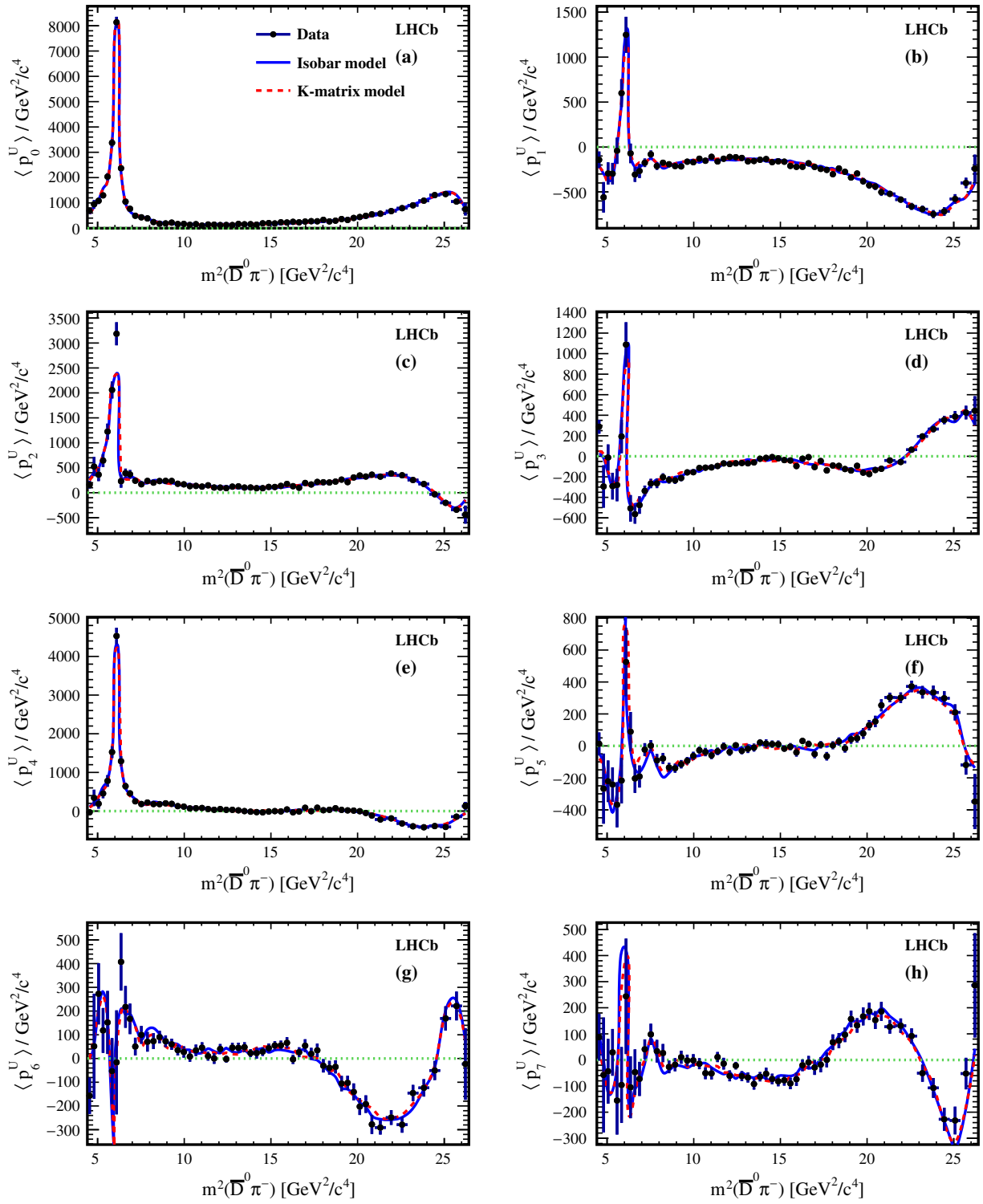

FIG. 14 (color online). The first eight unnormalized Legendre polynomial weighted moments [0 to 7 correspond to (a) to (h)] for background-subtracted and efficiency-corrected $B^0 \to \bar{D}^0\pi^+\pi^-$ data and the Dalitz plot fit results as a function of $m^2(\bar{D}^0\pi^-)$.

and ERC (European Union), Conseil général de Haute-Savoie, Labex ENIGMASS and OCEVU, Région Auvergne (France), RFBR (Russia), XuntaGal and GENCAT (Spain), Royal Society and Royal Commission for the Exhibition of 1851 (United Kingdom).

APPENDIX A: UNNORMALIZED LEGENDRE POLYNOMIAL WEIGHTED MOMENTS

Figures 14 and 15 show the distributions of the unnormalized Legendre polynomial weighted moments $\langle p_L^U \rangle$ which display the contributions of resonances with spin

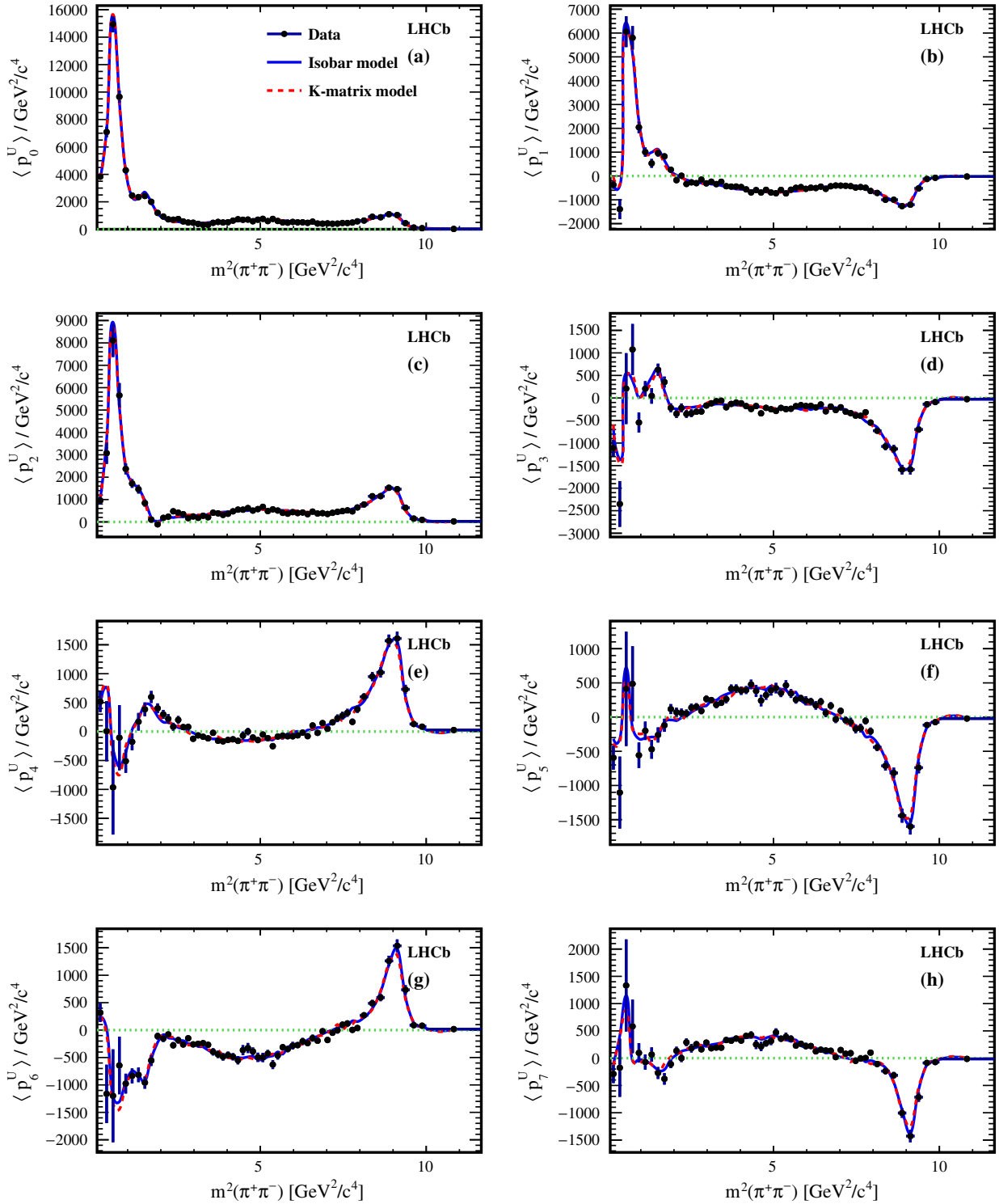

FIG. 15 (color online). The first eight unnormalized Legendre polynomial weighted moments [0 to 7 correspond to (a) to (h)] for background-subtracted and efficiency-corrected $B^0 \to \bar{D}^0\pi^+\pi^-$ data and the Dalitz plot fit results as a function of $m^2(\pi^+\pi^-)$.

larger than $L/2$. The $\rho(770)$ resonance can clearly be seen in the distributions with $L \leq 2$ and the $D_2^*(2460)^-$ resonance in the distributions with $L \leq 4$. Figures 16 and 17 display an expanded version in low mass regions. The distributions from the isobar and the K-matrix models are compatible with those from data.

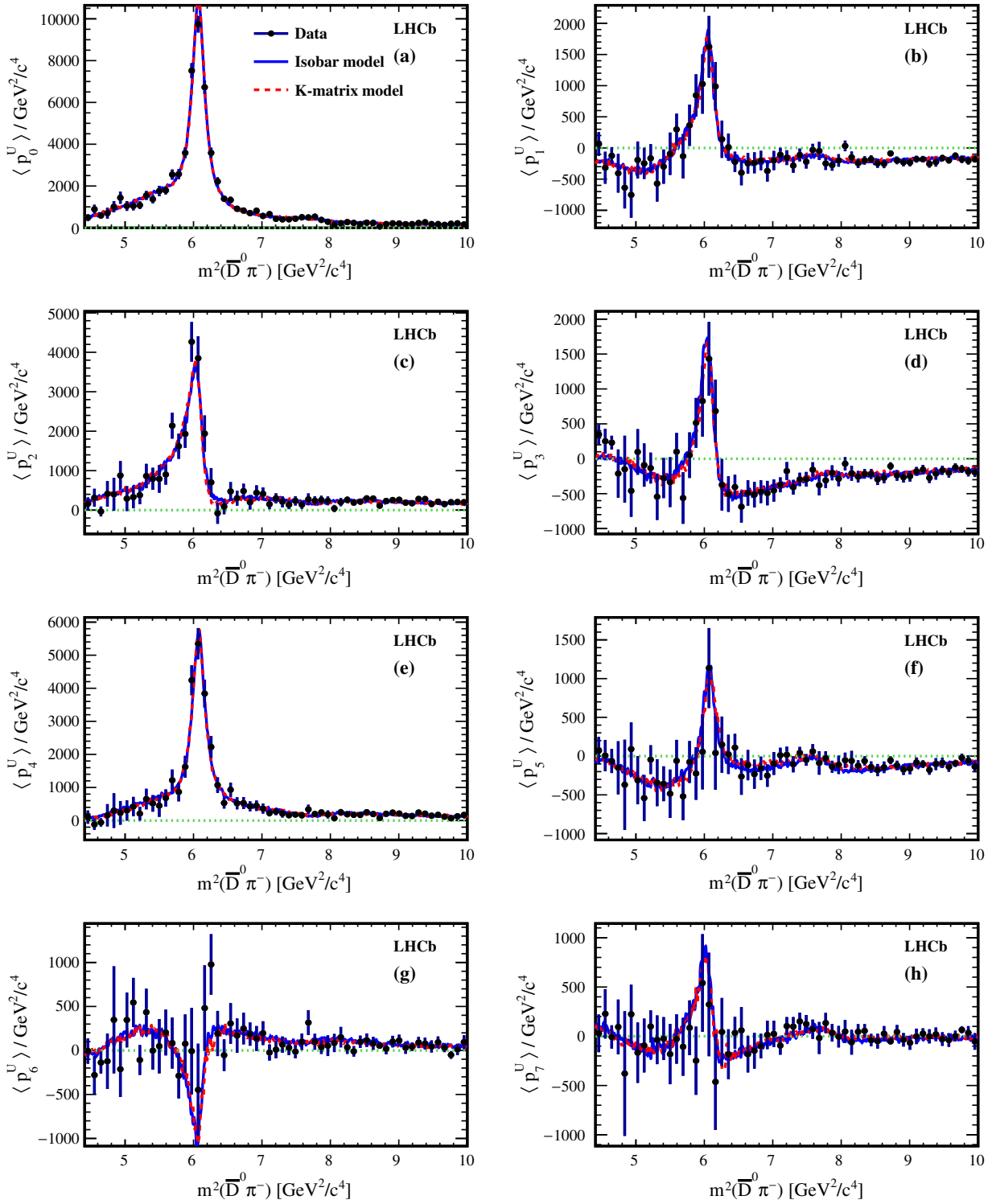

FIG. 16 (color online). The first eight unnormalized Legendre polynomial weighted moments [0 to 7 correspond to (a) to (h)] for background-subtracted and efficiency-corrected $B^0 \to \bar{D}^0\pi^+\pi^-$ data and the Dalitz plot fit results as a function of $m^2(\bar{D}^0\pi^-)$. Only results in the region $m^2(\bar{D}^0\pi^-) < 10$ GeV$^2/c^4$ are shown.

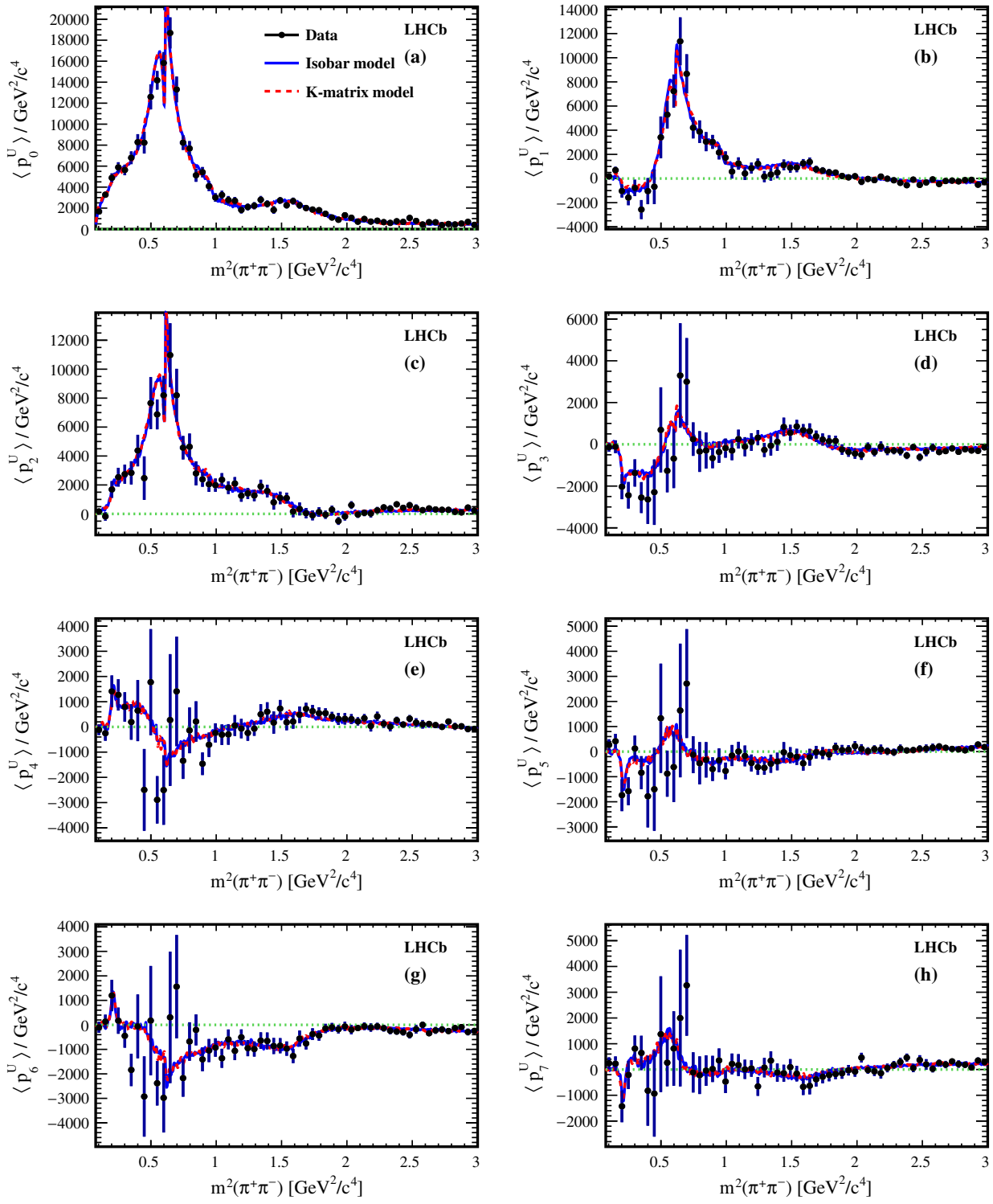

FIG. 17 (color online). The first eight unnormalized Legendre polynomial weighted moments [0 to 7 correspond to (a) to (h)] for background-subtracted and efficiency-corrected $B^0 \to \bar{D}^0\pi^+\pi^-$ data and the Dalitz plot fit results as a function of $m^2(\pi^+\pi^-)$. Only results in the region $m^2(\pi^+\pi^-) < 3$ GeV$^2/c^4$ are shown.

APPENDIX B: SYSTEMATIC UNCERTAINTIES ON THE PARAMETERS IN THE DALITZ PLOT ANALYSIS

1. Systematic uncertainties for the isobar model

TABLE XIV. Systematic uncertainties on the $\bar{D}^0\pi^-$ resonant masses (MeV/c^2) and widths (MeV) for the isobar model.

	$D_0^*(2400)^-$		$D_2^*(2460)^-$		$D_3^*(2760)^-$	
Source	Γ_0	m_0	Γ_0	m_0	Γ_0	m_0
PID	1.9	0.5	<0.1	<0.1	1.2	0.3
Trigger	0.5	0.2	0.2	<0.1	1.9	0.7
Reconstruction	0.2	0.1	<0.1	<0.1	0.5	0.1
Simulation statistic	0.6	0.1	0.1	<0.1	0.6	0.1
Background model	1.5	0.6	0.1	<0.1	3.4	0.4
$D^*(2010)^-$ veto	4.4	0.8	<0.1	<0.1	4.6	0.4
Total (experiment)	5.1	1.1	0.3	<0.1	6.2	1.0
Additional resonances	10.7	0.4	0.1	0.1	21.0	5.1
RBW parameters	0.1	1.9	0.1	<0.1	1.0	1.5
$\pi\pi$ resonant mass, width	3.4	0.1	0.1	0.1	2.9	1.3
B^0, D^0 mass	0.2	0.2	0.2	0.2	0.2	0.2
$f_0(500)$ model	2.3	3.6	0.5	<0.1	9.0	3.5
$f_0(980)$ model	2.8	0.7	0.2	0.1	3.5	1.2
Total (model)	11.8	4.2	0.6	0.3	23.3	6.6
Total (all)	12.9	4.3	0.7	0.3	24.1	6.7

TABLE XV. Systematic uncertainties on the moduli of the complex coefficients of the resonant contributions for the isobar model. The moduli are normalized to that of $\rho(770)$.

Source	Nonresonance	$f_0(500)$	$\omega(782)$	$f_0(980)$	$f_2(1270)$	$\rho(1450)$
PID	0.02	0.15	<0.01	0.03	<0.001	0.01
Trigger	0.02	0.03	<0.01	0.01	<0.001	<0.01
Reconstruction	<0.01	0.01	<0.01	<0.01	<0.001	<0.01
Simulation statistic	<0.01	0.11	<0.01	0.01	<0.001	<0.01
Background model	<0.01	0.07	<0.01	0.02	<0.001	<0.01
$D^*(2010)^-$ veto	0.03	0.20	<0.01	0.08	0.002	0.01
Total (experiment)	0.04	0.29	<0.01	0.09	<0.001	0.01
Additional resonances	0.34	0.61	<0.01	0.03	0.003	<0.01
RBW parameters	0.11	0.10	0.01	0.04	0.001	0.01
$\pi\pi$ resonant mass, width	0.06	0.41	<0.01	0.03	0.001	<0.01
$f_0(500)$ model	0.36	n/a	<0.01	0.46	0.004	0.01
$f_0(980)$ model	0.01	0.30	<0.01	n/a	<0.001	0.01
Total (model)	0.51	0.80	0.01	0.46	0.005	0.02
Total	0.51	0.85	0.01	0.47	0.006	0.02

Source	$\rho(1700)$	$f_0(2020)$	$\bar{D}^0\pi^-$ P-wave	$D_0^*(2400)^-$	$D_2^*(2460)^-$	$D_3^*(2760)^-$
PID	<0.001	0.06	0.14	0.21	<0.01	<0.001
Trigger	0.001	0.02	0.17	0.08	0.02	<0.001
Reconstruction	<0.001	<0.01	0.01	0.02	<0.01	<0.001
Simulation statistic	0.001	0.02	0.10	0.03	0.01	<0.001
Background model	0.002	0.01	0.03	0.06	<0.01	0.002
$D^*(2010)^-$ veto	0.006	0.20	n/a	0.20	<0.01	0.002
Total (experiment)	0.006	0.21	0.25	0.31	0.02	0.003
Additional resonances	0.005	0.37	1.74	0.47	0.01	0.007
RBW parameters	0.002	0.27	0.05	0.12	0.01	<0.001
$\pi\pi$ resonant mass, width	0.002	0.73	0.16	0.19	<0.01	0.001
$f_0(500)$ model	0.004	1.56	0.62	0.20	0.01	0.003
$f_0(980)$ model	0.003	0.06	0.06	0.18	0.01	0.002
Total (model)	0.008	1.78	1.86	0.59	0.02	0.008
Total (all)	0.010	1.80	1.87	0.66	0.03	0.008

TABLE XVI. Systematic uncertainties on the phases (°) of the complex coefficients of the resonant contributions for the isobar model. The phase of $\rho(700)$ is set to 0° as the reference.

Source	Nonresonance	$f_0(500)$	$\omega(782)$	$f_0(980)$	$f_2(1270)$	$\rho(1450)$
PID	0.2	0.1	0.4	0.1	0.1	0.1
Trigger	1.1	0.3	0.1	0.1	0.6	0.2
Reconstruction	<0.1	<0.1	<0.1	<0.1	0.1	0.1
Simulation statistic	0.3	0.1	0.3	0.2	0.3	0.3
Background model	0.7	0.1	<0.1	0.4	0.4	0.4
$D^*(2010)^-$ veto	1.8	1.2	0.2	1.4	1.4	4.8
Total (experiment)	2.3	1.3	0.6	1.5	1.6	4.8
Additional resonances	3.0	2.8	<0.1	2.7	1.6	1.1
RBW parameters	0.3	1.1	0.1	1.3	<0.1	0.3
$\pi\pi$ resonant mass, width	2.3	0.1	0.3	0.4	1.2	2.2
$f_0(500)$ model	3.7	n/a	0.3	10.5	3.0	3.6
$f_0(980)$ model	1.0	2.1	0.2	n/a	1.1	1.1
Total (model)	5.4	3.7	0.5	10.9	3.8	4.5
Total (all)	5.8	3.9	0.7	11.0	4.1	6.6

Source	$\rho(1700)$	$f_0(2020)$	$\bar{D}^0\pi^-$ P-wave	$D_0^*(2400)^-$	$D_2^*(2460)^-$	$D_3^*(2760)^-$
PID	0.4	<0.1	0.2	0.3	0.1	0.2
Trigger	0.5	0.2	0.2	0.7	<0.1	0.6
Reconstruction	<0.1	0.1	0.1	0.1	0.1	0.1
Simulation statistic	0.7	0.2	0.1	0.2	0.1	0.1
Background model	0.6	0.9	0.1	<0.1	0.2	0.3
$D^*(2010)^-$ veto	4.4	0.6	n/a	2.7	0.8	1.2
Total (experiment)	4.5	1.1	0.3	2.8	0.8	1.4
Additional resonances	0.3	3.4	5.7	1.8	1.2	3.9
RBW parameters	1.0	1.1	0.6	1.6	0.7	1.8
$\pi\pi$ resonant mass, width	0.5	1.3	0.5	0.3	0.7	2.0
$f_0(500)$ model	0.3	26.5	4.2	3.9	2.4	1.9
$f_0(980)$ model	2.1	1.8	0.4	0.1	0.9	0.2
Total (model)	2.4	26.8	7.1	4.6	3.0	5.1
Total (all)	5.1	26.9	7.1	5.4	3.1	5.3

TABLE XVII. Systematic uncertainties on the fit fractions (%) of the resonant contributions for the isobar model.

Source	Nonresonance	$f_0(500)$	$\rho(770)$	$\omega(782)$	$f_0(980)$	$f_2(1270)$	$\rho(1450)$
PID	0.02	0.23	0.37	0.01	0.04	0.07	0.06
Trigger	0.01	0.03	0.09	<0.01	<0.01	0.05	0.03
Reconstruction	0.01	0.09	0.39	0.01	0.01	0.01	<0.01
Simulation statistic	<0.01	0.09	0.26	<0.01	0.01	0.04	<0.01
Background model	0.01	0.08	0.07	<0.01	0.01	0.05	0.04
$D^*(2010)^-$ veto	0.06	0.15	0.01	<0.01	0.10	0.29	0.03
Total (experiment)	0.07	0.31	0.61	0.01	0.11	0.31	0.08
Additional resonances	0.51	0.57	0.81	0.02	<0.01	0.53	0.01
RBW parameters	0.21	0.03	0.50	0.01	0.07	0.10	0.15
$\pi\pi$ resonant mass, width	0.09	0.60	0.08	<0.01	0.03	0.16	<0.01
$f_0(500)$ model	0.57	2.25	0.04	0.01	0.50	0.94	0.14
$f_0(980)$ model	0.03	0.48	0.19	0.01	0.20	0.11	0.09
Total (model)	0.80	2.45	0.98	0.03	0.54	1.10	0.22
Total (all)	0.80	2.47	1.15	0.03	0.56	1.14	0.24

Source	$\rho(1700)$	$f_0(2020)$	S-wave	$\bar{D}^0\pi^-$ P-wave	$D_0^*(2400)^-$	$D_2^*(2460)^-$	$D_3^*(2760)^-$
PID	0.01	0.01	0.31	0.19	0.12	0.43	0.02
Trigger	<0.01	0.03	0.04	0.02	0.06	0.28	0.01
Reconstruction	<0.01	0.01	0.12	0.13	0.14	0.18	0.02
Simulation statistic	<0.01	0.01	0.05	0.06	0.04	0.09	0.01
Background model	0.02	0.01	0.04	0.05	0.03	0.01	0.02
$D^*(2010)^-$ veto	0.07	0.14	0.26	n/a	0.01	0.50	0.06
Total (experiment)	0.07	0.15	0.43	0.24	0.20	0.74	0.07
Additional resonances	0.04	0.24	1.43	1.60	0.01	0.01	0.07
RBW parameters	0.02	0.21	0.07	0.17	0.28	0.44	0.02
$\pi\pi$ resonant mass, width	0.02	0.22	0.05	0.17	0.13	0.02	0.02
$f_0(500)$ model	0.03	0.92	0.25	0.60	0.13	0.22	0.03
$f_0(980)$ model	0.02	0.04	0.14	0.01	0.10	0.09	0.03
Total (model)	0.06	1.00	1.46	1.73	0.35	0.50	0.09
Total (all)	0.10	1.01	1.52	1.74	0.40	0.90	0.11

2. Systematic uncertainties for the K-matrix model

TABLE XVIII. Systematic uncertainties on the $\bar{D}^0\pi^-$ resonant masses (MeV/c^2) and widths (MeV) for the K-matrix model.

	$D_0^*(2400)^-$		$D_2^*(2460)^-$		$D_3^*(2760)^-$	
Source	Γ_0	m_0	Γ_0	m_0	Γ_0	m_0
PID	8.9	5.9	1.0	0.3	1.1	8.6
Trigger	1.1	0.6	0.1	<0.1	0.1	0.1
Reconstruction	<0.1	<0.1	<0.1	<0.1	<0.1	<0.1
Simulation statistic	4.6	0.5	0.2	0.1	2.4	0.4
Background model	2.3	0.9	0.1	<0.1	2.7	0.8
$D^*(2010)^-$ veto	14.9	9.0	1.4	0.3	12.1	5.4
Total (experiment)	18.1	10.8	1.7	0.4	12.7	10.2
Additional resonances	8.5	1.0	0.3	0.2	1.4	1.1
RBW parameters	6.0	1.5	<0.1	0.1	8.9	2.3
$\pi\pi$ resonant mass, width	1.4	0.9	0.1	0.1	1.3	0.1
B^0, D^0 mass	0.2	0.2	0.2	0.2	0.2	0.2
Total (model)	10.5	2.0	0.4	0.3	9.1	2.6
Total (all)	21.0	11.0	1.8	0.5	15.6	10.5

TABLE XIX. Systematic uncertainties on the moduli of the complex coefficients of the resonant contributions for the K-matrix model. The moduli are normalized to that of $\rho(770)$.

Source	$\omega(782)$	$f_2(1270)$	$\rho(1450)$	$\rho(1700)$
PID	<0.01	0.001	0.04	0.037
Trigger	<0.01	<0.001	<0.01	0.002
Reconstruction	<0.01	<0.001	<0.01	<0.001
Simulation statistic	<0.01	0.003	0.02	0.004
Background model	<0.01	<0.001	<0.01	0.001
$D^*(2010)^-$ veto	0.01	0.005	0.07	0.067
Total (experiment)	0.01	0.006	0.08	0.077
Additional resonances	<0.01	0.003	<0.01	0.003
RBW parameters	0.01	<0.001	0.01	0.003
$\pi\pi$ resonant mass, width	<0.01	<0.001	<0.01	0.010
Total (model)	0.01	0.003	0.01	0.011
Total (all)	0.01	0.007	0.08	0.077
Source	$\bar{D}^0\pi^-$ P-wave	$D_0^*(2400)^-$	$D_2^*(2460)^-$	$D_3^*(2760)^-$
PID	0.21	0.10	<0.01	0.003
Trigger	0.12	0.01	0.02	<0.001
Reconstruction	<0.01	<0.01	<0.01	0.001
Simulation statistic	0.62	0.72	0.03	0.003
Background model	0.13	0.13	<0.01	0.002
$D^*(2010)^-$ veto	<0.01	0.39	<0.01	0.001
Total (experiment)	0.68	0.84	0.04	0.005
Additional resonances	0.52	0.22	<0.01	0.002
RBW parameters	0.30	0.46	<0.01	0.002
$\pi\pi$ resonant mass, width	0.05	0.04	<0.01	0.001
Total (model)	0.60	0.51	<0.01	0.003
Total (all)	0.91	0.98	0.04	0.006

TABLE XX. Systematic uncertainties on the phases (°) of the complex coefficients of the resonant contributions for the K-matrix model. The phase of $\rho(700)$ is set to 0° as reference.

Source	$\omega(782)$	$f_2(1270)$	$\rho(1450)$	$\rho(1700)$
PID	0.8	5.6	4.1	12.8
Trigger	<0.1	0.2	<0.1	0.3
Reconstruction	0.1	<0.1	<0.1	0.0
Simulation statistic	0.5	1.1	1.6	1.5
Background model	0.2	1.3	0.3	0.1
$D^*(2010)^-$ veto	1.1	6.2	7.1	19.2
Total (experiment)	1.5	8.5	8.4	23.1
Additional resonances	0.2	1.9	2.3	3.3
RBW parameters	0.4	1.3	0.4	0.6
$\pi\pi$ resonant mass, width	0.1	1.1	5.0	3.0
Total (model)	0.5	2.6	5.5	4.5
Total (all)	1.5	8.9	10.0	23.6
Source	$\bar{D}^0\pi^-$ P-wave	$D_0^*(2400)^-$	$D_2^*(2460)^-$	$D_3^*(2760)^-$
PID	3.2	7.0	0.2	11.8
Trigger	0.4	0.9	0.3	0.1
Reconstruction	<0.1	<0.1	<0.1	0.1
Simulation statistic	0.1	0.8	0.1	1.3
Background model	0.7	0.3	0.4	0.1
$D^*(2010)^-$ veto	n/a	9.1	0.4	9.5
Total (experiment)	3.3	11.5	0.7	15.2
Additional resonances	6.6	0.2	1.8	0.4
RBW parameters	1.0	1.5	0.4	2.2
$\pi\pi$ resonant mass, width	0.4	0.7	0.2	0.3
Total (model)	6.7	1.7	1.9	2.3
Total (all)	7.5	11.7	2.0	15.4

TABLE XXI. Systematic uncertainties on the fit fractions (%) of the resonant contributions for the K-matrix model.

Source	$\rho(770)$	$\omega(782)$	$f_2(1270)$	$\rho(1450)$	$\rho(1700)$
PID	1.36	<0.01	0.06	0.50	0.37
Trigger	0.33	0.01	0.04	0.01	0.01
Reconstruction	0.02	<0.01	<0.01	<0.01	<0.01
Simulation statistic	1.17	0.01	0.45	0.22	0.02
Background model	0.07	<0.01	0.15	0.04	0.01
$D^*(2010)^-$ veto	1.09	<0.01	0.68	0.61	0.48
Total (experiment)	2.13	0.01	0.83	0.82	0.61
Additional resonances	0.61	0.02	0.56	0.01	0.05
RBW parameters	0.49	0.01	0.15	0.21	0.04
$\pi\pi$ resonant mass, width	0.12	0.01	0.04	0.04	0.10
Total (model)	0.79	0.02	0.58	0.21	0.12
Total (all)	2.28	0.03	1.02	0.85	0.62
Source	S-wave	$\bar{D}^0\pi^-$ P-wave	$D_0^*(2400)^-$	$D_2^*(2460)^-$	$D_3^*(2760)^-$
PID	0.77	0.59	0.13	0.28	0.13
Trigger	0.09	0.03	0.01	0.39	0.03
Reconstruction	0.01	<0.01	<0.01	<0.01	<0.01
Simulation statistic	0.31	0.28	0.49	0.38	0.01
Background model	0.23	0.13	0.08	0.03	0.04
$D^*(2010)^-$ veto	1.44	n/a	0.69	0.86	0.12
Total (experiment)	1.68	0.67	0.86	1.06	0.18
Additional resonances	1.08	0.63	0.23	0.28	0.03
RBW parameters	0.18	0.40	0.47	0.46	0.06
$\pi\pi$ resonant mass, width	0.07	0.07	0.02	0.01	0.01
Total (model)	1.10	0.75	0.52	0.54	0.07
Total (all)	2.01	1.00	1.01	1.19	0.20

APPENDIX C: RESULTS FOR THE INTERFERENCE FIT FRACTIONS

The central values of the interference fit fractions for the isobar (K-matrix) model are given in Table XXII (Table XXIII). The statistical, experimental systematic and model-dependent uncertainties on these quantities are given in Tables XXIV, XXV and XXVI (Tables XXVII, XXVIII and XXIX).

TABLE XXII. Interference fit fractions (%) of the resonant contributions for the isobar model with $m(\bar{D}^0\pi^\pm) > 2.1$ GeV/c^2. The resonances are (A_0) nonresonant S-wave, (A_1) $f_0(500)$, (A_2) $f_0(980)$, (A_3) $f_0(2020)$, (A_4) $\rho(770)$, (A_5) $\omega(782)$, (A_6) $\rho(1450)$, (A_7) $\rho(1700)$, (A_8) $f_2(1270)$, (A_9) $\bar{D}^0\pi^-$ P-wave, (A_{10}) $D_0^*(2400)^-$, (A_{11}) $D_2^*(2460)^-$, (A_{12}) $D_3^*(2760)^-$. The diagonal elements correspond to the fit fractions given in Table IX.

	A_0	A_1	A_2	A_3	A_4	A_5	A_6	A_7	A_8	A_9	A_{10}	A_{11}	A_{12}
A_0	2.82	2.70	−0.37	−0.25	0.00	0.00	0.00	0.00	0.13	0.79	−1.70	−2.12	0.06
A_1	—	13.23	−1.02	−4.53	0.00	0.00	0.00	0.00	0.14	3.37	0.97	3.81	0.57
A_2	—	—	1.56	0.79	0.00	0.00	0.00	0.00	−0.21	−0.60	0.63	−0.90	−0.14
A_3	—	—	—	1.58	0.00	0.00	0.00	0.00	−0.17	−1.39	−1.27	−1.76	−0.16
A_4	—	—	—	—	37.54	−0.78	2.43	1.53	0.00	−5.71	−1.54	−3.26	−0.78
A_5	—	—	—	—	—	0.49	−0.01	0.00	0.00	0.00	0.01	−0.01	0.00
A_6	—	—	—	—	—	—	1.54	−0.06	0.00	0.26	−0.74	0.94	0.04
A_7	—	—	—	—	—	—	—	0.38	0.00	−0.89	−0.66	−0.58	−0.13
A_8	—	—	—	—	—	—	—	—	10.28	−2.29	−0.89	−1.43	−0.27
A_9	—	—	—	—	—	—	—	—	—	9.21	0.00	−0.01	0.00
A_{10}	—	—	—	—	—	—	—	—	—	—	9.00	0.01	0.00
A_{11}	—	—	—	—	—	—	—	—	—	—	—	28.83	0.00
A_{12}	—	—	—	—	—	—	—	—	—	—	—	—	1.22

TABLE XXIII. Interference fit fractions (%) of the resonant contributions for the K-matrix model with $m(\bar{D}^0\pi^\pm) > 2.1$ GeV/c^2. The resonances are (A_0) K-matrix S-wave, (A_1) $\rho(770)$, (A_2) $\omega(782)$, (A_3) $\rho(1450)$, (A_4) $\rho(1700)$, (A_5) $f_2(1270)$, (A_6) $\bar{D}^0\pi^-$ P-wave, (A_7) $D_0^*(2400)^-$, (A_8) $D_2^*(2460)^-$, (A_9) $D_3^*(2760)^-$. The diagonal elements correspond to the fit fractions given in Table IX.

	A_0	A_1	A_2	A_3	A_4	A_5	A_6	A_7	A_8	A_9
A_0	16.51	0.00	0.00	0.00	0.00	−0.06	2.37	−1.45	−0.10	0.01
A_1	—	36.15	−0.84	4.20	2.10	0.00	−5.39	−1.88	−2.81	−0.90
A_2	—	—	0.50	−0.01	0.00	0.00	0.00	0.01	−0.01	0.00
A_3	—	—	—	2.16	−0.43	0.00	−0.15	−1.14	0.73	−0.04
A_4	—	—	—	—	0.83	0.00	−1.49	−0.99	−1.12	−0.24
A_5	—	—	—	—	—	9.88	−2.03	−0.73	−1.50	−0.35
A_6	—	—	—	—	—	—	9.22	0.00	−0.01	0.00
A_7	—	—	—	—	—	—	—	9.27	0.01	0.00
A_8	—	—	—	—	—	—	—	—	28.13	0.00
A_9	—	—	—	—	—	—	—	—	—	1.58

TABLE XXIV. Statistical uncertainties on the interference fit fractions (%) of the resonant contributions for the isobar model with $m(\bar{D}^0\pi^\pm) > 2.1$ GeV/c^2. The resonances are (A_0) nonresonant S-wave, (A_1) $f_0(500)$, (A_2) $f_0(980)$, (A_3) $f_0(2020)$, (A_4) $\rho(770)$, (A_5) $\omega(782)$, (A_6) $\rho(1450)$, (A_7) $\rho(1700)$, (A_8) $f_2(1270)$, (A_9) $\bar{D}^0\pi^-$ P-wave, (A_{10}) $D_0^*(2400)^-$, (A_{11}) $D_2^*(2460)^-$, (A_{12}) $D_3^*(2760)^-$. The diagonal elements correspond to the statistical uncertainties on the fit fractions given in Table IX.

	A_0	A_1	A_2	A_3	A_4	A_5	A_6	A_7	A_8	A_9	A_{10}	A_{11}	A_{12}
A_0	0.34	0.29	0.11	0.07	0.00	0.00	0.00	0.00	0.02	0.13	0.36	0.26	0.03
A_1	—	0.89	0.54	0.64	0.00	0.00	0.00	0.00	0.04	0.22	0.45	0.20	0.08
A_2	—	—	0.29	0.15	0.00	0.00	0.00	0.00	0.03	0.09	0.09	0.11	0.04
A_3	—	—	—	0.36	0.00	0.00	0.00	0.00	0.02	0.18	0.20	0.22	0.05
A_4	—	—	—	—	1.00	0.33	0.65	0.32	0.00	0.35	0.21	0.22	0.12
A_5	—	—	—	—	—	0.13	0.00	0.00	0.00	0.00	0.00	0.00	0.00
A_6	—	—	—	—	—	—	0.32	0.24	0.00	0.24	0.18	0.19	0.04
A_7	—	—	—	—	—	—	—	$^{+0.25}_{-0.12}$	0.00	0.23	0.15	0.20	0.03
A_8	—	—	—	—	—	—	—	—	0.49	0.20	0.14	0.07	0.04
A_9	—	—	—	—	—	—	—	—	—	0.56	0.00	0.00	0.00
A_{10}	—	—	—	—	—	—	—	—	—	—	0.60	0.00	0.00
A_{11}	—	—	—	—	—	—	—	—	—	—	—	0.69	0.00
A_{12}	—	—	—	—	—	—	—	—	—	—	—	—	0.19

TABLE XXV. Experimental systematic uncertainties on the interference fit fractions (%) of the resonant contributions for the isobar model with $m(\bar{D}^0\pi^\pm) > 2.1$ GeV/c^2. The resonances are (A_0) nonresonant S-wave, (A_1) $f_0(500)$, (A_2) $f_0(980)$, (A_3) $f_0(2020)$, (A_4) $\rho(770)$, (A_5) $\omega(782)$, (A_6) $\rho(1450)$, (A_7) $\rho(1700)$, (A_8) $f_2(1270)$, (A_9) $\bar{D}^0\pi^-$ P-wave, (A_{10}) $D_0^*(2400)^-$, (A_{11}) $D_2^*(2460)^-$, (A_{12}) $D_3^*(2760)^-$. The diagonal elements correspond to the statistical uncertainties on the fit fractions given in Table IX.

	A_0	A_1	A_2	A_3	A_4	A_5	A_6	A_7	A_8	A_9	A_{10}	A_{11}	A_{12}
A_0	0.07	0.06	0.03	0.03	0.00	0.00	0.00	0.00	0.07	0.02	0.11	0.09	0.01
A_1	—	0.31	0.22	0.20	0.00	0.00	0.00	0.00	0.07	0.06	0.26	0.04	0.01
A_2	—	—	0.11	0.05	0.00	0.00	0.00	0.00	0.14	0.02	0.04	0.04	0.02
A_3	—	—	—	0.15	0.00	0.00	0.00	0.00	0.11	0.08	0.06	0.11	0.02
A_4	—	—	—	—	0.61	0.05	0.31	0.16	0.00	0.18	0.05	0.03	0.02
A_5	—	—	—	—	—	0.01	0.00	0.00	0.00	0.00	0.00	0.00	0.00
A_6	—	—	—	—	—	—	0.08	0.03	0.00	0.11	0.12	0.06	0.01
A_7	—	—	—	—	—	—	—	0.07	0.00	0.10	0.07	0.03	0.01
A_8	—	—	—	—	—	—	—	—	0.31	0.16	0.11	0.07	0.02
A_9	—	—	—	—	—	—	—	—	—	0.24	0.00	0.00	0.00
A_{10}	—	—	—	—	—	—	—	—	—	—	0.20	0.00	0.00
A_{11}	—	—	—	—	—	—	—	—	—	—	—	0.74	0.00
A_{12}	—	—	—	—	—	—	—	—	—	—	—	—	0.07

TABLE XXVI. Model-dependent systematic uncertainties on the interference fit fractions (%) of the resonant contributions for the isobar model with $m(\bar{D}^0\pi^\pm) > 2.1$ GeV/c^2. The resonances are (A_0) nonresonant S-wave, (A_1) $f_0(500)$, (A_2) $f_0(980)$, (A_3) $f_0(2020)$, (A_4) $\rho(770)$, (A_5) $\omega(782)$, (A_6) $\rho(1450)$, (A_7) $\rho(1700)$, (A_8) $f_2(1270)$, (A_9) $\bar{D}^0\pi^-$ P-wave, (A_{10}) $D_0^*(2400)^-$, (A_{11}) $D_2^*(2460)^-$, (A_{12}) $D_3^*(2760)^-$. The diagonal elements correspond to the statistical uncertainties on the fit fractions given in Table IX.

	A_0	A_1	A_2	A_3	A_4	A_5	A_6	A_7	A_8	A_9	A_{10}	A_{11}	A_{12}
A_0	0.80	0.61	0.31	0.17	0.00	0.00	0.00	0.00	0.03	0.28	0.56	0.45	0.01
A_1	—	2.45	2.00	3.03	0.00	0.00	0.00	0.00	0.16	0.72	0.79	0.98	0.08
A_2	—	—	0.54	0.67	0.00	0.00	0.00	0.00	0.02	0.15	0.13	0.28	0.08
A_3	—	—	—	1.00	0.00	0.00	0.00	0.00	0.08	0.51	0.34	0.69	0.06
A_4	—	—	—	—	0.98	0.03	0.47	0.12	0.00	0.54	0.33	0.27	0.09
A_5	—	—	—	—	—	0.03	0.00	0.00	0.00	0.00	0.00	0.00	0.00
A_6	—	—	—	—	—	—	0.22	0.08	0.00	0.31	0.18	0.14	0.03
A_7	—	—	—	—	—	—	—	0.06	0.00	0.12	0.07	0.04	0.02
A_8	—	—	—	—	—	—	—	—	1.10	0.49	0.33	0.09	0.05
A_9	—	—	—	—	—	—	—	—	—	1.73	0.00	0.00	0.00
A_{10}	—	—	—	—	—	—	—	—	—	—	0.35	0.00	0.00
A_{11}	—	—	—	—	—	—	—	—	—	—	—	0.50	0.00
A_{12}	—	—	—	—	—	—	—	—	—	—	—	—	0.09

TABLE XXVII. Statistical uncertainties on the interference fit fractions (%) of the resonant contributions for the K-matrix model with $m(\bar{D}^0\pi^\pm) > 2.1$ GeV/c^2. The resonances are (A_0) K-matrix S-wave, (A_1) $\rho(770)$, (A_2) $\omega(782)$, (A_3) $\rho(1450)$, (A_4) $\rho(1700)$, (A_5) $f_2(1270)$, (A_6) $\bar{D}^0\pi^-$ P-wave, (A_7) $D_0^*(2400)^-$, (A_8) $D_2^*(2460)^-$, (A_9) $D_3^*(2760)^-$. The diagonal elements correspond to the statistical uncertainties on the fit fractions shown in Table IX.

	A_0	A_1	A_2	A_3	A_4	A_5	A_6	A_7	A_8	A_9
A_0	0.70	0.00	0.00	0.00	0.00	0.04	0.28	0.49	0.43	0.16
A_1	—	1.00	0.34	0.71	0.31	0.00	0.41	0.22	0.25	0.14
A_2	—	—	0.13	0.00	0.00	0.00	0.01	0.00	0.00	0.00
A_3	—	—	—	0.42	0.29	0.00	0.29	0.23	0.20	0.07
A_4	—	—	—	—	0.21	0.00	0.23	0.16	0.19	0.04
A_5	—	—	—	—	—	0.58	0.22	0.16	0.08	0.05
A_6	—	—	—	—	—	—	0.58	0.00	0.00	0.00
A_7	—	—	—	—	—	—	—	0.60	0.00	0.00
A_8	—	—	—	—	—	—	—	—	0.72	0.00
A_9	—	—	—	—	—	—	—	—	—	0.22

TABLE XXVIII. Experimental systematic uncertainties on the interference fit fractions (%) of the resonant contributions for the K-matrix model with $m(\bar{D}^0\pi^\pm) > 2.1$ GeV/c^2. The resonances are (A_0) K-matrix S-wave, (A_1) $\rho(770)$, (A_2) $\omega(782)$, (A_3) $\rho(1450)$, (A_4) $\rho(1700)$, (A_5) $f_2(1270)$, (A_6) $\bar{D}^0\pi^-$ P-wave, (A_7) $D_0^*(2400)^-$, (A_8) $D_2^*(2460)^-$, (A_9) $D_3^*(2760)^-$. The diagonal elements correspond to the statistical uncertainties on the fit fractions shown in Table IX.

	A_0	A_1	A_2	A_3	A_4	A_5	A_6	A_7	A_8	A_9
A_0	1.68	0.00	0.00	0.00	0.00	0.10	0.84	1.88	1.21	0.36
A_1	—	2.13	0.06	1.42	1.02	0.00	0.87	0.37	0.14	0.29
A_2	—	—	0.01	0.00	0.00	0.00	0.01	0.00	0.00	0.00
A_3	—	—	—	0.82	0.73	0.00	0.13	0.30	0.10	0.15
A_4	—	—	—	—	0.61	0.00	0.88	0.51	0.89	0.14
A_5	—	—	—	—	—	0.83	0.27	0.16	0.18	0.16
A_6	—	—	—	—	—	—	0.67	0.00	0.00	0.00
A_7	—	—	—	—	—	—	—	0.86	0.00	0.00
A_8	—	—	—	—	—	—	—	—	1.06	0.00
A_9	—	—	—	—	—	—	—	—	—	0.18

TABLE XXIX. Model-dependent systematic uncertainties on the interference fit fractions (%) of the resonant contributions for the K-matrix model with $m(\bar{D}^0\pi^\pm) > 2.1$ GeV/c^2. The resonances are (A_0) K-matrix S-wave, (A_1) $\rho(770)$, (A_2) $\omega(782)$, (A_3) $\rho(1450)$, (A_4) $\rho(1700)$, (A_5) $f_2(1270)$, (A_6) $\bar{D}^0\pi^-$ P-wave, (A_7) $D_0^*(2400)^-$, (A_8) $D_2^*(2460)^-$, (A_9) $D_3^*(2760)^-$. The diagonal elements correspond to the statistical uncertainties on the fit fractions shown in Table IX.

	A_0	A_1	A_2	A_3	A_4	A_5	A_6	A_7	A_8	A_9
A_0	1.10	0.00	0.00	0.00	0.00	0.02	0.24	0.25	0.40	0.15
A_1	—	0.79	0.02	0.41	0.25	0.00	0.26	0.29	0.19	0.05
A_2	—	—	0.02	0.00	0.00	0.00	0.00	0.00	0.00	0.00
A_3	—	—	—	0.21	0.08	0.00	0.20	0.09	0.12	0.03
A_4	—	—	—	—	0.12	0.00	0.14	0.12	0.08	0.02
A_5	—	—	—	—	—	0.58	0.14	0.19	0.08	0.08
A_6	—	—	—	—	—	—	0.75	0.00	0.00	0.00
A_7	—	—	—	—	—	—	—	0.52	0.00	0.00
A_8	—	—	—	—	—	—	—	—	0.54	0.00
A_9	—	—	—	—	—	—	—	—	—	0.07

APPENDIX D: RESULTS OF THE K-MATRIX PARAMETERS

The moduli and phases of the K-matrix parameters in Eq. (25) are listed in Table XXX. The breakdown of systematic uncertainties is shown in Tables XXXI and XXXII.

TABLE XXX. The moduli and phases of the K-matrix parameters. The first uncertainty is statistical, the second the experimental systematic, and the third the model-dependent systematic. The moduli are normalized to that of the $\rho(770)$ contribution and the phase of $\rho(770)$ is set to 0°.

Parameter	Modulus	Phase (°)
f_{10}	$17.0 \pm 3.3 \pm 9.5 \pm 3.7$	$347.3 \pm 13.7 \pm 18.7 \pm 3.2$
f_{11}	$14.9 \pm 17.1 \pm 20.3 \pm 8.0$	$160.0 \pm 70.1 \pm 39.6 \pm 26.2$
f_{12}	$111.3 \pm 23.1 \pm 23.8 \pm 12.8$	$226.1 \pm 12.0 \pm 11.2 \pm 4.9$
f_{13}	$28.7 \pm 14.2 \pm 8.1 \pm 5.3$	$186.5 \pm 30.0 \pm 30.4 \pm 8.6$
f_{14}	$31.0 \pm 12.8 \pm 13.4 \pm 8.8$	$10.61 \pm 25.9 \pm 15.2 \pm 2.9$
β_0	$9.5 \pm 1.8 \pm 2.9 \pm 1.1$	$20.7 \pm 15.2 \pm 13.5 \pm 10.4$
β_1	$17.2 \pm 6.4 \pm 6.2 \pm 4.8$	$19.6 \pm 19.4 \pm 14.4 \pm 3.7$
β_2	$34.9 \pm 7.6 \pm 14.3 \pm 3.1$	$128.3 \pm 12.1 \pm 2.1 \pm 1.9$
β_3	$53.5 \pm 14.3 \pm 9.2 \pm 4.2$	$138.7 \pm 15.5 \pm 7.2 \pm 3.9$
β_4	$52.5 \pm 10.2 \pm 22.4 \pm 5.9$	$305.0 \pm 10.5 \pm 13.5 \pm 2.2$

TABLE XXXI. Systematic uncertainties on the moduli of the K-matrix parameters. The moduli are normalized to that of $\rho(770)$.

Source	f_{10}	f_{11}	f_{12}	f_{13}	f_{14}	β_0	β_1	β_2	β_3	β_4
PID	8.1	5.5	22.5	3.2	13.2	2.5	3.6	10.7	8.0	18.0
Trigger	0.4	1.1	2.5	1.0	1.2	0.2	0.7	0.6	1.1	1.0
Reconstruction	0.1	0.9	0.4	0.5	0.7	0.1	0.4	0.4	0.6	0.5
Simulation statistic	0.3	4.6	2.8	2.7	1.6	0.1	1.8	1.0	0.6	0.7
Background model	0.6	0.5	6.5	<0.1	0.2	0.1	0.7	1.7	2.4	2.7
$D^*(2010)^-$ veto	4.9	18.9	1.9	6.8	0.6	1.4	4.6	9.2	3.7	13.1
Total (experiment)	9.5	20.3	23.8	8.1	13.4	2.9	6.2	14.3	9.2	22.4
Additional resonances	3.5	8.0	12.6	3.8	7.7	1.1	4.6	3.0	3.5	5.6
RBW parameters	1.2	0.4	2.3	3.3	4.0	0.2	1.1	0.5	2.2	1.9
$\pi\pi$ resonant mass, width	0.3	0.7	0.1	1.5	1.7	0.2	0.6	0.4	0.7	0.3
Total (model)	3.7	8.0	12.8	5.3	8.8	1.1	4.8	3.1	4.2	5.9
Total (all)	10.2	21.8	27.0	9.6	16.0	3.1	7.8	14.6	10.1	23.2

TABLE XXXII. Systematic uncertainties on the phases (°) of the K-matrix parameters. The phase of $\rho(700)$ is set to 0° as the reference.

Source	f_{10}	f_{11}	f_{12}	f_{13}	f_{14}	β_0	β_1	β_2	β_3	β_4
PID	18.0	35.0	9.6	25.9	5.8	10.4	10.4	1.7	1.4	4.3
Trigger	0.5	0.2	0.3	0.2	<0.1	0.5	0.3	0.1	0.5	0.1
Reconstruction	0.3	2.4	0.6	0.5	0.6	0.6	0.4	0.1	0.6	0.2
Simulation statistic	4.0	1.0	0.2	2.0	7.1	5.2	4.6	0.8	1.9	1.3
Background model	3.1	8.2	0.4	3.9	0.4	1.9	2.5	0.1	0.3	0.4
$D^*(2010)^-$ veto	0.3	16.4	5.8	15.2	12.1	6.5	8.5	1.0	6.7	12.7
Total (experiment)	18.7	39.6	11.2	30.4	15.2	13.5	14.4	2.1	7.2	13.5
Additional resonances	0.4	5.0	4.1	2.1	1.0	3.6	1.9	0.2	3.7	1.9
RBW parameters	3.2	25.2	2.6	8.3	0.6	9.2	3.2	1.9	1.0	1.1
$\pi\pi$ resonant mass, width	0.3	5.0	0.5	1.0	2.6	3.2	0.4	0.2	0.7	0.3
Total (model)	3.2	26.2	4.9	8.6	2.9	10.4	3.7	1.9	3.9	2.2
Total (all)	19.0	47.5	12.3	31.6	15.5	17.0	14.9	2.9	8.1	13.7

[1] N. Cabibbo, Unitary Symmetry and Leptonic Decays, Phys. Rev. Lett. **10**, 531 (1963).

[2] M. Kobayashi and T. Maskawa, *CP*-violation in the renormalizable theory of weak interaction, Prog. Theor. Phys. **49**, 652 (1973).

[3] B. Aubert *et al.* (*BABAR* Collaboration), Measurement of time-dependent *CP* asymmetry in $B^0 \to c\bar{c}K^{(*)0}$ decays, Phys. Rev. D **79**, 072009 (2009).

[4] I. Adachi *et al.* (Belle Collaboration), Precise Measurement of the *CP* Violation Parameter $\sin 2\phi_1$ in $B^0 \to c\bar{c}K^0$ Decays, Phys. Rev. Lett. **108**, 171802 (2012).

[5] R. Aaij *et al.* (LHCb Collaboration), Measurement of *CP* Violation in $B^0 \to J/\psi K^0_S$ Decays, arXiv:1503.07089 [Phys. Rev. Lett. (to be published)].

[6] J. Charles, A. Le Yaouanc, L. Oliver, O. Pène, and J.-C. Raynal, $B^0_d(t) \to DPP$ time-dependent Dalitz plots, *CP*-violating angles 2β, $2\beta + \gamma$, and discrete ambiguities, Phys. Lett. B **425**, 375 (1998).

[7] T. Latham and T. Gershon, A method of measuring $cos(2\beta)$ using time-dependent Dalitz plot analysis of $B^0 \to D_{CP}\pi^+\pi^-$, J. Phys. G **36**, 025006 (2009).

[8] B. Aubert *et al.* (*BABAR* Collaboration), Measurement of Time-Dependent *CP* Asymmetry in $B^0 \to D^{(*)}_{CP}h^0$ Decays, Phys. Rev. Lett. **99**, 081801 (2007).

[9] B. Aubert *et al.* (*BABAR* Collaboration), Measurement of $cos2\beta$ in $B^0 \to D^{(*)0}h^0$ Decays with a Time-Dependent Dalitz Plot Analysis of $D \to K^0_S\pi^+\pi^-$, Phys. Rev. Lett. **99**, 231802 (2007).

[10] P. Krokovny *et al.* (Belle Collaboration), Measurement of the Quark Mixing Parameter $cos(2\phi_1)$ Using Time-Dependent Dalitz Analysis of $\bar{B}^0 \to D[K^0_S\pi^+\pi^-]h^0$, Phys. Rev. Lett. **97**, 081801 (2006).

[11] Y. Grossman and M. P. Worah, *CP* asymmetries in B decays with new physics in decay amplitudes, Phys. Lett. B **395**, 241 (1997).

[12] R. Fleischer, *CP* violation and the role of electroweak penguins in nonleptonic *B* decays, Int. J. Mod. Phys. A **12**, 2459 (1997).

[13] D. London and A. Soni, Measuring the *CP* angle β in hadronic $b \to s$ penguin decays, Phys. Lett. B **407**, 61 (1997).

[14] M. Ciuchini, E. Franco, G. Martinelli, A. Masiero, and L. Silvestrini, *CP* Violating B Decays in the Standard Model and Supersymmetry, Phys. Rev. Lett. **79**, 978 (1997).

[15] R. H. Dalitz, On the analysis of τ-meson data and the nature of the τ-meson, Philos. Mag. **44**, 1068 (1953).

[16] G. N. Fleming, Recoupling effects in the isobar model. 1. General formalism for three-pion scattering, Phys. Rev. **135**, B551 (1964).

[17] D. Morgan, Phenomenological analysis of $I = \frac{1}{2}$ single-pion production processes in the energy range 500 to 700 MeV, Phys. Rev. **166**, 1731 (1968).

[18] D. Herndon, P. Soding, and R. J. Cashmore, Generalized isobar model formalism, Phys. Rev. D **11**, 3165 (1975).

[19] V. V. Anisovich and A. V. Sarantsev, K-matrix analysis of the $(IJ^{PC} = 00^{++})$-wave in the mass region below 1900 MeV, Eur. Phys. J. A **16**, 229 (2003).

[20] A. Satpathy *et al.* (Belle Collaboration), Study of $\bar{B}^0 \to D^{(*)0}\pi^+\pi^-$ decays, Phys. Lett. B **553**, 159 (2003).

[21] A. Kuzmin *et al.* (Belle Collaboration), Study of $\bar{B}^0 \to D^0\pi^+\pi^-$ decays, Phys. Rev. D **76**, 012006 (2007).

[22] P. del Amo Sanchez *et al.* (*BABAR* Collaboration), Dalitz-plot analysis of $B^0 \to \bar{D}^0\pi^+\pi^-$, *Proc. Sci.*, ICHEP2010 (2010) 250 [arXiv:1007.4464].

[23] K. Abe *et al.* (Belle Collaboration), Study of $B^- \to D^{**0}\pi^-(D^{**0} \to D^{(*)+}\pi^-)$ decays, Phys. Rev. D **69**, 112002 (2004).

[24] B. Aubert *et al.* (*BABAR* Collaboration), Dalitz plot analysis of $B^- \to D^+\pi^-\pi^-$, Phys. Rev. D **79**, 112004 (2009).

[25] R. Aaij *et al.* (LHCb Collaboration), Observation of Overlapping Spin-1 and Spin-3 $\bar{D}^0 K^-$ Resonances at Mass 2.86 GeV/c^2, Phys. Rev. Lett. **113**, 162001 (2014).

[26] R. Aaij *et al.* (LHCb Collaboration), Dalitz plot analysis of $B_s^0 \to \bar{D}^0 K^- \pi^+$ decays, Phys. Rev. D **90**, 072003 (2014).

[27] S. Godfrey and N. Isgur, Mesons in a relativized quark model with chromodynamics, Phys. Rev. D **32**, 189 (1985).

[28] P. Colangelo, F. De Fazio, F. Giannuzzi, and S. Nicotri, New meson spectroscopy with open charm and beauty, Phys. Rev. D **86**, 054024 (2012).

[29] R. Aaij *et al.* (LHCb Collaboration), Study of D_J meson decays to $D^+\pi^-$, $D^0\pi^+$ and $D^{*+}\pi^-$ final states in pp collisions, J. High Energy Phys. 09 (2013) 145.

[30] P. del Amo Sanchez *et al.* (*BABAR* Collaboration), Observation of new resonances decaying to $D\pi$ and $D^*\pi$ in inclusive e^+e^- collisions near $\sqrt{s} = 10.58$ GeV, Phys. Rev. D **82**, 111101 (2010).

[31] Y. Amhis *et al.* (Heavy Flavor Averaging Group), Averages of b-hadron, c-hadron, and τ-lepton properties as of summer 2014, arXiv:1412.7515.

[32] K. A. Olive *et al.* (Particle Data Group), Review of particle physics, Chin. Phys. C **38**, 090001 (2014).

[33] J.-P. Lees *et al.* (*BABAR* Collaboration), Measurement of an excess of $\bar{B} \to D^{(*)}\tau^-\bar{\nu}_\tau$ decays and implications for charged Higgs bosons, Phys. Rev. D **88**, 072012 (2013).

[34] A. Celis, Effects of a charged Higgs boson in $B \to D^{(*)}\tau\nu$ decays, *Proc. Sci.*, EPS-HEP2013 (2013) 334 [arXiv:1308.6779].

[35] Y. Sakaki, M. Tanaka, A. Tayduganov, and R. Watanabe, Testing leptoquark models in $\bar{B} \to D^{(*)}\tau\bar{\nu}$, Phys. Rev. D **88**, 094012 (2013).

[36] M. Bauer, B. Stech, and M. Wirbel, Exclusive non-leptonic decays of D, $D(s)$, and B mesons, Z. Phys. C **34**, 103 (1987).

[37] M. Neubert and A. A. Petrov, Comments on color-suppressed hadronic B decays, Phys. Lett. B **519**, 50 (2001).

[38] C.-K. Chua, W.-S. Hou, and K.-C. Yang, Final state rescattering and color-suppressed $\bar{B}^0 \to D^{(*)0}h^0$ decays, Phys. Rev. D **65**, 096007 (2002).

[39] S. Mantry, D. Pirjol, and I. W. Stewart, Strong phases and factorization for color-suppressed decays, Phys. Rev. D **68**, 114009 (2003).

[40] J. P. Lees *et al.* (*BABAR* Collaboration), Branching fraction measurements of the color-suppressed decays $\bar{B}^0 \to D^{(*)0}\pi^0$, $D^{(*)0}\eta$, $D^{(*)0}\omega$, and $D^{(*)0}\eta'$ and measurement of the polarization in the decay $\bar{B}^0 \to D^{*0}\omega$, Phys. Rev. D **84**, 112007 (2011).

[41] J. L. Rosner, Large final state phases in heavy meson decays, Phys. Rev. D **60**, 074029 (1999).

[42] Y.-Y. Keum, T. Kurimoto, H.-n. Li, C.-D. Lü, and A. I. Sanda, Nonfactorizable contributions to $B \to D^{(*)}M$ decays, Phys. Rev. D **69**, 094018 (2004).

[43] B. Aubert *et al.* (*BABAR* Collaboration), Improved measurement of the CKM angle γ in $B^\mp \to D^{(*)}K^{(*\mp)}$ decays with a Dalitz plot analysis of D decays to $K_S^0\pi^+\pi^-$ and $K_S^0K^+K^-$, Phys. Rev. D **78**, 034023 (2008).

[44] P. del Amo Sanchez *et al.* (*BABAR* Collaboration), Measurement of $D^0 - \bar{D}^0$ Mixing Parameters Using $D^0 \to K_S^0\pi^+\pi^-$ and $D^0 \to K_S^0K^+K^-$ Decays, Phys. Rev. Lett. **105**, 081803 (2010).

[45] T. Peng *et al.* (Belle Collaboration), Measurement of $D^0 - \bar{D}^0$ mixing and search for indirect CP violation using $D^0 \to K_S^0\pi^+\pi^-$ decays, Phys. Rev. D **89**, 091103 (2014).

[46] R. Aaij *et al.* (LHCb Collaboration), Analysis of the resonant components in $\bar{B}_s^0 \to J/\psi\pi^+\pi^-$, Phys. Rev. D **86**, 052006 (2012).

[47] R. Aaij *et al.* (LHCb Collaboration), Analysis of the resonant components in $\bar{B}^0 \to J/\psi\pi^+\pi^-$, Phys. Rev. D **87**, 052001 (2013).

[48] R. Aaij *et al.* (LHCb Collaboration), Measurement of resonant and CP components in $\bar{B}_s^0 \to J/\psi\pi^+\pi^-$ decays, Phys. Rev. D **89**, 092006 (2014).

[49] R. Aaij *et al.* (LHCb Collaboration), Measurement of the resonant and CP components in $\bar{B}^0 \to J/\psi\pi^+\pi^-$ decays, Phys. Rev. D **90**, 012003 (2014).

[50] C. Amsler *et al.*, Note on scalar mesons below 2 GeV in review of particle physics, Chin. Phys. C **38**, 090001 (2014).

[51] R. L. Jaffe, Exotica, Phys. Rep. **409**, 1 (2005).

[52] E. Klempt and A. Zaitsev, Glueballs, hybrids, multiquarks: Experimental facts versus QCD inspired concepts, Phys. Rep. **454**, 1 (2007).

[53] L. Zhang and S. Stone, Time-dependent Dalitz-plot formalism for $B_q \to J/\psi h^+h^-$, Phys. Lett. B **719**, 383 (2013).

[54] R. Aaij *et al.* (LHCb Collaboration), Measurement of the CP-violating phase ϕ_s in $\bar{B}_s^0 \to J/\psi\pi^+\pi^-$ decays, Phys. Lett. B **736**, 186 (2014).

[55] L. Maiani, F. Piccinini, A. D. Polosa, and V. Riquer, New Look at Scalar Mesons, Phys. Rev. Lett. **93**, 212002 (2004).

[56] G. 't Hooft, G. Isidori, L. Maiani, A. D. Polosa, and V. Riquer, A theory of scalar mesons, Phys. Lett. B **662**, 424 (2008).

[57] W. Wang and C.-D. Lu, Distinguishing two kinds of scalar mesons from heavy meson decays, Phys. Rev. D **82**, 034016 (2010).

[58] J.-W. Li, D.-S. Du, and C.-D. Lu, Determination of $f_0 - \sigma$ mixing angle through $B_s^0 \to J/\psi f_0(980)(\sigma)$ decays, Eur. Phys. J. C **72**, 2229 (2012).

[59] A. A. Alves Jr. *et al.* (LHCb Collaboration), The LHCb detector at the LHC, JINST **3**, S08005 (2008).

[60] R. Aaij *et al.*, Performance of the LHCb vertex locator, JINST **9**, P09007 (2014).

[61] R. Arink *et al.*, Performance of the LHCb outer tracker, JINST **9**, P01002 (2014).

[62] M. Adinolfi *et al.*, Performance of the LHCb RICH detector at the LHC, Eur. Phys. J. C **73**, 2431 (2013).

[63] A. A. Alves Jr. *et al.*, Performance of the LHCb muon system, JINST **8**, P02022 (2013).

[64] V. V. Gligorov and M. Williams, Efficient, reliable and fast high-level triggering using a bonsai boosted decision tree, JINST **8**, P02013 (2013).

[65] T. Sjöstrand, S. Mrenna, and P. Skands, PYTHIA 6.4 physics and manual, J. High Energy Phys. 05 (2006) 026; , A brief introduction to PYTHIA 8.1, Comput. Phys. Commun. **178**, 852 (2008).

[66] I. Belyaev *et al.*, Handling of the generation of primary events in Gauss, the LHCb simulation framework, Nuclear Science Symposium Conference Record (NSS/MIC) IEEE (2010) 1155.

[67] D. J. Lange, The EvtGen particle decay simulation package, Nucl. Instrum. Methods Phys. Res., Sect. A **462**, 152 (2001).

[68] P. Golonka and Z. Was, PHOTOS Monte Carlo: A precision tool for QED corrections in Z and W decays, Eur. Phys. J. C **45**, 97 (2006).

[69] J. Allison *et al.* (Geant4 Collaboration), Geant4 developments and applications, IEEE Trans. Nucl. Sci. **53**, 270 (2006); S. Agostinelli *et al.* (Geant4 Collaboration), Geant4: A simulation toolkit, Nucl. Instrum. Methods Phys. Res., Sect. A **506**, 250 (2003).

[70] M. Clemencic, G. Corti, S. Easo, C. R. Jones, S. Miglioranzi, M. Pappagallo, and P. Robbe, The LHCb simulation application, Gauss: Design, evolution and experience, J. Phys. Conf. Ser. **331**, 032023 (2011).

[71] W. D. Hulsbergen, Decay chain fitting with a Kalman filter, Nucl. Instrum. Methods Phys. Res., Sect. A **552**, 566 (2005).

[72] R. A. Fisher, The use of multiple measurements in taxonomic problems, Annals Eugen. **7**, 179 (1936).

[73] M. Pivk and F. R. Le Diberder, $_s$Plot: A statistical tool to unfold data distributions, Nucl. Instrum. Methods Phys. Res., Sect. A **555**, 356 (2005).

[74] R. Aaij *et al.* (LHCb Collaboration), Measurements of the branching fractions of the decays $B_s^0 \to \bar{D}^0 K^- \pi^+$ and $B^0 \to \bar{D}^0 K^+ \pi^-$, Phys. Rev. D **87**, 112009 (2013).

[75] R. Aaij *et al.* (LHCb Collaboration), Study of beauty baryon decays to $D^0 p h^-$ and $\Lambda_c^+ h^-$ final states, Phys. Rev. D **89**, 032001 (2014).

[76] T. Skwarnicki, A study of the radiative CASCADE transitions between the Υ' and Υ resonances, Ph.D. thesis, Institute for Nuclear Physics, Krakow, 1986; DESY Internal Report, Report No. DESY-F31-86-02, 1986.

[77] J. Blatt and V. E. Weisskopf, *Theoretical Nuclear Physics* (J. Wiley, New York, 1952).

[78] R. Aaij *et al.* (LHCb Collaboration), Observation of the Resonant Character of the $Z(4430)^-$ State, Phys. Rev. Lett. **112**, 222002 (2014).

[79] S. U. Chung, A general formulation of covariant helicity-coupling amplitudes, Phys. Rev. D **57**, 431 (1998).

[80] V. Filippini, A. Fontana, and A. Rotondi, Covariant spin tensors in meson spectroscopy, Phys. Rev. D **51**, 2247 (1995).

[81] G. J. Gounaris and J. J. Sakurai, Finite Width Corrections to the Vector-Meson-Dominance Prediction for $\rho \to e^+ e^-$, Phys. Rev. Lett. **21**, 244 (1968).

[82] R. R. Akhmetshin *et al.* (CMD-2 Collaboration), Measurement of $e^+ e^- \to \pi^+ \pi^-$ cross section with CMD-2 around ρ-meson, Phys. Lett. B **527**, 161 (2002).

[83] D. V. Bugg, The mass of the σ pole, J. Phys. G **34**, 151 (2007).

[84] S. M. Flatté, Coupled-channel analysis of the $\pi\eta$ and $K\bar{K}$ systems near $K\bar{K}$ threshold, Phys. Lett. **63B**, 224 (1976).

[85] S. L. Adler, Consistency conditions on the strong interactions implied by a partially conserved axial-vector current I, Phys. Rev. B **137**, B1022 (1965).

[86] S. L. Adler, Consistency conditions on the strong interactions implied by a partially conserved axial-vector current II, Phys. Rev. B **139**, B1638 (1965).

[87] K. Cranmer *et al.*, HistFactory: A tool for creating statistical models for use with RooFit and RooStats, Tech. Rep. No. CERN-OPEN-2012-016, CERN, 2012.

[88] W. Verkerke and D. P. Kirkby, *The RooFit toolkit for data modeling*, eConf. C0303241, MOLT007 (2003).

[89] K. Cranmer, Kernel estimation in high-energy physics, Comput. Phys. Commun. **136**, 198 (2001).

[90] J. P. Lees *et al.* (*BABAR* Collaboration), Precise measurement of the $e^+ e^- \to \pi^+ \pi^- (\gamma)$ cross section with the initial-state radiation method at *BABAR*, Phys. Rev. D **86**, 032013 (2012).

[91] W. H. Liang, J.-J. Xie, and E. Oset, $\bar{B}^0$ decay into D^0 and ρ or $f_0(500)$, $f_0(980)$, $a_0(980)$ and $\bar{B}_s^0$ decay into D^0 and K^{*0} or $\kappa(800)$, arXiv:1501.00088.

[92] R. Aaij *et al.* (LHCb Collaboration), First observation and amplitude analysis of the $B^- \to D^+ K^- \pi^-$ decay, Phys. Rev. D **91**, 092002 (2015).

[93] B. Aubert *et al.* (*BABAR* Collaboration), Dalitz plot analysis of the decay $B^\pm \to K^\pm K^\pm K^\mp$, Phys. Rev. D **74**, 032003 (2006).

[94] M. Ablikim *et al.* (BES Collaboration), Evidence for $f_0(980) f_0(980)$ production in χ_{c0} decays, Phys. Rev. D **70**, 092002 (2004).

[95] R. Aaij *et al.* (LHCb Collaboration), Search for the decay $B_s^0 \to \bar{D}^0 f_0(980)$, arXiv:1505.01654 (to be published).

[96] W. H. Liang and E. Oset, B^0 and B_s^0 decays into J/ψ $f_0(980)$ and J/ψ $f_0(500)$ and the nature of the scalar resonances, Phys. Lett. B **737**, 70 (2014).

[97] M. Beneke, G. Buchalla, M. Neubert, and C. T. Sachrajda, QCD factorization for exclusive, nonleptonic B meson decays: General arguments and the case of heavy-light final states, Nucl. Phys. **B591**, 313 (2000).

[98] H.-Y. Cheng and K.-C. Yang, Updated analysis of a_1 and a_2 in hadronic two-body decays of B mesons, Phys. Rev. D **59**, 092004 (1999).

[99] J. Charles, A. Höcker, H. Lacker, S. Laplace, F. R. Diberder, J. Malclés, J. Ocariz, M. Pivk, and L. Roos, CP violation and the CKM matrix: Assessing the impact of the asymmetric B factories, Eur. Phys. J. C **41**, 1 (2005).

R. Aaij,[41] B. Adeva,[37] M. Adinolfi,[46] A. Affolder,[52] Z. Ajaltouni,[5] S. Akar,[6] J. Albrecht,[9] F. Alessio,[38] M. Alexander,[51] S. Ali,[41] G. Alkhazov,[30] P. Alvarez Cartelle,[53] A. A. Alves Jr.,[25,38] S. Amato,[2] S. Amerio,[22] Y. Amhis,[7] L. An,[3] L. Anderlini,[17,a] J. Anderson,[40] R. Andreassen,[57] M. Andreotti,[16,b] J. E. Andrews,[58] R. B. Appleby,[54] O. Aquines Gutierrez,[10] F. Archilli,[38] P. d'Argent,[11] A. Artamonov,[35] M. Artuso,[59] E. Aslanides,[6] G. Auriemma,[25,c] M. Baalouch,[5] S. Bachmann,[11] J. J. Back,[48] A. Badalov,[36] C. Baesso,[60] W. Baldini,[16] R. J. Barlow,[54] C. Barschel,[38] S. Barsuk,[7] W. Barter,[38] V. Batozskaya,[28] V. Battista,[39] A. Bay,[39] L. Beaucourt,[4] J. Beddow,[51] F. Bedeschi,[23] I. Bediaga,[1]

L. J. Bel,[41] S. Belogurov,[31] I. Belyaev,[31] E. Ben-Haim,[8] G. Bencivenni,[18] S. Benson,[38] J. Benton,[46] A. Berezhnoy,[32] R. Bernet,[40] A. Bertolin,[22] M.-O. Bettler,[47] M. van Beuzekom,[41] A. Bien,[11] S. Bifani,[45] T. Bird,[54] A. Birnkraut,[9] A. Bizzeti,[17,d] T. Blake,[48] F. Blanc,[39] J. Blouw,[10] S. Blusk,[59] V. Bocci,[25] A. Bondar,[34] N. Bondar,[30,38] W. Bonivento,[15] S. Borghi,[54] A. Borgia,[59] M. Borsato,[7] T. J. V. Bowcock,[52] E. Bowen,[40] C. Bozzi,[16] D. Brett,[54] M. Britsch,[10] T. Britton,[59] J. Brodzicka,[54] N. H. Brook,[46] A. Bursche,[40] J. Buytaert,[38] S. Cadeddu,[15] R. Calabrese,[16,b] M. Calvi,[20,e] M. Calvo Gomez,[36,f] P. Campana,[18] D. Campora Perez,[38] L. Capriotti,[54] A. Carbone,[14,g] G. Carboni,[24,h] R. Cardinale,[19,38,i] A. Cardini,[15] P. Carniti,[20] L. Carson,[50] K. Carvalho Akiba,[2,38] R. Casanova Mohr,[36] G. Casse,[52] L. Cassina,[20,e] L. Castillo Garcia,[38] M. Cattaneo,[38] Ch. Cauet,[9] G. Cavallero,[19] R. Cenci,[23,j] M. Charles,[8] Ph. Charpentier,[38] M. Chefdeville,[4] S. Chen,[54] S.-F. Cheung,[55] N. Chiapolini,[40] M. Chrzaszcz,[40,26] X. Cid Vidal,[38] G. Ciezarek,[41] P. E. L. Clarke,[50] M. Clemencic,[38] H. V. Cliff,[47] J. Closier,[38] V. Coco,[38] J. Cogan,[6] E. Cogneras,[5] V. Cogoni,[15,k] L. Cojocariu,[29] G. Collazuol,[22] P. Collins,[38] A. Comerma-Montells,[11] A. Contu,[15,38] A. Cook,[46] M. Coombes,[46] S. Coquereau,[8] G. Corti,[38] M. Corvo,[16,b] I. Counts,[56] B. Couturier,[38] G. A. Cowan,[50] D. C. Craik,[48] A. Crocombe,[48] M. Cruz Torres,[60] S. Cunliffe,[53] R. Currie,[53] C. D'Ambrosio,[38] J. Dalseno,[46] P. David,[8] P. N. Y. David,[41] A. Davis,[57] K. De Bruyn,[41] S. De Capua,[54] M. De Cian,[11] J. M. De Miranda,[1] L. De Paula,[2] W. De Silva,[57] P. De Simone,[18] C.-T. Dean,[51] D. Decamp,[4] M. Deckenhoff,[9] L. Del Buono,[8] N. Déléage,[4] D. Derkach,[55] O. Deschamps,[5] F. Dettori,[38] B. Dey,[40] A. Di Canto,[38] F. Di Ruscio,[24] H. Dijkstra,[38] S. Donleavy,[52] F. Dordei,[11] M. Dorigo,[39] A. Dosil Suárez,[37] D. Dossett,[48] A. Dovbnya,[43] K. Dreimanis,[52] G. Dujany,[54] F. Dupertuis,[39] P. Durante,[6] R. Dzhelyadin,[35] A. Dziurda,[26] A. Dzyuba,[30] S. Easo,[49,38] U. Egede,[53] V. Egorychev,[31] S. Eidelman,[34] S. Eisenhardt,[50] U. Eitschberger,[9] R. Ekelhof,[9] L. Eklund,[51] I. El Rifai,[5] Ch. Elsasser,[40] S. Ely,[59] S. Esen,[11] H. M. Evans,[47] T. Evans,[55] A. Falabella,[14] C. Färber,[11] C. Farinelli,[41] N. Farley,[45] S. Farry,[52] R. Fay,[52] D. Ferguson,[50] V. Fernandez Albor,[37] F. Ferrari,[14] F. Ferreira Rodrigues,[1] M. Ferro-Luzzi,[38] S. Filippov,[33] M. Fiore,[16,b] M. Fiorini,[16,b] M. Firlej,[27] C. Fitzpatrick,[39] T. Fiutowski,[27] P. Fol,[53] M. Fontana,[10] F. Fontanelli,[19,i] R. Forty,[38] O. Francisco,[2] M. Frank,[38] C. Frei,[38] M. Frosini,[17] J. Fu,[21,38] E. Furfaro,[24,h] A. Gallas Torreira,[37] D. Galli,[14,g] S. Gallorini,[22,38] S. Gambetta,[19,i] M. Gandelman,[2] P. Gandini,[59] Y. Gao,[3] J. García Pardiñas,[37] J. Garofoli,[59] J. Garra Tico,[47] L. Garrido,[36] D. Gascon,[36] C. Gaspar,[38] U. Gastaldi,[16] R. Gauld,[55] L. Gavardi,[9] G. Gazzoni,[5] A. Geraci,[21,l] D. Gerick,[11] E. Gersabeck,[11] M. Gersabeck,[54] T. Gershon,[48] Ph. Ghez,[4] A. Gianelle,[22] S. Gianì,[39] V. Gibson,[47] L. Giubega,[29] V. V. Gligorov,[38] C. Göbel,[60] D. Golubkov,[31] A. Golutvin,[53,31,38] A. Gomes,[1,m] C. Gotti,[20,e] M. Grabalosa Gándara,[5] R. Graciani Diaz,[36] L. A. Granado Cardoso,[38] E. Graugés,[36] E. Graverini,[40] G. Graziani,[17] A. Grecu,[29] E. Greening,[55] S. Gregson,[47] P. Griffith,[45] L. Grillo,[11] O. Grünberg,[63] B. Gui,[59] E. Gushchin,[33] Yu. Guz,[35,38] T. Gys,[38] C. Hadjivasiliou,[59] G. Haefeli,[39] C. Haen,[38] S. C. Haines,[47] S. Hall,[53] B. Hamilton,[58] T. Hampson,[46] X. Han,[11] S. Hansmann-Menzemer,[11] N. Harnew,[55] S. T. Harnew,[46] J. Harrison,[54] J. He,[38] T. Head,[39] V. Heijne,[41] K. Hennessy,[52] P. Henrard,[5] L. Henry,[8] J. A. Hernando Morata,[37] E. van Herwijnen,[38] M. Heß,[63] A. Hicheur,[2] D. Hill,[55] M. Hoballah,[5] C. Hombach,[54] W. Hulsbergen,[41] T. Humair,[53] N. Hussain,[55] D. Hutchcroft,[52] D. Hynds,[51] M. Idzik,[27] P. Ilten,[56] R. Jacobsson,[38] A. Jaeger,[11] J. Jalocha,[55] E. Jans,[41] A. Jawahery,[58] F. Jing,[3] M. John,[55] D. Johnson,[38] C. R. Jones,[47] C. Joram,[38] B. Jost,[38] N. Jurik,[59] S. Kandybei,[43] W. Kanso,[6] M. Karacson,[38] T. M. Karbach,[38,†] S. Karodia,[51] M. Kelsey,[59] I. R. Kenyon,[45] M. Kenzie,[38] T. Ketel,[42] B. Khanji,[20,38,e] C. Khurewathanakul,[39] S. Klaver,[54] K. Klimaszewski,[28] O. Kochebina,[7] M. Kolpin,[11] I. Komarov,[39] R. F. Koopman,[42] P. Koppenburg,[41,38] M. Korolev,[32] L. Kravchuk,[33] K. Kreplin,[11] M. Kreps,[48] G. Krocker,[11] P. Krokovny,[34] F. Kruse,[9] W. Kucewicz,[26,n] M. Kucharczyk,[20,e] V. Kudryavtsev,[34] K. Kurek,[28] T. Kvaratskheliya,[31] V. N. La Thi,[39] D. Lacarrere,[38] G. Lafferty,[54] A. Lai,[15] D. Lambert,[50] R. W. Lambert,[42] G. Lanfranchi,[18] C. Langenbruch,[48] B. Langhans,[38] T. Latham,[48] C. Lazzeroni,[45] R. Le Gac,[6] J. van Leerdam,[41] J.-P. Lees,[4] R. Lefèvre,[5] A. Leflat,[32] J. Lefrançois,[7] O. Leroy,[6] T. Lesiak,[26] B. Leverington,[11] Y. Li,[7] T. Likhomanenko,[64] M. Liles,[52] R. Lindner,[38] C. Linn,[38] F. Lionetto,[40] B. Liu,[15] S. Lohn,[38] I. Longstaff,[51] J. H. Lopes,[2] D. Lucchesi,[22,o] H. Luo,[50] A. Lupato,[22] E. Luppi,[16,b] O. Lupton,[55] F. Machefert,[7] I. V. Machikhiliyan,[31] F. Maciuc,[29] O. Maev,[30] S. Malde,[55] A. Malinin,[64] G. Manca,[15,k] G. Mancinelli,[6] P. Manning,[59] A. Mapelli,[38] J. Maratas,[5] J. F. Marchand,[4] U. Marconi,[14] C. Marin Benito,[36] P. Marino,[23,j] R. Märki,[39] J. Marks,[11] G. Martellotti,[25] M. Martinelli,[39] D. Martinez Santos,[42] F. Martinez Vidal,[66] D. Martins Tostes,[2] A. Massafferri,[1] R. Matev,[38] Z. Mathe,[38] C. Matteuzzi,[20] A. Mauri,[40] B. Maurin,[39] A. Mazurov,[45] M. McCann,[53] J. McCarthy,[45] A. McNab,[54] R. McNulty,[12] B. McSkelly,[52] B. Meadows,[57] F. Meier,[9] M. Meissner,[11] M. Merk,[41] D. A. Milanes,[62] M.-N. Minard,[4] D. S. Mitzel,[11] J. Molina Rodriguez,[60] S. Monteil,[5] M. Morandin,[22] P. Morawski,[27] A. Mordà,[6] M. J. Morello,[23,j] J. Moron,[27] A. B. Morris,[50] R. Mountain,[59] F. Muheim,[50] J. Müller,[9] K. Müller,[40] V. Müller,[9] M. Mussini,[14] B. Muster,[39] P. Naik,[46] T. Nakada,[39] R. Nandakumar,[49] I. Nasteva,[2] M. Needham,[50] N. Neri,[21] S. Neubert,[11] N. Neufeld,[38] M. Neuner,[11]

A. D. Nguyen,[39] T. D. Nguyen,[39] C. Nguyen-Mau,[39,p] M. Nicol,[7] V. Niess,[5] R. Niet,[9] N. Nikitin,[32] T. Nikodem,[11] A. Novoselov,[35] D. P. O'Hanlon,[48] A. Oblakowska-Mucha,[27] V. Obraztsov,[35] S. Ogilvy,[51] O. Okhrimenko,[44] R. Oldeman,[15,k] C. J. G. Onderwater,[67] B. Osorio Rodrigues,[1] J. M. Otalora Goicochea,[2] A. Otto,[38] P. Owen,[53] A. Oyanguren,[66] B. K. Pal,[59] A. Palano,[13,q] F. Palombo,[21,r] M. Palutan,[18] J. Panman,[38] A. Papanestis,[49] M. Pappagallo,[51] L. L. Pappalardo,[16,b] C. Parkes,[54] C. J. Parkinson,[9,45] G. Passaleva,[17] G. D. Patel,[52] M. Patel,[53] C. Patrignani,[19,i] A. Pearce,[54,49] A. Pellegrino,[41] G. Penso,[25,s] M. Pepe Altarelli,[38] S. Perazzini,[14,g] P. Perret,[5] L. Pescatore,[45] K. Petridis,[46] A. Petrolini,[19,i] M. Petruzzo,[21] E. Picatoste Olloqui,[36] B. Pietrzyk,[4] T. Pilař,[48] D. Pinci,[25] A. Pistone,[19] S. Playfer,[50] M. Plo Casasus,[37] F. Polci,[8] A. Poluektov,[48,34] I. Polyakov,[31] E. Polycarpo,[2] A. Popov,[35] D. Popov,[10] B. Popovici,[29] C. Potterat,[2] E. Price,[46] J. D. Price,[52] J. Prisciandaro,[39] A. Pritchard,[52] C. Prouve,[46] V. Pugatch,[44] A. Puig Navarro,[39] G. Punzi,[23,t] W. Qian,[4] R. Quagliani,[7,46] B. Rachwal,[26] J. H. Rademacker,[46] B. Rakotomiaramanana,[39] M. Rama,[23] M. S. Rangel,[2] I. Raniuk,[43] N. Rauschmayr,[38] G. Raven,[42] F. Redi,[53] S. Reichert,[54] M. M. Reid,[48] A. C. dos Reis,[1] S. Ricciardi,[49] S. Richards,[46] M. Rihl,[38] K. Rinnert,[52] V. Rives Molina,[36] P. Robbe,[7] A. B. Rodrigues,[1] E. Rodrigues,[54] P. Rodriguez Perez,[54] S. Roiser,[38] V. Romanovsky,[35] A. Romero Vidal,[37] M. Rotondo,[22] J. Rouvinet,[39] T. Ruf,[38] H. Ruiz,[36] P. Ruiz Valls,[66] J. J. Saborido Silva,[37] N. Sagidova,[30] P. Sail,[51] B. Saitta,[15,k] V. Salustino Guimaraes,[2] C. Sanchez Mayordomo,[66] B. Sanmartin Sedes,[37] R. Santacesaria,[25] C. Santamarina Rios,[37] E. Santovetti,[24,h] A. Sarti,[18,s] C. Satriano,[25,c] A. Satta,[24] D. M. Saunders,[46] D. Savrina,[31,32] M. Schiller,[38] H. Schindler,[38] M. Schlupp,[9] M. Schmelling,[10] T. Schmelzer,[9] B. Schmidt,[38] O. Schneider,[39] A. Schopper,[38] M.-H. Schune,[7] R. Schwemmer,[38] B. Sciascia,[18] A. Sciubba,[25,s] A. Semennikov,[31] I. Sepp,[53] N. Serra,[40] J. Serrano,[6] L. Sestini,[22] P. Seyfert,[11] M. Shapkin,[35] I. Shapoval,[16,43,b] Y. Shcheglov,[30] T. Shears,[52] L. Shekhtman,[34] V. Shevchenko,[64] A. Shires,[9] R. Silva Coutinho,[48] G. Simi,[22] M. Sirendi,[47] N. Skidmore,[46] I. Skillicorn,[51] T. Skwarnicki,[59] E. Smith,[55,49] E. Smith,[53] J. Smith,[47] M. Smith,[54] H. Snoek,[41] M. D. Sokoloff,[57] F. J. P. Soler,[51] F. Soomro,[39] D. Souza,[46] B. Souza De Paula,[2] B. Spaan,[9] P. Spradlin,[51] S. Sridharan,[38] F. Stagni,[38] M. Stahl,[11] S. Stahl,[38] O. Steinkamp,[40] O. Stenyakin,[35] F. Sterpka,[59] S. Stevenson,[55] S. Stoica,[29] S. Stone,[59] B. Storaci,[40] S. Stracka,[23,j] M. Straticiuc,[29] U. Straumann,[40] R. Stroili,[22] L. Sun,[57] W. Sutcliffe,[53] K. Swientek,[27] S. Swientek,[9] V. Syropoulos,[42] M. Szczekowski,[28] P. Szczypka,[39,38] T. Szumlak,[27] S. T'Jampens,[4] T. Tekampe,[9] M. Teklishyn,[7] G. Tellarini,[16,b] F. Teubert,[38] C. Thomas,[55] E. Thomas,[38] J. van Tilburg,[41] V. Tisserand,[4] M. Tobin,[39] J. Todd,[57] S. Tolk,[42] L. Tomassetti,[16,b] D. Tonelli,[38] S. Topp-Joergensen,[55] N. Torr,[55] E. Tournefier,[4] S. Tourneur,[39] K. Trabelsi,[39] M. T. Tran,[39] M. Tresch,[40] A. Trisovic,[38] A. Tsaregorodtsev,[6] P. Tsopelas,[41] N. Tuning,[41,38] M. Ubeda Garcia,[38] A. Ukleja,[28] A. Ustyuzhanin,[65,64] U. Uwer,[11] C. Vacca,[15,k] V. Vagnoni,[14] G. Valenti,[14] A. Vallier,[7] R. Vazquez Gomez,[18] P. Vazquez Regueiro,[37] C. Vázquez Sierra,[37] S. Vecchi,[16] J. J. Velthuis,[46] M. Veltri,[17,u] G. Veneziano,[39] M. Vesterinen,[11] B. Viaud,[7] D. Vieira,[2] M. Vieites Diaz,[37] X. Vilasis-Cardona,[36,f] A. Vollhardt,[40] D. Volyanskyy,[10] D. Voong,[46] A. Vorobyev,[30] V. Vorobyev,[34] C. Voß,[63] J. A. de Vries,[41] R. Waldi,[63] C. Wallace,[48] R. Wallace,[12] J. Walsh,[23] S. Wandernoth,[11] J. Wang,[59] D. R. Ward,[47] N. K. Watson,[45] D. Websdale,[53] M. Whitehead,[48] D. Wiedner,[11] G. Wilkinson,[55,38] M. Wilkinson,[59] M. P. Williams,[45] M. Williams,[56] F. F. Wilson,[49] J. Wimberley,[58] J. Wishahi,[9] W. Wislicki,[28] M. Witek,[26] G. Wormser,[7] S. A. Wotton,[47] S. Wright,[47] K. Wyllie,[38] Y. Xie,[61] Z. Xing,[59] Z. Xu,[39] Z. Yang,[3] X. Yuan,[34] O. Yushchenko,[35] M. Zangoli,[14] M. Zavertyaev,[10,v] L. Zhang,[3] W. C. Zhang,[12] Y. Zhang,[3] A. Zhelezov,[11] A. Zhokhov,[31] and L. Zhong[3]

(LHCb Collaboration)

[1]*Centro Brasileiro de Pesquisas Físicas (CBPF), Rio de Janeiro, Brazil*
[2]*Universidade Federal do Rio de Janeiro (UFRJ), Rio de Janeiro, Brazil*
[3]*Center for High Energy Physics, Tsinghua University, Beijing, China*
[4]*LAPP, Université Savoie Mont-Blanc, CNRS/IN2P3, Annecy-Le-Vieux, France*
[5]*Clermont Université, Université Blaise Pascal, CNRS/IN2P3, LPC, Clermont-Ferrand, France*
[6]*CPPM, Aix-Marseille Université, CNRS/IN2P3, Marseille, France*
[7]*LAL, Université Paris-Sud, CNRS/IN2P3, Orsay, France*
[8]*LPNHE, Université Pierre et Marie Curie, Université Paris Diderot, CNRS/IN2P3, Paris, France*
[9]*Fakultät Physik, Technische Universität Dortmund, Dortmund, Germany*
[10]*Max-Planck-Institut für Kernphysik (MPIK), Heidelberg, Germany*
[11]*Physikalisches Institut, Ruprecht-Karls-Universität Heidelberg, Heidelberg, Germany*
[12]*School of Physics, University College Dublin, Dublin, Ireland*
[13]*Sezione INFN di Bari, Bari, Italy*

[14]Sezione INFN di Bologna, Bologna, Italy
[15]Sezione INFN di Cagliari, Cagliari, Italy
[16]Sezione INFN di Ferrara, Ferrara, Italy
[17]Sezione INFN di Firenze, Firenze, Italy
[18]Laboratori Nazionali dell'INFN di Frascati, Frascati, Italy
[19]Sezione INFN di Genova, Genova, Italy
[20]Sezione INFN di Milano Bicocca, Milano, Italy
[21]Sezione INFN di Milano, Milano, Italy
[22]Sezione INFN di Padova, Padova, Italy
[23]Sezione INFN di Pisa, Pisa, Italy
[24]Sezione INFN di Roma Tor Vergata, Roma, Italy
[25]Sezione INFN di Roma La Sapienza, Roma, Italy
[26]Henryk Niewodniczanski Institute of Nuclear Physics Polish Academy of Sciences, Kraków, Poland
[27]AGH—University of Science and Technology, Faculty of Physics and Applied Computer Science, Kraków, Poland
[28]National Center for Nuclear Research (NCBJ), Warsaw, Poland
[29]Horia Hulubei National Institute of Physics and Nuclear Engineering, Bucharest-Magurele, Romania
[30]Petersburg Nuclear Physics Institute (PNPI), Gatchina, Russia
[31]Institute of Theoretical and Experimental Physics (ITEP), Moscow, Russia
[32]Institute of Nuclear Physics, Moscow State University (SINP MSU), Moscow, Russia
[33]Institute for Nuclear Research of the Russian Academy of Sciences (INR RAN), Moscow, Russia
[34]Budker Institute of Nuclear Physics (SB RAS) and Novosibirsk State University, Novosibirsk, Russia
[35]Institute for High Energy Physics (IHEP), Protvino, Russia
[36]Universitat de Barcelona, Barcelona, Spain
[37]Universidad de Santiago de Compostela, Santiago de Compostela, Spain
[38]European Organization for Nuclear Research (CERN), Geneva, Switzerland
[39]Ecole Polytechnique Fédérale de Lausanne (EPFL), Lausanne, Switzerland
[40]Physik-Institut, Universität Zürich, Zürich, Switzerland
[41]Nikhef National Institute for Subatomic Physics, Amsterdam, The Netherlands
[42]Nikhef National Institute for Subatomic Physics and VU University Amsterdam, Amsterdam, The Netherlands
[43]NSC Kharkiv Institute of Physics and Technology (NSC KIPT), Kharkiv, Ukraine
[44]Institute for Nuclear Research of the National Academy of Sciences (KINR), Kyiv, Ukraine
[45]University of Birmingham, Birmingham, United Kingdom
[46]H.H. Wills Physics Laboratory, University of Bristol, Bristol, United Kingdom
[47]Cavendish Laboratory, University of Cambridge, Cambridge, United Kingdom
[48]Department of Physics, University of Warwick, Coventry, United Kingdom
[49]STFC Rutherford Appleton Laboratory, Didcot, United Kingdom
[50]School of Physics and Astronomy, University of Edinburgh, Edinburgh, United Kingdom
[51]School of Physics and Astronomy, University of Glasgow, Glasgow, United Kingdom
[52]Oliver Lodge Laboratory, University of Liverpool, Liverpool, United Kingdom
[53]Imperial College London, London, United Kingdom
[54]School of Physics and Astronomy, University of Manchester, Manchester, United Kingdom
[55]Department of Physics, University of Oxford, Oxford, United Kingdom
[56]Massachusetts Institute of Technology, Cambridge, Massachusetts 02139, USA
[57]University of Cincinnati, Cincinnati, Ohio 45221, USA
[58]University of Maryland, College Park, Maryland 20742, USA
[59]Syracuse University, Syracuse, New York 13244, USA
[60]Pontifícia Universidade Católica do Rio de Janeiro (PUC-Rio), Rio de Janeiro, Brazil (associated with Universidade Federal do Rio de Janeiro (UFRJ), Rio de Janeiro, Brazil)
[61]Institute of Particle Physics, Central China Normal University, Wuhan, Hubei, China (associated with Center for High Energy Physics, Tsinghua University, Beijing, China)
[62]Departamento de Fisica, Universidad Nacional de Colombia, Bogota, Colombia (associated with LPNHE, Université Pierre et Marie Curie, Université Paris Diderot, CNRS/IN2P3, Paris, France)
[63]Institut für Physik, Universität Rostock, Rostock, Germany (associated with Physikalisches Institut, Ruprecht-Karls-Universität Heidelberg, Heidelberg, Germany)
[64]National Research Centre Kurchatov Institute, Moscow, Russia (associated with Institute of Theoretical and Experimental Physics (ITEP), Moscow, Russia)

[65]*Yandex School of Data Analysis, Moscow, Russia*
(associated with Institute of Theoretical and Experimental Physics (ITEP), Moscow, Russia)
[66]*Instituto de Fisica Corpuscular (IFIC), Universitat de Valencia-CSIC, Valencia, Spain*
(associated with Universitat de Barcelona, Barcelona, Spain)
[67]*Van Swinderen Institute, University of Groningen, Groningen, The Netherlands*
(associated with Nikhef National Institute for Subatomic Physics, Amsterdam, The Netherlands)

[†]Deceased.
[a]Also at Università di Firenze, Firenze, Italy.
[b]Also at Università di Ferrara, Ferrara, Italy.
[c]Also at Università della Basilicata, Potenza, Italy.
[d]Also at Università di Modena e Reggio Emilia, Modena, Italy.
[e]Also at Università di Milano Bicocca, Milano, Italy.
[f]Also at LIFAELS, La Salle, Universitat Ramon Llull, Barcelona, Spain.
[g]Also at Università di Bologna, Bologna, Italy.
[h]Also at Università di Roma Tor Vergata, Roma, Italy.
[i]Also at Università di Genova, Genova, Italy.
[j]Also at Scuola Normale Superiore, Pisa, Italy.
[k]Also at Università di Cagliari, Cagliari, Italy.
[l]Also at Politecnico di Milano, Milano, Italy.
[m]Also at Universidade Federal do Triângulo Mineiro (UFTM), Uberaba-MG, Brazil.
[n]Also at AGH—University of Science and Technology, Faculty of Computer Science, Electronics and Telecommunications, Kraków, Poland.
[o]Also at Università di Padova, Padova, Italy.
[p]Also at Hanoi University of Science, Hanoi, Viet Nam.
[q]Also at Università di Bari, Bari, Italy.
[r]Also at Università degli Studi di Milano, Milano, Italy.
[s]Also at Università di Roma La Sapienza, Roma, Italy.
[t]Also at Università di Pisa, Pisa, Italy.
[u]Also at Università di Urbino, Urbino, Italy.
[v]Also at P.N. Lebedev Physical Institute, Russian Academy of Science (LPI RAS), Moscow, Russia.